UNIVERSITY OF CALIFORNIA, SAN DIEGO

Anticyclones in the Irminger Sea

A dissertation submitted in partial satisfaction of the
requirements for the degree
Doctor of Philosophy

in

Oceanography

by

Xue Fan

Committee in charge:

Uwe Send, Chair
Teresa Chereskin
Sarah Gille
Juan Lasheras
Arthur Miller
Mark Ohman
Daniel Rudnick

2014

The dissertation of Xue Fan is approved, and it is acceptable in quality and form for publication on microfilm and electronically:

_____

_____

_____

_____

_____

_____

_____

Chair

University of California, San Diego

2014

TABLE OF CONTENTS

LIST OF FIGURES

LIST OF TABLES

ACKNOWLEDGEMENTS

First and foremost, I would like to express my sincerest gratitude to my advisor, Dr. Uwe Send. His dedication to my journey through my doctoral studies was unwavering, and his creativity was inspiring. His guidance and patience throughout my studies have allowed me to grow immensely as a scientist.

I would also like to thank my committee members, who have provided expertise and advice on many levels throughout my research. Thank you, Dr. Sarah Gille, Dr. Teresa Chereskin, Dr. Art Miller, Dr. Dan Rudnick, Dr. Mark Ohman, and Dr. Juan Lasheras. The research and experience I have gained could not have been possible without the help of our collaborators. Thank you, Dr. Pierre Testor, Dr. Johannes Karstensen, Dr. Pascale Lherminier, and Dr. Erik Behrens.

My research and ocean-going experiences could not have been accomplished without the help of the extremely talented researchers and engineers in the Send Lab. Dr. Matthias Lankhorst and Dr. Sunghyun Nam provided invaluable guidance throughout my studies. My at-sea time was crucial in aiding my understanding of Physical Oceanography, and these experiences could not have been possible without the work of Paul Chua, Gabriela Chavez, Romain Heux, and Christian Begler. I could not have asked for a more welcoming, talented, hard-working, and fun group of people as mentors and colleagues.

Chapter 2, in full, is a reprint of the material as it appears in Xue Fan, Uwe Send, Pierre Testor, Pascale Lherminier, Johannes Karstensen, 2013. "Observations of Irminger Sea Anticyclonic Eddies", *Journal of Physical Oceanography*, 43, 805 – 823. The dissertation author was the primary investigator and author of this paper. This work would have not been possible without the invaluable contributions from the co-authors, Uwe Send, Pierre Testor, Johannes Karstensen, and Pascale Lherminier. We would like to thank the teams of LPO/IFREMER, LOCEAN/CNRS, PO/IFM-GEOMAR, and PORD/SIO for performing the 2006 Spray glider mission, and specifically Thierry Terre (LPO) and Jeff Sherman (SIO) for making the mission possible. Gratitude goes to the reviewers and Sarah Gille for valuable advice on the manuscript. This work benefitted from discussions with George Carnevale and William Young. Funding for the CIS mooring was provided by the European Ocean Observatory Network (EuroSITES) and

the glider was operated with MERSEA support. Altimeter data was provided via the AVISO website (*www.aviso.oceanobs.com*). Argo data was provided by the USGADAE Project website (*www.usgodae.org*). Drifter data was provided by the NOAA AOML Global Drifter Program website (*www.aoml.noaa.gov/phod/dac/index.php*).

Chapter 3 would have not been possible without the work of the co-authors, Uwe Send and Johannes Karstensen. Funding for the CIS mooring was provided by the European Ocean Observatory Network (EuroSITES). Altimeter data was provided via the AVISO website (*www.aviso.oceanobs.com*). Argo data was provided by the USGADAE Project website ($http://www.usgodae.org$). Argo gridded fields were provided by the UCSD Argo website ($http://www.argo.ucsd.edu/Gridded_fields.html$). NCEP Reanalysis Derived data was provided by the NOAA/OAR/ESRL PSD, Boulder, Colorado, USA, from their website ($http://www.esrl.noaa.gov/psd/$). The ECMWF Reanalysis data was provided by the European Centre for Medium-Range Weather Forecasts, 2009: ERA-Interim Project, available online at $http://rda.ucar.edu/datasets/ds627.0/$. The World Ocean Atlas (WOA) climatology datasets were provided by the NOAA National Oceanographic Data Center (NODC) and are available at $http://www.nodc.noaa.gov/OC5/WOA09/pubwoa09.html$.

Chapter 4 benefited from the co-author, Uwe Send, who provided valuable guidance and insight in this work. Funding for the CIS mooring was provided by the European Ocean Observatory Network (EuroSITES). Altimeter data was provided via the AVISO website (*www.aviso.oceanobs.com*). Argo data was provided by the USGADAE Project website ($http$: *www.usgodae.org*).

Chapter 5 benefited from Uwe Send, co-author, who provided insight in this study. Thank you to Erik Behrens, co-author, who performed the VIKING20 model simulations and provided the data and support. Funding for the CIS mooring was provided by the European Ocean Observatory Network (EuroSITES). Altimeter data was provided via the AVISO website (*www.aviso.oceanobs.com*). The Chelton eddy identification dataset is provided on their website at $http://cioss.coas.oregonstate.edu/eddies/$. Argo data was provided by the USGADAE Project website (*www.usgodae.org*).

VITA

2007	B. S. in Physics, Atmospheric and Oceanic Sciences, McGill University, Montreal, QC, Canada
2008	M. S. in Oceanography, Scripps Institution of Oceanography, University of California, San Diego
2014	Ph. D. in Oceanography, Scripps Institution of Oceanography, University of California, San Diego

PUBLICATIONS

Xue Fan, Uwe Send, Pierre Testor, Pascale Lherminier, Johannes Karstensen, 2013. "Observations of Irminger Sea Anticyclonic Eddies", *Journal of Physical Oceanography*, 43.

ABSTRACT OF THE DISSERTATION

Anticyclones in the Irminger Sea

by

Xue Fan

Doctor of Philosophy in Oceanography

University of California, San Diego, 2014

Professor Uwe Send, Chair

This dissertation seeks to document observations, statistics, and physical processes relating to warm, salty mesoscale anticyclonic eddies in the Irminger Sea and their impact on the properties of the region. Anticyclones are studied with a variety of platforms including a mooring, a glider, Argo floats, satellite altimetry, and a regional model. They are found to be widespread throughout the central Irminger gyre, and are similar to anticyclones documented in the neighboring Labrador Sea and Lofoten Basin. Two anticyclone formation regions are found along the boundary current, producing two size classes of anticylones. Over the period between 2002 and 2009, anticyclone transport makes an important contribution to the heat and salt budgets of the gyre upper (< 460 m) layer. Along with surface fluxes, they dominate the heat and salt balance on

this time scale. The eddy contribution is relatively steady over the 7-year period and presumably over longer timescales as well. Changes in the temperature and salinity in the central gyre can be explained by anomalies in surface forcing. Over yearly time scales, the eddy contribution plays a minimal role in the heat and salt budgets, and the dominant terms include surface forcing and non-eddy horizontal advection. The assumption was made that anticyclones decay in the basin interior, motivated by the observed absence of eddies in the winter, and we explore the hypothesis that winter mixing can lead to eddy decay. To study this, a 1D mixing model is used to show that the barotropic component of velocity can be weakened during a period of sustained surface heat loss, with little change in the baroclinic component. This can push the eddy toward a counter-rotating state, which has been shown by theoretical studies to be unstable for similar anticyclonic vortices, and may thus be a mechanism for eddy decay. Observations of anticyclones are compared to a 1/20° resolution regional model (VIKING20). The model reproduces many features of the circulation and water masses, and similar salty anticyclones as observed. However, it cannot resolve the smallest eddies that we detected, and the long-term evolution of the eddies in the model appears to be dominated by numerical diffusivity and viscosity. Therefore, the model cannot be used for studying the processes of eddy decay.

Chapter 1

Introduction

The Central Irminger Sea has earned its reputation as a region that undergoes unique and important atmospheric and oceanic phenomena. However, its remoteness and rough conditions make it a difficult region for study. It is located between Greenland and Iceland, and represents part of the eastern half of the North Atlantic subpolar gyre. Its components are diverse oceanographically, having influences from the subtropical thermocline from the North Atlantic Current as well as dense overflow waters formed from the Arctic. Since the study by Pickart et al. (2003), the Irminger Sea has been identified as a region likely to undergo deep open ocean convection under appropriate atmospheric conditions, and Bacon et al. (2003) provide evidence that convection did indeed occur in the winter of 1996/7. After a period of no deep convection, Våge et al. (2008a) report that the Irminger Sea once again experienced deep mixing in the winter of 2007/8. This makes the Irminger Sea one of the few sites of new water formation in the world (previously thought to be limited to the Greenland, Labrador, Mediterranean, and Weddell Seas (Marshall and Schott, 1999)). In order for open-ocean deep convection to occur, *preconditioning* of the water column is required (Group, 1970; Bacon et al., 2003). This consists of an existing region of cyclonic circulation with isopycnal surfaces forming a dome with a central region of weakly stratified water brought to the surface. Then, there must be sufficiently strong surface buoyancy removal (usually by strong air-sea heat fluxes) to deplete the surface stratification and cause deep convection.

Based on the schematic by Schott et al. (2004), a diagram of the upper and deep currents within the Irminger Sea is shown in figure 2.1. Surface circulation is generally

cyclonic, dominated by the northward flowing Irminger Current on the east, and the southward flowing branches of the East Greenland Current on the west. The Irminger Current and offshore component of the East Greenland current are warm and salty, with salinities generally above 34.95 psu and temperatures exceeding 6°C. It is fed by the western branch of the North Atlantic Current as it separates in the Iceland Basin. East of the eastern limb of the Irminger current are thick layers of subpolar mode water formed over the Reykjanes Ridge and in the Iceland Basin. The inshore component of the East Greenland Current (also known as the East Greenland Coastal Current) is a very fresh and cold surface flow originating from Arctic waters, and it carries water southward along the eastern coast of Greenland. Deep water flows consist of Denmark Strait Overflow Water and Iceland Strait Overflow Water, originating from the Arctic and flowing from their respective straits. This deep water eventually evolves to become a major component of the North Atlantic Deep Water (Dickson and Brown, 1994).

Because of the Irminger Sea's rough weather and seasonal sea-ice coverage, direct observations are difficult to make, and little is known about the variability of deep mixing, water mass formation, and even the variability of the Irminger and East Greenland Currents. The Central Irminger Sea, like most other areas of the ocean, undergoes much mesoscale (eddy) activity, which constitutes a large part of its variability. Eddies have been studied and modeled in other ocean regions in order to gain insights into their structure, methods of formation, and ultimately, their impact on their environment through which they are advected. Because of their small size (compared to boundary currents and large-scale oceanic flows) and unpredictable movements, they are difficult to observe with instrumentation, and few observations have been able to characterize an eddy's properties and behavior. Due to their nature, it is useful to combine different methods of observation in order to observe an eddy. Both anticyclonic and cyclonic eddies distort the sea surface height, and with the improvement of satellite altimetry data, signatures of eddies can be seen in every ocean basin ranging in size from many hundreds of kilometers to the limit of resolution of the satellite altimetry (about 40 km at mid-latitudes) (e.g. Traganza et al., 1983; Abbott and Zion, 1985). They can appear and disappear in a matter of weeks, but a study by McWilliams (1985) suggests that some coherent submesoscale eddies can propagate for at least a year's time before losing their

coherent structure. Eddies are found in satellite altimetry to exhibit both short and long propogation paths through an ocean basin (Chelton et al., 2011).

There are a few mechanisms for eddy formation: instabilities arising from edges of currents (e.g. Gill et al., 1974; Arbic and Flierl, 2004) or Rossby waves (LaCasce and Pedlosky, 2004), topography (Huppert and Bryan, 1976b), and during the breakup of a plume during the deep convection process (Send and Marshall, 1995). McGillicuddy et al. (2007) describe three major divisions of eddies: anticyclonic, cyclonic, and mode-water eddies. Anticyclonic and cyclonic eddies are the 'classic' eddy with dipping and doming isopycnals, respectively (both seasonal and permanent). The mode-water eddy differs slightly in that an anticyclonic flow with a dipping of permanent isopycnals is found beneath a doming of seasonal isopycnals, due to a lens-like core shape. All of these eddies will exhibit strong azimuthal rotations (compared to the ambient flow) somewhere within the eddy, usually at a critical radius from the center, before and beyond which velocities decay. McWilliams (1985) propose a sub-mesoscale coherent eddy model where subsurface maxima in azimuthal velocities occur at the transition between a center area of constant potential vorticity (the 'core') and the remaining outskirts of the eddy. Within the eddy core, water from the eddy formation area may be trapped within, in a sense, 'bounded' by the fast azimuthal flow surrounding it. As an eddy propagates through different water, mixing may occur at the edges of the eddy, causing long filaments as the eddy loses its outer body to the ambient water. When an eddy decays or loses its coherence, the net effect can be a 'bolus' transport of its core water.

Because of their coherent nature and often long propagation distances, eddies will frequently carry foreign water (from where they formed) to areas of different water, possibly affecting the properties and dynamics of the new area. The potential importance of physical property transport by eddies is exemplified by Gelderloos et al. (2011); this study determines from a model of deep convection and restratification that the transport of heat by Irminger Ring Eddies (eddies formed by topography containing Irminger Current water in the Labrador Sea) replenishes 45% of the heat content deficit in a convection area within 6 months, and are thus important contributors to restratification in the Labrador Sea.

The overarching goal of this dissertation is to examine mesoscale to submesoscale eddy processes in the Irminger Sea. Because of the capacity for anticyclonic vortices to affect basin properties and budgets in neighboring North Atlantic basins, our focus is on anticyclonic eddies. Following this introduction (Chapter 1), Chapter 2 describes the observations of these anticyclones using newly-developed methods to objectively obtain eddy properties (such as size and property distributions). Using the statistics obtained from Chapter 2, Chapter 3 compares the horizontal eddy transport of heat and salt into the basin with other important terms in the budget. The dominant processes governing the balance of heat and salt are discussed in the context of different time scales. Chapter 4 examines one possible mechanism for promoting instability in the anticyclones which can explain the lack of anticyclones observed during the winter. Finally, Chapter 5 examines a high-resolution eddy-resolving regional model. Overall characterics of water properties and statistics of these model eddies are compared to the observations.

Chapter 2

Observations of Anticyclonic Eddies in the Irminger Sea

This is a reproduction of the following paper:
Xue Fan, Uwe Send, Pierre Testor, Pascale Lherminier, Johannes Karstensen, 2013. "Observations of Irminger Sea Anticyclonic Eddies", *Journal of Physical Oceanography*, 43, 805 – 823.

2.1 Abstract

Mesoscale anticyclonic eddies in the Irminger Sea are observed using a mooring and a glider. Between 2002 and 2009, the mooring observed 53 anticyclones. Using a kinematic model, objective estimates of eddy length scales and velocity structure are made for 16 eddies. Anticyclones had a mean core diameter of 12 km and their mean peak observed azimuthal speed was 0.1 m s^{-1}. They had core salinities and potential temperatures of 34.91-34.98 and 4.48-5.34 °C, respectively, making them warm and salty features. These properties represent a typical salinity anomaly of 0.03 and a temperature anomaly of 0.28 °C from non-eddy values. All eddies had small ($\ll$1) Rossby numbers. In 2006, the glider observed two anticyclones having diameters of about 20 km and peak azimuthal speeds of about 0.3 m s^{-1}. Similar salinity anomalies were detected throughout the Irminger Sea by floats profiling in anticyclones. Two formation regions for the eddies are identified: one to the west of the Reykjanes Ridge and the

other off the East Greenland Irminger Current near Cape Farewell close to the mooring. Observations indicate that eddies formed in the former region are larger than the eddies observed at the mooring. A clear increase in eddy salinity is observed between 2002 and 2009. The observed break-up of these eddies in winter implies that they are a source of salt for the central gyre. The anticyclones are similar to those found in both the Labrador Sea and Norwegian Sea, making them a ubiquitous feature of the subpolar North Atlantic basins.

2.2 Introduction

The Irminger Sea (shown in figure 2.1) forms part of the transition zone between the warmer, more saline subtropical North Atlantic and the colder, fresher Arctic waters. The Irminger Current brings warm, salty water from the south into the Irminger Sea along the west side of the Reykjanes Ridge (see Schott et al., 2004; Lherminier et al., 2010; Daniault et al., 2011). At 65 °N, the current turns and flows south along the Greenland coast, becoming the East Greenland Irminger Current (EGIC). At Cape Farewell, the EGIC wraps around Greenland. Here, part of the EGIC transport is retroflected back towards the center of the Irminger Sea (Holliday et al., 2007).

Like in other basins in the North Atlantic, eddies in the Irminger Sea are often noted for their strong signal in in-situ measurements (e.g. De Jong, 2010; Våge et al., 2011a; De Jong et al., 2012). In the neighboring Labrador Sea (see figure 2.1), it has been shown that a certain type of eddy (called 'Irminger Current Anticyclones', or ICAs) is responsible for between 25 and 100% of the heat needed to balance the surface heat loss during winter convection (Lilly et al., 2003; Katsman et al., 2004; Hátún et al., 2007; Rykova et al., 2009) and can be an important contributor to the salt (or freshwater) budget (Hátún et al., 2007; Schmidt and Send, 2007). In the Norwegian Sea, anticyclones observed in the Lofoten Basin (see figure 2.1) have been shown to be essential in maintaining the heat balance (Nilsen and Falck, 2006; Köhl, 2007; Rossby et al., 2009a). In both the Labrador Sea and Lofoten Basin, eddies have been extensively observed and documented, but an equivalent analysis of eddies in the Irminger Sea does not yet exist, and the potential for the eddies in the Irminger Sea to affect budgets has

not been explored.

Eddies in the Irminger Sea appear in many observations (e.g. Holliday et al., 2007; De Jong, 2010; Daniault et al., 2011; Våge et al., 2011a; De Jong et al., 2012), but only a few studies have quantified their size and examined their properties. One study by Krauss (1995) shows energetic eddies in the center of the Irminger Sea gyre having a mean eddy kinetic energy (EKE) four times greater than the mean Irminger Sea kinetic energy. The eddies observed from these shipboard measurements typically have a horizontal scale of 75 km, and an anticyclone is observed with anomalously high salinity and temperature compared to non-eddy water found in the Irminger basin. Another study of eddies by Bruce (1995) focused on cold-core cyclonic eddies observed by satellite and moored current meters. These cyclones, having a diameter of 20-40 km, stayed trapped within the EGIC and did not appear to enter the gyre interior.

This study seeks to add to the present knowledge of eddies in the Irminger Sea. We focus on observations of anticyclonic eddies found in the Irminger Sea for two reasons: first, because they represent a source of heat and salt to the basin and may thus modulate the water mass properties in the Irminger sea, and second, because they appear to be analogous to the anticyclones found in the Labrador and Norwegian Seas, making such eddies a wide-spread phenomenon in the high-latitude North Atlantic. We present this work in two parts. Using data from a 7-year mooring timeseries, a glider, the Argo float array, and satellite altimetry, the present study focuses on analyzing the properties of the observed anticyclones. Chapter 3 will then seek to quantify the eddy transport of heat and salt by the observed anticyclones, and to determine their importance in the heat and salt budgets of the upper waters of the Irminger Sea.

This paper is organized as follows. We describe the data used in section 2.3. Sections 2.4 and 2.5 present the data treatment and observations of properties of anticyclones obtained from the 7-year mooring timeseries and the glider, respectively. Basin-wide eddy observations are presented in section 2.6, and the origin of the eddies is examined in section 2.7. A comparison with Labrador Sea and Lofoten Basin anticyclones is made in section 2.8, and a discussion follows in section 2.9.

2.3 Data

2.3.1 Mooring

The Central Irminger Sea (CIS) mooring is located nominally at 59.7°N 39.7°W (marked by the red triangle in figure 2.1). It was placed in the region of lowest surface dynamic height corresponding to the center of the gyre by this measure. The mooring has been in operation since September 2002. Primary instruments include Sea-bird MicroCATs which record temperature, conductivity, and pressure at approximately 14 depths between the surface and 1500m with a 20 minute temporal resolution. Starting in 2003, currents in the upper 800m of the water column were measured using a combination of a 300kHz (upward) and a 150kHz (downward) Acoustic Doppler Current Profiler (ADCP). The current observations were complemented by rotary current meters at 1000m and 2400m depth. Biogeochemical sensors measured nitrate, chlorophyll-a fluorescence, and carbon dioxide at 45m. Only the physical data are used in this study. Table 2.1 shows a representative list of instrumentation used at various depths.

The physical data from the CIS mooring instrumentation were calibrated each time the mooring was serviced. The mooring data contain some gaps due to equipment failure. The data used in this study span late 2002 to mid-2009 and is quality controlled. A detailed description of the quality control procedures applied to the CIS mooring data is given in Karstensen (2005). The variables (temperature, salinity, and ADCP velocities) were linearly interpolated onto a common time axis of one-hour intervals. Using the time-varying pressure signal and mooring instrument placement, variables were linearly interpolated onto a constant 20db pressure grid. Additionally, the ADCP data were low-pass-filtered using an Equiripple filter to suppress features with frequencies larger than 1 per day (thus removing inertial waves and tides).

2.3.2 Glider

We use data from the Spray glider mission executed in 2006 under the Marine Environment and Security for the European Area (MERSEA) project. The glider path is shown in yellow in figure 2.1. The Spray glider is an autonomous underwater vehicle that uses changes in buoyancy to propel itself through the water column while

taking profiles of temperature, pressure, and salinity. While at the surface, the Spray glider transmits its GPS position fix and dive data through the Iridium satellite system. The GPS fixes are used to calculate an absolute depth-averaged velocity using dead-reckoning; from here on, when the phrase 'glider velocity' is used, a velocity averaged over the depth of the dive is implied. A detailed description of the Spray glider can be found in other publications (e.g. Sherman et al., 2001; Rudnick et al., 2004). The Spray glider used here sampled from the surface to 1000m depth, making dives between 3 km and 5 km apart horizontally, taking about 5 hours between each surfacing.

2.3.3 Satellite altimetry

For satellite altimetry data, the gridded merged AVISO product (described in Picot et al., 2003) are used in this study. The sea surface height anomaly is an objectively-mapped estimate calculated relative to a mean sea surface averaged over 1992-2005. This product has a time resolution of 7 days and comes corrected for various environmental effects (wet and dry troposphere, inverse barometer, electromagnetic bias, ocean tides. See Picot et al., 2003, for more details). The merged product is so called because it is a combination of the TOPEX/Poseidon Experiment, Jason-1, EnviSat, and Geosat satellites. Both latitude and longitude coordinates are mapped onto a $1/3^{\circ}$ Mercator projection while accounting for long-wavelength errors (Ducet et al., 2000).

A dataset derived from the satellite alimetry merged product results from the eddy tracking procedure performed by Chelton et al. (2007); this procedure identifies and tracks coherent mesoscale eddies globally from 1992 to 2008. Details of the eddy tracking algorithm can be found from Chelton et al. (2011). The method which produced the dataset in this study will be referred to as the 'Chelton' algorithm. It should be noted that the gridded satellite altimetry product dampens eddy signals smaller than 40 km in size (Chelton et al., 2011), and appears to have large uncertainties near the EGIC region (Gourcuff et al., 2011).

2.3.4 Argo

Argo floats within the Irminger Sea provide profiles of temperature and salinity from the surface to 2000m depth approximately every 10 days. These floats drift at 1000m for about 10 days, then descend to 2000m and rise to the surface over 6 hours, collecting measurements on ascent. At the surface, data are transmitted and the float's location is determined. The float then dives back to 1000m to repeat its 10-day cycle. The data from these floats are available through the International Argo Project and can be found through the GODAE project server ($http://www.usgodae.org/Argo/Argo.html$). Only delayed-time quality-controlled data were used in this study.

2.3.5 'Ovide' Ship Sections

The 'Ovide' cruises were carried out as described in detail by Lherminier et al. (2007, 2010). They were performed on the R/V Thalassa between June and July of 2002, 2004, and 2006. Part of their cruise track, shown with white circles in figure 2.1, crosses the Irminger basin from the coast of Greenland to beyond the Reykjanes Ridge. At each of the approximately 30 stations in the Irminger Sea, measurements included temperature, conductivity, and pressure via a Neil Brown Mark III CTD probe. Salinity was calibrated with seawater samples analyzed on board.

2.3.6 15m Drogued Drifters

Two drifter tracks are used to illustrate different flow situations in this study. They were obtained from the public archives of the Global Drifter Data Assembly Center at the National Oceanographic and Atmospheric Administration's Atlantic Oceanographic and Meteorological Laboratory (AOML). Drifters were drogued at 15m below the surface float and were tracked by satellite positioning. Drifter details, processing, and quality control at AOML are described in Hansen and Herman (1989) and Hansen and Poulain (1996).

2.4 Anticyclones observed at the CIS Mooring

2.4.1 Methods

Figure 2.2 shows the mooring salinity timeseries with potential density contours superimposed. Here, both salinity and density are smoothed with a 3-day running mean at each pressure level. One first notices a change in overall color from cooler to warmer tones from 2002 to 2009, representing an overall increase in salinity over the dataset. The surface to 1000 m mean salinity increases 5.7×10^{-3} per year over the timeseries. This is within the 1.15-7.3×10^{-3} per year rate of salinity increase described by others in the Irminger Sea between 2003 and 2007 (Sarafanov et al., 2007; De Jong, 2010). The trend is also the same magnitude as the general salinification observed in the Labrador Sea and Nordic Seas beginning in the 2000s (see Falina et al., 2007; Sarafanov et al., 2007; Holliday et al., 2008; Louarn et al., 2009). This interannual trend is not the focus of the present paper.

The next obvious scale of variability is the displacement of isopycnals often corresponding to marked changes in salinity, and usually lasting on the order of ten days. These features appear less frequently between January and May, a period of strong winter surface forcing. They also appear to undergo a change in properties over the timeseries: their salinity representation evolves from light red in 2002 to deep red and white in 2009. This signifies a salinifying trend of the features themselves, an aspect that will be addressed in a later section.

Four possibilities exist to explain these features: (a) internal wave motion, (b) meanders from the nearby EGIC, (c) fresh-core cyclonic eddies (doming isopycnals with lower, or more blue, salinity), or (d) salty-core anticyclonic eddies (bowl-shaped isopycnals with higher, or more red, salinity). We use hodographs produced from the mooring ADCP data to determine that these features are (d), salty-core anticyclonic eddies. Following the analyses of Lilly and Rhines (2002), the presence of an eddy event moving past a mooring produces a hodograph with D-shaped curves, closed circles, or straight lines, resulting from a *closed* vortex's turning velocities. At almost all of the high salinity anomalies corresponding to bowl-shaped isopycnals, these hodograph shapes are indeed observed. Internal wave-like motions would not create such a turning

of velocities, nor would a meander from the EGIC (explored again in a later section), ruling out (a) and (b). Also, features with doming isopycnals showed no hodograph shapes corresponding to cyclonic eddies. We are left with choice (d), that most of this variability is caused by anticyclonic eddies with a high salinity core.

Our objective is now to estimate the eddy size and create a census of observed events. We present a method to estimate the eddy radius (R_{max}) and accompanying maximum azimuthal velocity (V_{max}), employing to the model used by Hátún et al. (2007). This model assumes the eddy is a vortex in solid body rotation, an observed characteristic for anticyclonic eddies in previous in-situ studies (e.g. Newton et al., 1974; Armi et al., 1989; Pingree and Le Cann, 1992; Hátún et al., 2007). Thus, the azimuthal velocity, V, grows linearly with the radial distance, r, as

$$V(r) = \frac{V_{max}}{R_{max}} r, r < R_{max}. \tag{2.1}$$

Beyond the core radius ($r > R_{max}$), V will decay with radial distance. Because we do not use observations beyond R_{max} in our data treatment, the shape of this decay does not change our result.

We determine whether a high-salinity feature is an eddy, and then we estimate R_{max} and accompanying maximum azimuthal velocity V_{max}, using the model from (2.1). The steps to achieve this are as follows:

1. *Identify eddy occurrences*. We isolate events with high salinity anomalies coinciding with dipping isopycnals (an example of which is shown in figure 2.3a). Data encompassing 3 days before the first detection of the salinity anomaly and 3 days after its last detection are used in the next steps. An anomaly is considered significant when the salinity exceeds the mean plus one standard deviation of the average salinity in a given year between 200 and 300m depth (the layer where the highest salinities are typically found). Values for this salinity threshold ranged from 34.91 to 34.99. The presence of an eddy event is then verified from hodographs following Lilly and Rhines (2002). D-shaped hodographs indicate observations where $r < R_{max}$ (the eddy core is crossed), circles imply observations where all $r > R_{max}$, and straight lines occur only when the center of the eddy is crossed. Events with other hodograph shapes are not considered further in the eddy analysis. In the case where the eddy

core is crossed, two maxima are observed in the ADCP velocity speed, and only one maximum is observed in crossings of the eddy periphery. The eddy events (core and peripheral encounters) are shown with white circles in figure 2.2 and are all used in eddy counts and property statistics, but only the events that cross the core can be used to estimate R_{max} and V_{max} with the method developed here.

2. *Find the direction of eddy translation past the mooring*. Following Lilly et al. (2003), herein referred to as L03, the eddy translation direction can be found by identifying the two time points $T_{1,max}$ and $T_{2,max}$ when the eddy core R_{max} crosses the mooring, and extracting the observed velocities at those times ($\vec{V}_{1,maxtot}$ and $\vec{V}_{2,maxtot}$). These observed velocities are averaged from 200 to 800m depth (a layer that incorporated most of the eddy velocity signal). Here we depart from L03 by not using the velocity observations to determine $T_{1,max}$ and $T_{2,max}$ because the velocities in our dataset are asymmetric and not centered on the eddy high salinity core. This is likely due to barotropic circulations and non-eddy flows. Instead, we prefer to find the times when the maximum isopycnal slope or horizontal pressure gradient passes the mooring, using the time derivative of pressure (dp/dt) as a proxy for the horizontal pressure gradient. Here, dp/dt is derived from density data using the hydrostatic balance and averaged over 200-800m. For an anticyclone we expect the dp/dt signal to move from negative, through zero, to positive as the eddy core is crossed. From this, we determine $T_{1,max}$ (minimum dp/dt), $T_\circ$ (where the mooring comes closest to the eddy center, when dp/dt crosses zero), and $T_{2,max}$ (maximum dp/dt). These quantities are shown in an example eddy in panel b and d of figure 2.3. The velocities $\vec{V}_{1,maxtot}$ and $\vec{V}_{2,maxtot}$ are the observed ones at the times $T_{1,max}$ and $T_{2,max}$ and are used in the translation direction estimate. As explained in L03, the eddy translation direction is perpendicular to the vector difference $\vec{V}_{1,maxtot} - \vec{V}_{2,maxtot}$.

3. *Calculate the translation speed of eddy past the mooring*. We find a depth-independent translation speed such that the observed velocity shear and the observed rate of change of density will be in thermal wind balance. This method differs from that of L03, who balance the absolute velocities and the rate of change of pressure. For ease of notation we use a local rotated coordinate system where x is the direction of translation, estimated in the previous step. Thermal wind balance is then defined

by

$$f\frac{\partial v}{\partial z} = -\frac{g}{\rho_\circ}\frac{\partial \rho}{\partial x}. \tag{2.2}$$

Here, f is the Coriolis frequency ($f = 1.26\times10^{-4}s^{-1}$ at 60 °N), v is the velocity component perpendicular to the direction of x, z is the vertical direction, g is 9.8 m s^{-2}, ρ is the potential density, and $\rho_\circ$ is a reference potential density (taken as the average potential density over all depths over the timeseries). This departs from L03 also in that we neglect the cyclostrophic term, which is small for our eddies. As mentioned, L03 suggest reconstructing the pressure field by vertically integrating the density field and comparing this to observed velocity magnitudes. We opt to balance only the horizontal density gradient field with the vertical shear because the barotropic component of the eddy flow is large (visible in figure 2.3c). It would therefore be incorrect, in our case, to balance observed absolute velocities with pressure gradients referenced to some depth, as in L03. Using (2.2), we estimate ∂x as Δx, the size of the eddy core transect. We then define U as the magnitude of the translation velocity. Using $\Delta x = -U\Delta t$, where $\Delta t = |T_o - T_{1,2,max}|$, we have an estimate of U. Comparing the two estimates of U for each half of the transected eddy (at $T_{1,max}$ and $T_{2,max}$) gives an indication of the robustness of the results.

4. *Generate velocities due to eddy flow only*. Now we assume, as done in L03, that the movement of the eddy past the mooring is due to a depth-independent translation with magnitude U and direction determined by the previous steps; this translation is removed from the observed velocities to obtain a velocity signal representing eddy flow only. This yields our estimate of the true maximum eddy speed V_{max}, for which we obtain two values, $V_{1,max}$ and $V_{2,max}$, representing estimates at $T_{1,max}$ and $T_{2,max}$, respectively.

5. *Estimate R_{max} using a least-squares fit of eddy velocities to a solid body model*. We take a step further than L03 here to estimate the actual eddy radius. Recall the solid body model described by (2.1). In our rotated frame, x is in the direction of translation, and y is perpendicular to this. We obtain the following equations describing the mooring velocity components:

$$u_{fit} = \frac{V_{max}}{R_{max}}y_o + U \tag{2.3}$$

$$v_{fit} = -\frac{V_{max}}{R_{max}} X, \tag{2.4}$$

where $X = x_o - Ut$, t is the time vector, and y_o is the offset in the y-direction (constant in the rotated frame). We know U, V_{max}, and $x_o = -UT_{1,max}$. The remaining unknowns are R_{max} and y_o, and are determined using the Nelder-Mead method (see Nelder and Mead, 1965) to minimize the sum of the squared misfit between eddy model velocities (u_{fit}, v_{fit}) and the observed velocities over the period between $T_{1,max}$ and $T_{2,max}$ (where the eddy is expected to exhibit solid body rotation).

The estimates of U, V_{max}, and R_{max} come from the average of the two segments of the eddy crossings; the difference between the estimates at these two segments gives an idea of the asymmetry and the error of the estimates. The root-mean-squared deviation was $\pm$ 0.017 m s^{-1} for U and $\pm$ 0.010 m s^{-1} for V_{max}, which meant a variability of $\pm$4.5 km for the R_{max} estimate. Results were compared with the estimates performed using the cyclogeostrophic method from L03; our method results in a consistently larger estimate of U compared to their method. It would be expected that the L03 method underestimates the translation speed for our eddies, for the case of a non-negligible barotropic flow which is missing in their calculation of dp/dt. This would lead to an underestimate of the eddy sizes (R_{max}). The sensitivity to the form of (2.1) was tested by performing the previous steps using a Gaussian velocity distribution with the form $V(r) = V_{max}\exp([(r - R_{max})/(R_{max}/2)]^2)$. The fit determined R_{max} to be, on average, 15% higher than R_{max} resulting using (2.1), which is well within the range of the $\pm$ 4.5 km variability of the R_{max} estimate. This suggests that the R_{max} fit is sufficiently insensitive to the exact model used in the minimization.

2.4.2 Results

Using the above method, a total of 76 high salinity anomalies coinciding with dipping isopycnals were found between September, 2002 and June, 2009. Of these, 54 had sufficient velocity and density data to proceed further. Forty-four events were identified as anticyclones from their hodograph and the direction with which their velocities turned, and are marked by white circles in figure 2.2. To revisit an earlier discussion, these features cannot be meanders from the nearby EGIC not only because their

hodographs show the shapes produced only by anticyclones, but because of the following density gradient argument. We compare the horizontal density gradients observed in the mooring eddies and the Ovide stations which sampled in the EGIC. The repeated Ovide transects all show the EGIC having about half the density gradient of that observed in the eddies. To create the same degree of isopycnal dipping in the same time period as an eddy event, the current would need to meander almost 700 km in 10 days. This requires a velocity of 0.8 m s^{-1} persisting for 10 days. Velocities observed by the mooring and satellite altimetry peak at 0.3 m s^{-1} in the vicinity of the current, so such a high velocity is unlikely.

An additional 9 high salinity anomaly events did not show an obvious eddy hodograph signature but had turning velocity vectors associated with their salinity anomalies. This turning resembled that of the positively identified anticyclones, and are likely to be anticyclones as well, despite their more irregular hodographs. These eddies are included in eddy counts and statistics as well as in the eddy identification in figure 2.2. Twenty-seven of the identified anticyclones exhibit two velocity maxima, meaning the mooring measurements occured within R_{max}, and 16 eddies showed expected alignment among all signals and were used in the estimate of R_{max}. Anticyclones had core salinities and potential temperatures of 34.91-34.98 and 4.48-5.34°C, respectively. These values represent a typical salinity anomaly of 0.03 and temperature anomaly of 0.28°C from non-eddy values. Figure 2.4 shows the results of the eddy property estimates from the mooring data from 2002 to 2009. The mean anticyclone diameter was 12 km. The estimate of V_{max} ranges from 0.04 m s^{-1} to 0.22 m s^{-1} (figure 2.4b), and has a mean of 0.10 m s^{-1}. Panel c of figure 2.4 shows the translation vector $\vec{U}$ for each anticyclone with a core crossing. The mean translation speed is 0.026 m s^{-1}, about one order of magnitude smaller than the eddy component of the velocity signal. Eddy translation appears to be most common toward the north-east. Although the CIS mooring was placed in the center of the lowest surface dynamic topography, some mid-depth recirculation was inferred by Lavender et al. (2000) at that location. Our eddy translations are consistent with that larger-scale mid-depth gyre circulation pattern.

The Rossby number, R_o, is defined as $R_o = |V_{max}| / (R_{max} f)$ (see Hebert et al., 1990). There are a few choices for the horizontal scale and velocity maximum that can

be used in the calculation of R_o; here, the variables R_{max} at V_{max} are used because they represent the dynamic variables associated with eddy velocities. The Rossby numbers of the mooring anticyclones (not shown) ranged between 0.01-1 and had a mean value of 0.3. These Rossby numbers suggest eddies with geostrophically-dominated flow.

The total number of anticyclones observed each year is shown in figure 2.4d (including those whose core was not crossed). Counts represent eddy totals beginning each June. The counts for the period 2003-2004 are extrapolated due to sampling gaps that year; we estimate the total number of eddies which would have been observed during this period if we had a full dataset by dividing the eddy count by the time fraction during which data are available that year. The number of anticyclones observed each year is not steady, and an almost three-fold increase in eddy occurrences is observed from 2003 to 2005 followed by a period of lower counts. There is a salinifying trend of the eddy cores plotted in figure 2.4e. The observed trend in surface to 1000 m mean salinities of anticyclones is 5.7×10^{-3} per year, identical to the salinifying trend over the entire timeseries, described earlier. This suggests that the properties of eddies and non-eddy water in the Irminger basin are linked. Trends will be examined in detail in Chapter 2.

2.5 Anticyclones observed by a glider

Two eddies, marked by yellow boxes on the property profiles in figure 2.5a and b, are encountered by the glider. Each time the glider observes a feature with bowl-shaped isopycnals and anticyclonically-turning velocities. These anticyclones have a well-mixed core of salty ($>$ 34.95) and warm ($>$5.5 °C) water between 200-700m . The core layer coincided with bowl-shaped isopycnals below 400m and a doming of isopycnals above it. This type of structure resembles that of a mode-water eddy (e.g. McGillicuddy et al., 2007), and is similar to the structure of some Labrador Sea ICAs and Meddies found in the North Atlantic basin (Richardson et al., 1989). Satellite altimetry in the region (figure 2.5c and d) shows an anticyclonic structure centered at approximately 59.8°N, 36.5°W that is crossed by the glider.

2.5.1 Method

Our goal here is to sort glider profiles in terms of distance from the eddy center, allowing us to estimate the size and show the property distributions of the eddy. As the glider follows its trajectory, we assume that the eddy is also moving with a depth-independent, constant translation $\vec{U}$, as we did in the mooring method. We want to position each glider dive relative to the translating eddy center. To do this, we move each glider dive back a distance $|\vec{U}|\Delta T$ in the direction $-\vec{U}$. Here, ΔT is the time elapsed from the first dive. This places each glider dive relative to the position of the eddy center at the time of the first dive. We find the $\vec{U}$ which minimizes the variance of the radial component of velocity after subtracting $\vec{U}$ from observed velocities. This assumes that the velocity signal (other than $\vec{U}$) is dominated by the azimuthal eddy velocity, and the radial component is small (see Martin et al., 2009, for an example of this method). In this fit, the remaining unknown to be determined is the center location corresponding to the eddy at the first glider dive. After placing each dive relative to the eddy center, we can sort properties and view them with respect to distance from the center. The continuity of the data is an indication of successful sorting. This method gives information about eddy size and peak velocity, the quantities of interest analyzed also by the mooring method outlined earlier.

The treatment of the glider data presented here is significantly simpler than that for mooring data. We discuss here why we cannot use the glider method on the mooring data. If a glider flew in a straight line through an eddy, the resulting profiles would be no different from an eddy moving past a mooring. However, if an idealized eddy were transected in a straight line through its center, its velocity vectors would be everywhere perpendicular to this line, so the variance of the radial component of velocity is zero everywhere along the line. This creates an infinite number of solutions satisfying our minimization, and the fit does not converge. Thus, the closer the transect is through the center of the eddy, the more difficulty we have obtaining a converging solution. Ultimately, what is needed for the glider method to work is the turning of velocity vectors, which is easily achieved by the glider dataset because the glider did not move in a straight line. It is also achieved for mooring transects far from the eddy center and outside of the core radius; however, in this situation one does not obtain information

about the eddy radius, R_{max}. Due to these limitations, the method outlined in section 2.4 was developed to work specifically for a mooring.

2.5.2 Results

Figure 2.6 shows the sorted properties from the two glider eddy encounters. The fit moved velocity measurements at each dive (grey arrows in panels a and b) in the direction of $-\vec{U}$ to obtain the resulting eddy velocities plotted relative to the first eddy center location (black arrows in panels a and b). The translation vector $\vec{U}$ is shown as the orange arrow in both panels. The minimization resulted in translation speeds of 0.05 m s^{-1} and 0.06 m s^{-1} for Eddy 1 and Eddy 2, respectively. Both translation values are higher than those observed at the mooring, but because these eddies were observed to the east of the mooring, they may be embedded in a stronger circulation. Density contours (panels b and f of figure 2.6) steepen closer to the eddy center. In both Eddy 1 and Eddy 2, a salty (>34.95), warm (>5.5 °C) homogeneous core extends from 200m to 700m depth, having properties similar to the mooring anticyclones.

The magnitude of the azimuthal component of velocity (with $\vec{U}$ removed) is shown in panels c and g of figure 2.6. For Eddy 1, velocities decrease slightly from the largest value of 0.28 m s^{-1} observed at about 10 km distance. This implies that the glider did not enter the eddy core, so the eddy V_{max} was not observed. Following our eddy model, R_{max} for Eddy 1 must be less than or equal to 10 km. The glider did appear to enter the core of Eddy 2, shown by the peak in velocity of 0.39 m s^{-1} (panel g), suggesting an R_{max} at about 10 km. The R_{max} values for Eddy 1 and Eddy 2 fall within the range of eddy sizes observed by the mooring. However, in both cases, eddy velocities exceeded those observed by the CIS mooring. The glider velocities are likely biased high because they have not had a low-pass filter applied to remove signals from tides, inertial currents, and other non-eddy phenomena, as was done with the mooring data. Since it is not possible to apply the same kind of filter to the glider data, glider velocities will retain the more extreme values. Geostrophic velocities calculated from the density profiles and referenced to 1000 m and are shown in panels d and h of figure 2.6. Both eddies have a subsurface maximum centered at about 400 m. The maximum geostrophic velocity of Eddy 2 occurs at R_{max}. It appears that the maximum in Eddy 1

increases toward shorter distances, and may also be maximum at its R_{max}. In the case of Eddy 1, the geostrophic velocity structure beyond about 25 km likely is not due to the eddy. Geostrophic velocities in Eddy 1 are substantially smaller than those of Eddy 2, related to less steep isopycnals in the former. This is expected if the observations in Eddy 1 are further from the center. Compared to maximum velocities observed at the mooring site, the maximum geostrophic velocities observed by the glider fall in the same range. The Rossby number for Eddy 2 is 0.26 (but we cannot compute this for Eddy 1 since we did not observe its V_{max}). This is well within the range of Rossby numbers from mooring anticyclones, and again suggests a vortex dominated by geostrophy.

2.6 Basin-wide anticyclone activity

To determine whether the anticyclones observed by the mooring and glider are representative of anticyclones found throughout the Irminger Sea, we use Argo float profiles (shown with grey circles in figure 2.7a) to find high salinity anomalies throughout the Irminger Sea and determine whether they are anticyclones similar to those observed by the mooring and glider. We do this in two ways: using satellite altimetry and salinity thresholds. The altimetry method finds the sea level anomaly (SLA) corresponding to each float profile. Float profiles taken at locations having $>$ 8 cm SLA were considered anticyclones, and each such SLA anomaly was checked for a closed contour of SLA, ensuring that meanders or filaments were not included. This method is expected to underestimate eddy numbers because of the resolution of altimetry, but positively identified profiles are likely to be eddies.

The salinity threshold method is based on our previous observations of anticyclones having anomalously high salinities. This method uses a determined salinity threshold beyond which profiles are considered anticyclones. Transects across the Irminger Sea (e.g. Våge et al., 2011a) show a gradient in salinity with low values to the west, so choosing one threshold to apply across all eddies in the Irminger Sea would be inappropriate. Instead, thresholds are defined as a local mean salinity plus one standard deviation; these values are calculated from a combination of float profiles and climatology from the World Ocean Atlas 2009 (WOA09) product. This method and the WOA09

dataset are described in detail in the Appendix. Salinity thresholds used in this method ranged from 34.92 to 34.99, spanning similar threshold values used in the CIS mooring analysis.

We first examine the properties of eddies obtained by the altimetry method. The salinity and temperature at 260m (a typical anticyclone core depth) of the float anticyclones determined by this method are plotted as grey circles in figure 2.7b, along with the mean properties from the mooring eddies (red stars). Care was taken to only examine profiles located within the blue ellipse shown in figure 2.7a; this is to avoid contaminating the data with profiles from the boundary current. The float profiles all exhibited high salinity (often $>$35.0), confirming the presence of salty anticyclones as seen by the mooring and glider throughout the Irminger basin. The highest anticyclone salinities in figure 2.7b exceed mooring anticyclone core salinities; these high values were found in the most north-east region of the Irminger basin (see figure 2.7a). Since the altimetry method likely misses some floats within anticyclones, for a more complete float eddy census, the salinity threshold method is used. A total of 130 anticyclones from 2002 to 2009 were found by the salinity threshold method, and are circled in black in figure 2.7a.

2.7 Eddy Origin

We now investigate possible origins for the anticyclones observed. The only high salinity sources in the Irminger Sea are the Irminger Current and the EGIC, an extension of the Irminger Current. To examine the basin-wide hotspots of eddy activity, we will first examine eddy kinetic energy (EKE) derived from satellite altimetry, shown in figure 2.7c. EKE is defined as

$$EKE = \frac{1}{2}(u'^2 + v'^2) \tag{2.5}$$

where u and v denote the zonal and meridional geostrophic velocities, respectively, and the prime denotes an anomaly with respect to the mean state. Here, we use the gridded AVISO geostrophic velocity anomaly product which is referenced to the 1992-2005 mean sea surface. We observe three regions of elevated EKE in figure 2.7c: just west of the Reykjanes Ridge, along the EGIC on the east coast of Greenland, and in the center

of the Irminger basin. This last region cannot be a formation site because there is no source of high salinity there, and is more likely a site of eddy 'congregation', possibly due to the deeper water there (see Huppert and Bryan, 1976a; Bretherton and Haidvogel, 1976; Carnevale et al., 1991; Cenedese and Linden, 1999). We will refer to the region of the Irminger Current west of the Reykjanes Ridge as the 'RR' region, our first potential eddy formation site. A second potential site of eddy formation is found along the EGIC just south of Cape Farewell, where the EGIC retroflects and where some eddy variability has been observed previously (see Holliday et al., 2007; Daniault et al., 2011); this site will be referred to as 'EGIC'. Both possible formation sites are circled in figure 2.7c. To illustrate the existence of Irminger Sea eddies coming from both regions, figure 2.8a and b show two drifter tracks, one passing through each site. Panel a shows a drifter trapped in an eddy at the RR region, then moving to the gyre center. The drifter in panel b follows the EGIC and breaks away near Cape Farewell, then moves towards the central gyre in a spiral, again trapped in an eddy.

Now we compare observed eddy core properties with properties from the two proposed formation sites. The Ovide cruises (whose cruise path is included in figure 2.1) crossed both the EGIC and RR regions in the summers of 2002, 2004, and 2006. Their salinity and temperature at 260m (a typical eddy core depth) is shown in figure 2.7b. There is an obvious salinity change in the Irminger Current, moving from higher salinities (> 35.1) at the RR region to 34.89-35.02 at the EGIC region. The salinities from the EGIC and the mooring eddy cores are similar. The Argo eddies have a much broader salinity range, with salinities exceeding those observed at the EGIC. These saltier eddies must be formed upstream of the EGIC, presumably at the RR region. The eddies found at the mooring site can have two origins: they can either be formed at the EGIC, or be long-lived eddies formed upstream that have lost some of their high salinity anomaly to surrounding waters as they propagated to the mooring site.

To determine which possibility is more likely, we assume that the anticyclones preserve the large-scale potential vorticity (PV), or stratification, from their formation site. We calculate PV for the EGIC and RR regions as well as for mooring and float eddies. The quantity PV describing the stratification (and ignoring the relative vorticity

term) is defined, following Talley (1988), as

$$PV = \frac{f}{\rho_o}\frac{\partial \rho}{\partial z} \tag{2.6}$$

where ρ_o is the average potential density, ρ the potential density, and z the depth. Because the salinity cores are found between 200-700m, we calculate the average PV in this layer, and all subsequent mentions of PV refer to 200-700m layer averaged PV. We assume the quantity in (2.6) is conserved until the period of winter forcing (see section 2.8 for discussion of this), since we do not observe eddies that have survived a winter. The mean PV for all Ovide stations at the EGIC and RR regions, shown by the blue and red lines in figure 2.8c, d, and e, is 2.4×10^{-11} m^{-1} s^{-1} and 5.1×10^{-11} m^{-1} s^{-1}, respectively. Both regions have a standard deviation of 0.5×10^{-11} m^{-1} s^{-1}, meaning the PV values at the two sites are statistically distinct. The higher PV at the RR is explained by the higher stratification there compared to the EGIC (see figure 8 of Våge et al., 2011a). At the RR, the Irminger Current's tilted isopycnals begin flattening around 500m, contributing to the increase in stratification and higher PV. At the EGIC, the current reaches the bottom of the basin and isopycnals do not flatten, resulting in a lower stratification and lower PV.

The histogram of PV values obtained from mooring and float anticyclones (determined by both the altimetry and salinity threshold methods mentioned earlier) are shown in the lower panels of figure 2.8. The count distribution of mooring eddy PV values (panel c) is centered around the EGIC value (almost 60% of the eddies have a PV within two standard deviations of the EGIC PV) with only a few values reaching the RR value. This suggests that mooring anticyclones are mainly formed from the EGIC region, a result supported by the preference for eddy translation to the north-east found by mooring (figure 2.4c). Float anticyclones obtained by the altimetry method (panel d of figure 2.8) show a clear preference for RR PV values, whereas the salinity threshold method (panel e of figure 2.8) produces a distribution with two peaks, one near the EGIC value, and the other at the RR value. It appears that eddies with EGIC properties are missed when determining float anticyclones from satellite. Interestingly, if we examine the tracked eddy paths produced by the Chelton algorithm, anticyclones with lifetimes greater than 16 weeks appear to be first detected exclusively over the RR region. We conclude that the satellite-based eddy detection must miss EGIC eddies because they

are smaller than eddies formed at the RR region and could not be detected.

The maximum salinities at 260m depth corresponding to each PV bin (figure 2.8f, g, and h) show all eddies detected at the CIS mooring having salinities below the maximum EGIC salinity. As for float anticyclones, maximum salinities in the eddies exceed the maximum EGIC salinity in the higher PV range. These eddies, again, must be formed upstream of the EGIC. These results suggest that both the EGIC and RR regions are formation sites for the anticyclones, and these anticyclones are found throughout the Irminger basin but have different sizes. The larger eddies observed by the floats are not encountered at the mooring.

2.8 Comparison to other North Atlantic Eddies

This section describes observed properties of eddies found in the Labrador Sea and the Norwegian Sea and compares them to our Irminger Sea observations.

2.8.1 Labrador Sea Eddies

Three types of eddies in the Labrador Sea have been observed: Irminger Current Anticyclones (ICAs), Irminger Current cyclones, and convectively formed anticyclones. The most notable contributor to the heat and salt budget in the Labrador Sea are the ICAs. They play an important role in the advection of heat into the central Labrador Sea via their thick subsurface layer of warm Irminger Current water, and contribute 25 to 100% of the heat needed to balance the surface heat loss (Rykova et al., 2009; Hátún et al., 2007; Katsman et al., 2004, L03). ICAs are formed off the west coast of Greenland where the topographic slope changes (Eden and Böning, 2002; Katsman et al., 2004; Bracco et al., 2008) and have a large sea surface height signal and elevated EKE (Prater, 2002; Lilly et al., 2003; Lavender et al., 2005). Eddy numbers peak in winter (December to March), coinciding with a peak in the sea surface height variance (Prater, 2002) and EKE (L03). Rykova et al. (2009) suggest that the ability for ICAs to maintain their structure through winters depends on the amount of surface forcing.

The published typical properties of ICAs in the Labrador Sea are summarized in table 2.2. Observed core temperatures include 4.9 °C (Prater, 2002), 3-4.15 °C (L03),

4.6-5.2 °C (Hátún et al., 2007), and 3.2-4.9 °C (Rykova et al., 2009). Core salinities include 34.85 (L03), 34.9 (Hátún et al., 2007), and 34.83-34.91 (Rykova et al., 2009). Approximate diameters range from 50 km (Prater, 2002), 30-60 km (L03) to 60-70 km (Hátún et al., 2007). All ICAs were anticyclonic with positive sea surface height anomalies and bowl-shaped isopycnals, and had surface or near-surface intensified azimuthal velocities of 20-40 cm s^{-1} (Prater, 2002), 30-80 cm s^{-1} (L03), and 50-70 cm s^{-1} (Hátún et al., 2007). These values yield Rossby numbers ranging between 0.03-0.3. Although the baroclinic nature of the ICAs is evident from the shape of the isopycnals and sheared velocity profiles, significant velocities within the ICA cores were observed even at depths exceeding 2000 m (L03). This suggests that both barotropic and baroclinic components contribute to the velocity field within an ICA.

2.8.2 Lofoten Basin Eddies

A conspicuous region of high EKE in the Nordic Seas exists in the Lofoten Basin (Poulain et al., 1996; Köhl, 2007; Rossby et al., 2009b). The eddies with an important influence on the basin's properties are warm-core anticyclones. The anticyclones form near the coast of Norway where there is a rapid slope change (Rossby et al., 2009b), and then drift west and eventually coalesce with other anticyclones in the center of the basin (Köhl, 2007). These anticyclones contain enough heat required to maintain the annually averaged heat loss in the Lofoten Basin (Rossby et al., 2009a), and serve to maintain the deep pycnocline in the center of the basin (Nilsen and Falck, 2006; Köhl, 2007; Rossby et al., 2009a).

A few ship-board and float measurements have been published on the anticyclones, and these are summarized in table 2.2. Core temperatures range from 3.5-4 °C (Köhl, 2007) to 6-7 °C (Rossby et al., 2009a), and core salinities greater than 35 were observed (Köhl, 2007). The maximum anticyclone diameter observed was about 50-60 km (Köhl, 2007; Gascard and Mork, 2008). Azimuthal velocities ranged from 13-26 cm s^{-1} (Gascard and Mork, 2008) to 30-40 cm s^{-1} (Köhl, 2007). These numbers yield Rossby numbers between 0.2-0.5.

2.8.3 Comparison to Irminger Sea Anticyclones

Individual characteristics of anticyclones from each basin spanned a broad range. The size of anticyclones at the CIS mooring is substantially smaller than the 75 km eddy reported by Krauss (1995), but is in the range of anticyclone sizes observed in the Labrador Sea and Lofoten Basins. It should be noted that often, as in the Krauss (1995) study, eddy sizes are determined by the extent to which salinity or temperature is anomalous, and not by our definition of the core radius where maximum velocities are observed. Our observations show that the extent of the salinity (and temperature) anomaly can exceed the core radius by a factor of two or more at times, so our reported eddy sizes are by definition smaller than those observed by other studies. To make this difference clear, the eddy diameters reported in Table 2.2 are separated into diameters calculated from R_{max} and from property anomalies (estimated as $4R_{max}$ for our mooring and glider eddies). Maximum observed azimuthal velocities in our eddies were in the low range of velocities found in the other two basins. All anticyclones had low ($\ll 1$) Rossby numbers, signifying dynamics dominated by geostrophic balance. Most ICAs in the Labrador Sea had surface or near-surface velocity maxima, whereas the Lofoten and Irminger anticyclones had more sub-surface intensified velocity structures. Anticyclones in the Labrador Sea experience maximum numbers in winter months; the opposite appears to be true for the Irminger Sea anticyclones. Figure 2.2 shows anticyclone occurrences mainly in the summer months. During winter months, mixing down to at least 400m is observed, and any observed remnants of high salinity anomalies do not have associated turning velocities that would indicate a coherent vortex. This suggests that at the mooring site, anticyclones may experience strong enough surface forcing to be destroyed during winter.

Despite the eddies' differences, we can generalize: lens-like anticyclones are observed in all three high-latitude North Atlantic basins that we have examined. Although individual properties vary, their broad characteristics are the same. All anticyclones form from a boundary current over steep topography, suggesting that baroclinic instabilities produced from topography (see Wolfe and Cenedese, 2006) can be a ubiquitous formation mechanism for lens-like anticyclones in the subpolar North Atlantic.

In both the Labrador Sea and Lofoten Basins, anticyclonic eddies play an impor-

tant role in balancing winter heat loss due to their anomalous warm cores. This is likely also the case for Irminger Sea, where warm anticyclones have the potential to contribute to the heat balance of the Irminger Sea. In the Labrador Sea, the anomalously fresh anticyclones balance the freshwater budget (Hátún et al., 2007); analagously, our Irminger Sea anticyclones have the potential to contribute to the freshwater budget due to their anomalous salinity signature.

2.9 Discussion

At the CIS mooring, we have observed warm, salty anticyclones that are found throughout the Irminger basin. Eddies observed at the mooring are of EGIC origin, and eddies originating from the RR region do not typically reach the mooring location. The benefit of the mooring and glider observations is the ability to obtain a detailed, quantitative representation of eddy structure and frequencies that cannot be done with existing datasets spanning large spatial domains.

Although our analysis suggests two separate formation regions for the Irminger Sea anticyclones, satellite altimetry appears to identify only one of them. As mentioned, the gridded satellite altimetry product dampens eddy signals smaller than 40 km (Chelton et al., 2011). The mooring anticyclones had a mean R_{max} of 6 km; since this corresponds to eddy sizes of 24km, most of the altimetry signal of these eddies will be dampened. This suggests that the eddies detected by satellite altimetry and that appear to form at the RR region are larger than those observed at the mooring site. Because we do not observe the larger eddies at the mooring, we do not have sufficient data to analyze them.

The horizontal scales of the eddies observed in the CIS appear to scale with the first baroclinic Rossby radius of deformation, R_1 (Emery et al., 1984; Chelton et al., 1998). We calculate this quantity following Emery et al. (1984) and compare it to our observed eddy scales. As in Emery et al. (1984), values of the squared buoyancy frequency are linearly extrapolated from the deepest measurement to zero at the sea floor. We calculate R_1 using our available datasets. The mean R_1 obtained from the mooring, glider, Argo floats, and Ovide transects is 5.6 km, 7.0 km, 7.5 km, and 10.7 km, respec-

tively. The most unstable wavelength, L_1, of the baroclinic instability process is given by $L_1 = 2\pi R_1$ (Emery et al., 1984; Stammer and Böning, 1992). The diameter of eddies resulting from this instability is expected to be $L_1/2$. Our R_1 values predict eddies to have a diameters of 17.7 km, 22.0 km, 23.7 km, 33.6 km from the data sources listed previously. This expected eddy diameter should be compared to our observations of the size of the salinity or temperature anomaly of 4 R_{max} from our analyses (table 2.2). Our observed anticyclone sizes fall within the range of diameters predicted from the first baroclinic Rossby radius.

This study has focused on anticyclonic eddies with warm and salty core anomalies found in the Irminger basin. We have concentrated on these eddies because of their analagous traits to anticyclones in the Labrador and Norwegian Seas, and their potential for influencing budgets of the Irminger Sea. These anticyclones appear to be a general feature of subpolar North Atlantic basins. Further work must be done to determine the impact and fate of the anticyclones in the Irminger Sea. As mentioned, the eddies at the CIS mooring show interannual variability in occurrence, and their core salinity shows an increase over the timeseries. We expect this to be an important source of salt for the Irminger Sea, and a quantitative analysis using the eddy statistics from this study will be done in Chapter 3.

Chapter 2, in full, is a reprint of the material as it appears in Xue Fan, Uwe Send, Pierre Testor, Pascale Lherminier, Johannes Karstensen, 2013. "Observations of Irminger Sea Anticyclonic Eddies", *Journal of Physical Oceanography*, 43, 805 – 823. The dissertation author was the primary investigator and author of this paper. This work would have not been possible without the invaluable contributions from the co-authors, Uwe Send, Pierre Testor, Johannes Karstensen, and Pascale Lherminier. We would like to thank the teams of LPO/IFREMER, LOCEAN/CNRS, PO/IFM-GEOMAR, and PORD/SIO for performing the 2006 Spray glider mission, and specifically Thierry Terre (LPO) and Jeff Sherman (SIO) for making the mission possible. Gratitude goes to the reviewers and Sarah Gille for valuable advice on the manuscript. This work benefitted from discussions with George Carnevale and William Young. Funding for the CIS mooring was provided by the European Ocean Observatory Network (EuroSITES) and the glider was operated with MERSEA support. Altimeter data was provided via the

AVISO website (*www.aviso.oceanobs.com*). Argo data was provided by the USGADAE Project website (*www.usgodae.org*). Drifter data was provided by the NOAA AOML Global Drifter Program website (*www.aoml.noaa.gov/phod/dac/index.php*).

Table 2.1: CIS Mooring configuration and instrumentation example taken from the CIS 3rd deployment (2004). Note that not every MicroCAT has a pressure sensor, and pressures are interpolated for measurements that do not have their own pressure sensor. The second MicroCAT is part of a slack surface telemetry unit that does not have tension pulling the wire vertical.

NominalDepth	*Instrument*	*Measurement*
10 m	SBE MicroCAT IM	S,T
10-30 m	SBE MicroCAT IMP	S,T,P
70 m	SBE MicroCAT IM	S,T
109 m	SBE MicroCAT IM	S,T
150 m	Teledyne-RDI Workhorse (upward)	U,V,W velocities 0m-150m, P
153 m	Teledyne-RDI Longranger ADCP (downward)	150m-720m, P
155 m	SBE MicroCAT IM	S,T
197 m	SBE MicroCAT IM	S,T
267 m	SBE MicroCAT IMP	S,T,P
372 m	SBE MicroCAT IM	S,T
548 m	SBE MicroCAT IMP	S,T,P
748 m	SBE MicroCAT IM	S,T
998 m	SBE MicroCAT IMP	S,T,P
1004 m	Aanderaa RCM-8 AVTP	T,P,U,V point velocities
1245 m	SBE MicroCAT IMP	S,T,P
1496 m	SBE MicroCAT IM	S,T
2283 m	McLean Sediment Trap	Sediment accumulation
2327 m	Aanderaa RCM-8 AVT	T,U,V point velocities

Table 2.2: Summary of properties of anticyclones found in various basins in the North Atlantic. Columns are: Diameter (D, km) calculated from R_{max} , Diameter (D (Anom.), km) estimated by the salinity or temperature anomaly (and estimated as $4R_{max}$ for our mooring and glider eddies), Temperature (Temp,°C), Salinity (Sal), Maximum observed velocity (cm s^{-1}), and Rossby number (Rossby). The diameter ranges for eddies observed at the mooring are reported as one standard deviation about the mean observed eddy diameter.

	D	*D(Anom.)*	*Temp*	*Sal*	V_{max}	*Rossby*
Labrador Sea	10-70km	25-65 km	3-4.9 °C	34.83-34.91	20-80 cm s^{-1}	0.03-0.3
Lofoten Basin		50-60 km	3.5-7 °C	>35	13-40 cm s^{-1}	0.2-0.5
Irm. Sea (mooring)	4-21 km	8-42 km	4.2-5.3 °C	34.97-35.01	3-21 cm s^{-1}	0.01-1 (mean 0.3)
Irm. Sea (glider)	20 km	40 km	5.5 °C	34.91-35.01	30-36 cm s^{-1}	0.26
Irm. Sea (Argo)			3.6-7.7 °C	34.8-35.15		

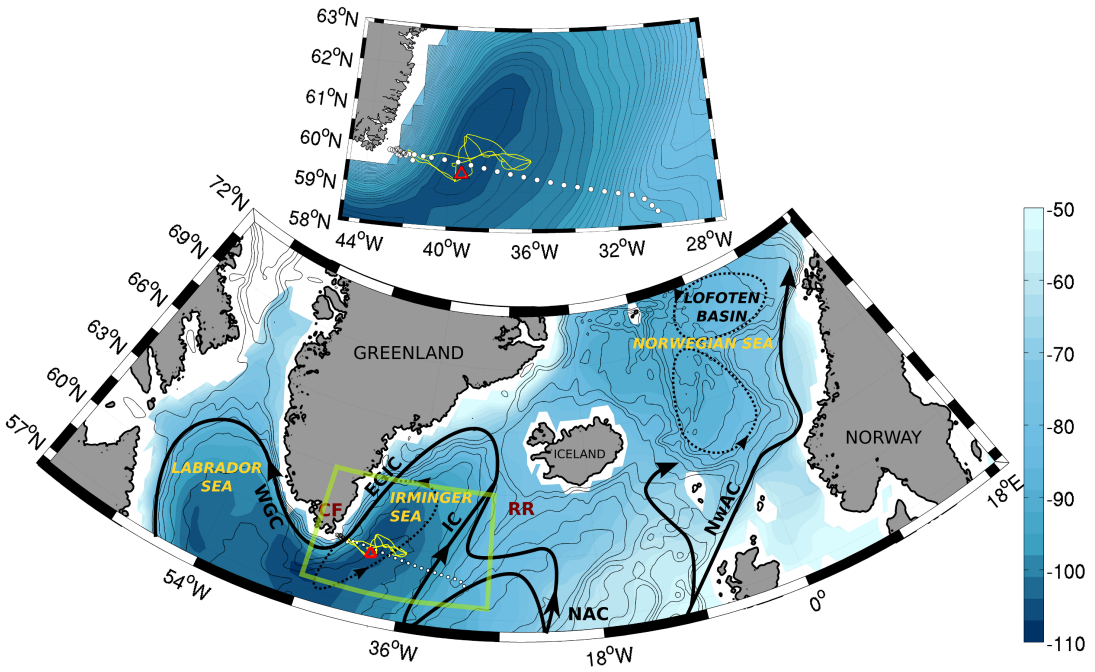

Figure 2.1: Map of basins and current systems of study area. Solid black pathways show a schematic of the general upper currents adapted from Schott et al. (2004); Köhl (2007); Daniault et al. (2011). The major currents are: the West Greenland Current (WGC), East Greenland-Irminger Current (EGIC), Irminger Current (IC), North Atlantic Current (NAC), and Norwegian Atlantic Current (NwAC). Dotted black pathways show recirculation patterns in the Irminger Sea and Norwegian Sea. Blue colors represent the 1992-2002 mean surface dynamic ocean topography (in cm) obtained from Nikolai Maximenko (IPRC) and Peter Niiler (SIO) (Maximenko et al. (2009)). Thin black contours represent the bottom topography in 500 m intervals. Geographic features, in red text, are the Reykjanes Ridge (RR), and Cape Farewell (CF). The green line marks the boundaries of the inset. Inset: the yellow line shows the glider path, the red triangle represents the CIS mooring location in the center of the gyre, and the white circles show ship hydrographic stations from the Ovide cruises. Black lines and blue color contours represent the mean dynamic topography (same as in lower figure) to highlight the mooring's location in the center of the lowest surface dynamic topography.

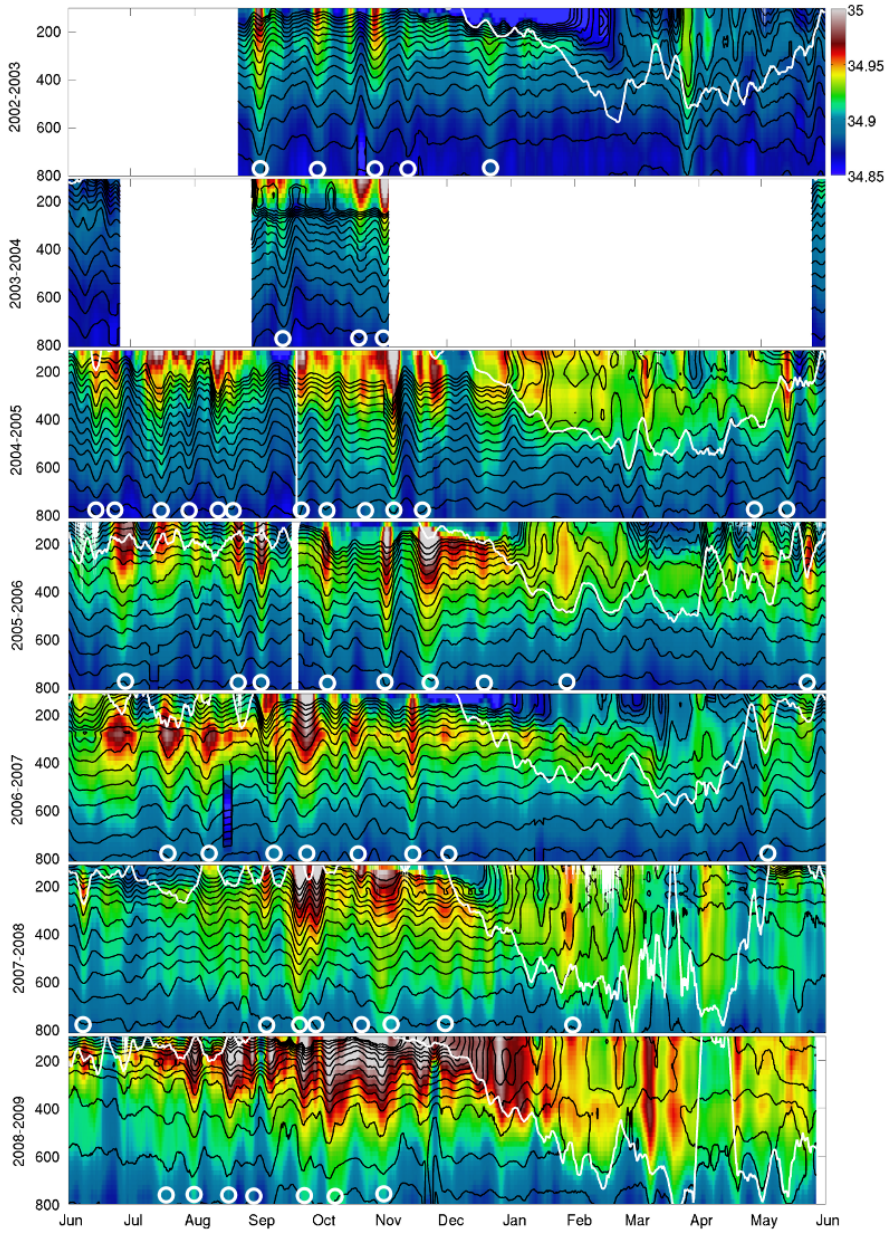

Figure 2.2: Color depth-time display showing salinity from 7 years of CIS mooring deployment. Solid lines are potential density contours, plotted with a spacing of 0.01 $kg\ m^{-3}$. The white line represents the mixed layer depth calculated by a threshold difference of 0.5 °C from the surface temperature. A running mean is applied to the data at each pressure level with a 3-day time window. Identified anticyclones are indicated by white circles found at the bottom of their profiles. This includes eddies whose cores were not transected as well as 'likely' anticyclones (9 total) which had a typical salinity anomaly signature and turning velocities, but an atypical hodograph.

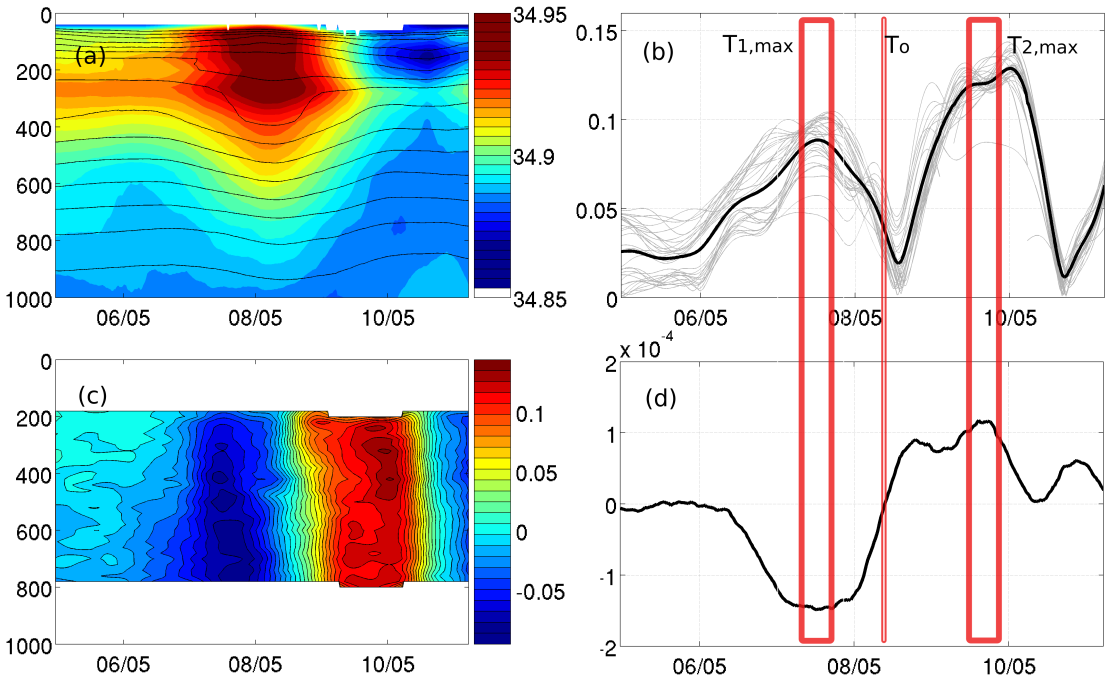

Figure 2.3: An example of one mooring eddy and the method to determine V_{max} and $T_\circ$. a: Salinity in color contours with black potential density contours (in intervals of 0.01 kg m^{-3}, starting from 1027.74 at the bottom contour). b: Observed magnitude of velocity signal (in m s^{-1}) from all levels during eddy passing (thin grey lines) and their column average (thick black line). c: Observed velocity signal perpendicular to the advection direction (in m s^{-1}) plotted against depth and time. d: Depth-averaged dp/dt (in dbar s^{-1}) derived from the density data. The two thick red boxes indicate the minimum and maximum points used in the algorithm, and the thin red box shows the location of $T_\circ$, where dp/dt crosses zero.

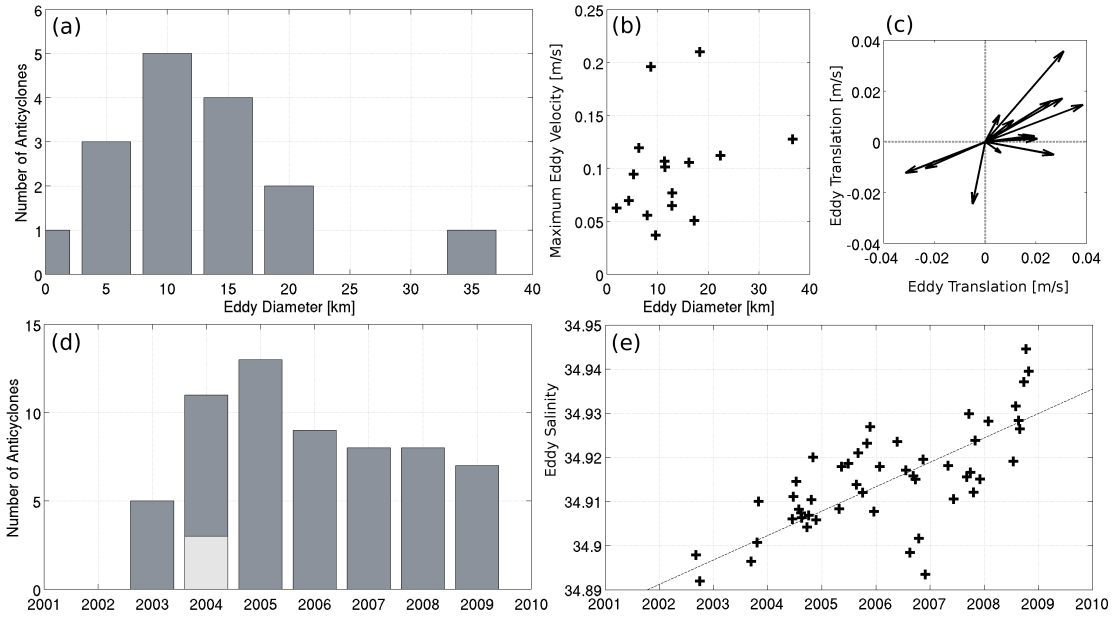

Figure 2.4: Results from eddy census using the mooring algorithm. (a): Number of anticyclones found at a given diameter scale ($2R_{max}$, in km). (b): Maximum velocities (in m s^{-1}) encountered at each anticyclone plotted against diameter. (c): The translation vector for each anticyclone encounter. (d): Number of eddies each year, counted between Junes of each year. The bar placed at year 2003 represents the June 2002 to June 2003 counts, and so on. This count includes eddies whose cores were not observed as well as 'likely' anticyclones (9 total) which had a typical salinity anomaly signature and turning velocities, but an atypical hodograph. Note that between June 2003-2004, there were very few mooring data, resulting in the low eddy number shown in the light grey bar. We estimate the total number of eddies which would have been observed during this period if we had a full dataset by dividing the eddy count by the time fraction during which data are available that year. This estimated count is shown in the dark grey bar. (e): The surface to 1000 m mean eddy salinities plotted against date of occurrence. The dotted black line represents the fitted linear trend.

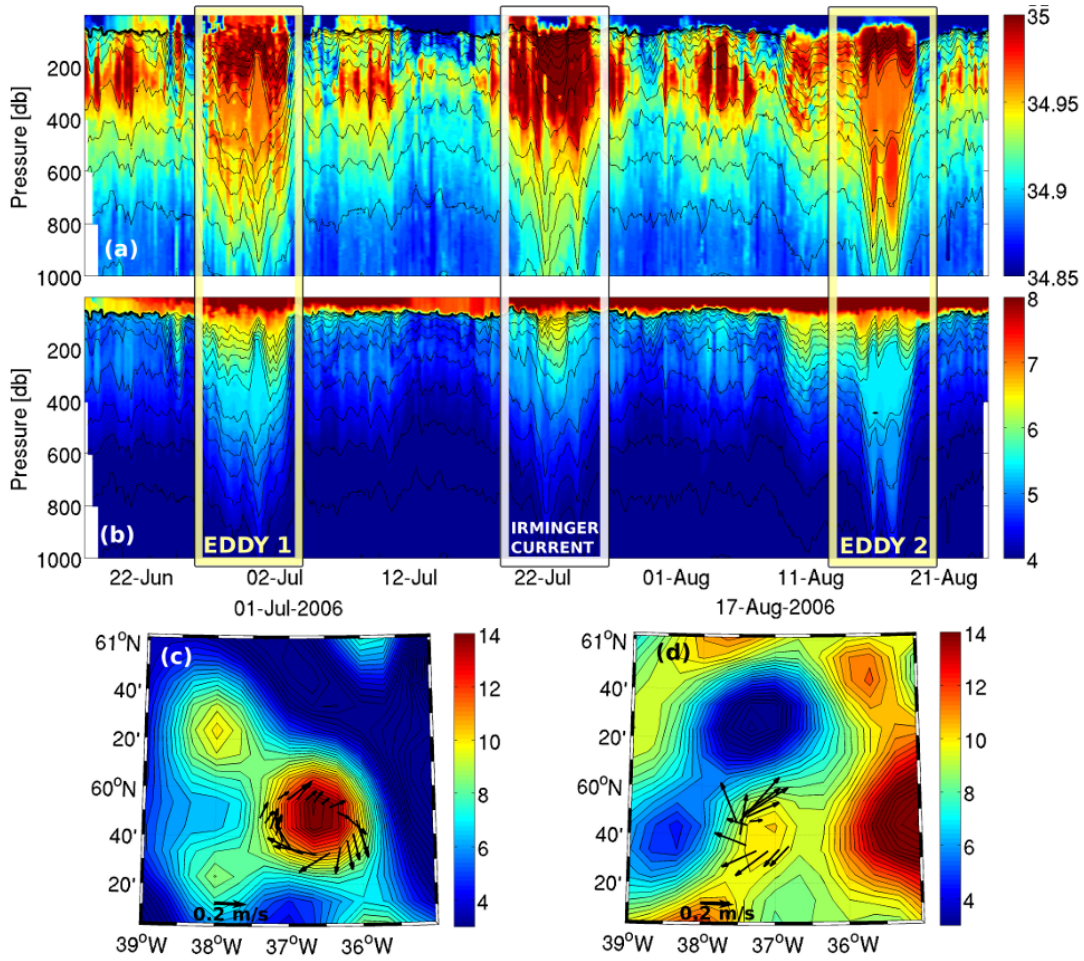

Figure 2.5: Glider profiles showing eddies. (a): Salinity in color with potential density contours in black (0.02 kg m^{-3} apart). (b): Potential temperature (°C) in color with potential density contours in black (0.02 kg m^{-3} apart). Eddy 1 (left) and Eddy 2 (right) are highlighted in yellow, along with a crossing of the Irminger Current (in white). Between Eddy 1, the Irminger Current, and Eddy 2, patches of lens-like high salinity features are observed. The density of these features is similar to that of the Irminger Current, and they are likely to be subsurface filaments from the current and not an eddy feature. (c) and (d): Depth-averaged current vectors from glider measurements and SLA (in cm) from satellite altimetry on a date near the eddy encounters.

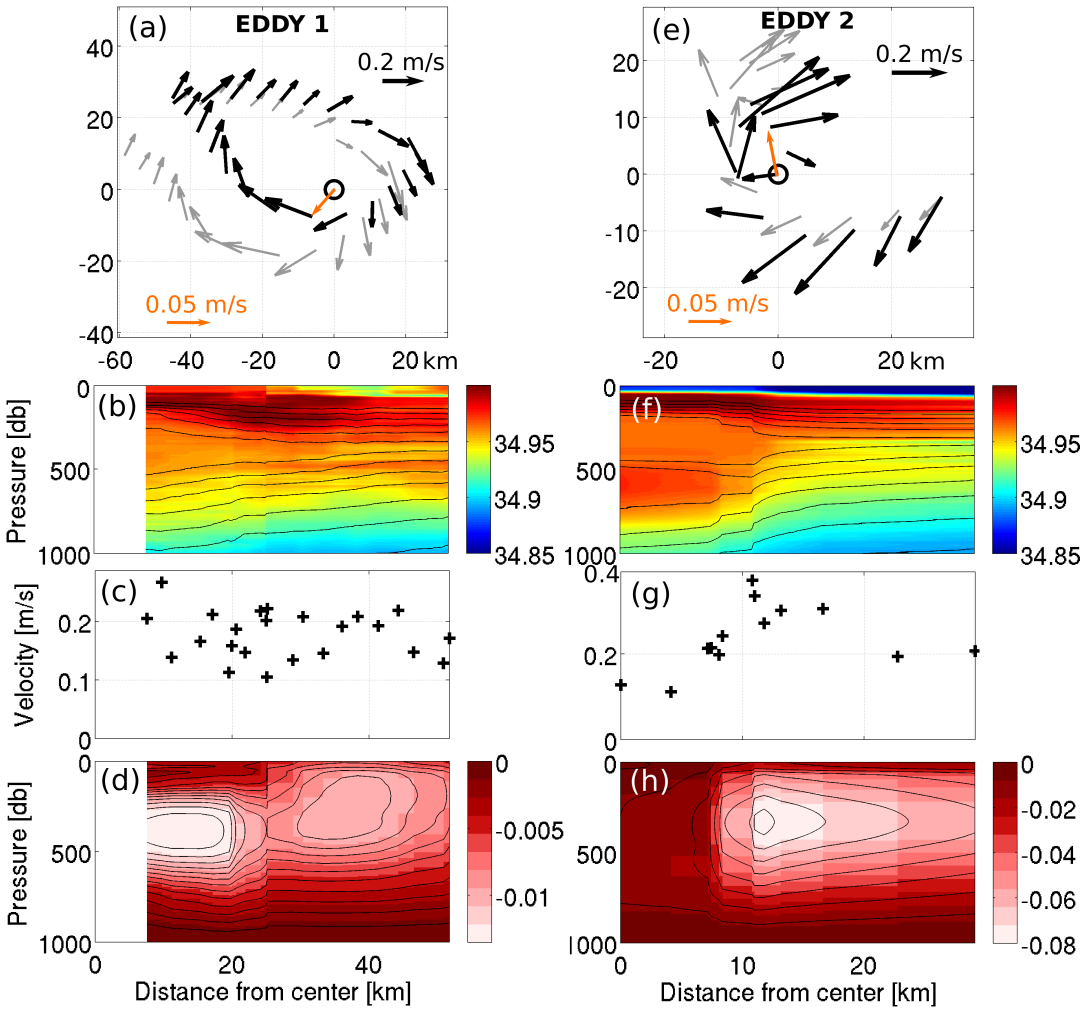

Figure 2.6: Sorted glider profiles from Eddy 1 (left) and Eddy 2 (right). (a) and (e): Depth-averaged velocity vectors before (gray) and after (black) applying the method described in the text. The gray vectors show velocity measurements with respect to the eddy center of the first dive. The scale for both the gray and black vectors is the black arrow in the top right corner. The orange vector represents the direction of the translation velocity obtained from the fit, and its scale is the orange arrow in the bottom left corner. The black arrows have the translation velcity removed. (b) and (f): Color contours of salinity and line contours of potential density (with 0.02 kg m^{-3} contour spacing), plotted against distance from the eddy center. (c) and (g): Magnitude of the tangential component of the depth-averaged velocity (m s^{-1}) after data method is applied, plotted against distance from the eddy center. (d) and (h): Geostrophic velocity (m s^{-1}) referenced to 1000 m, with negative values coming out of the page, plotted against distance from the eddy center.

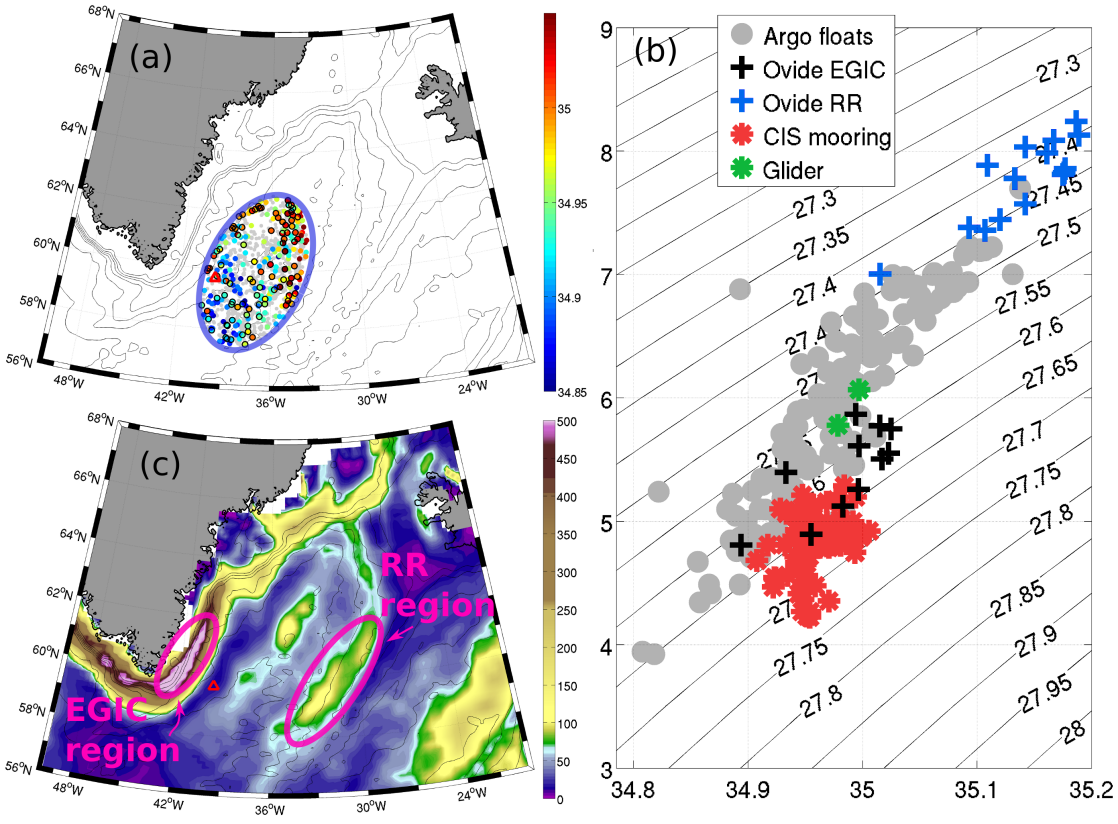

Figure 2.7: Argo float data indicating profiles within anticyclones, TS plots, and basin EKE. (a): Argo float data from 2002 to 2006, showing salinities at 260 m depth. Floats within the ellipse shape are considered for eddy search. Grey circles represent all float data, and floats showing color represent measurements assumed to be uncorrelated. Circled in black are profiles identified as eddies using the salinity theshold method. The colors within circles represent the salinity at 260 m. The red triangle marks the CIS mooring location. (b): Temperature-salinity plot of measurements (at 260 m depth) of float profiles within anticyclones determined by the altimetry method (grey circles). Anticyclone properties at 260 m depth from the mooring and the glider are represented with red and green stars, respectively. Ovide transects through the RR region (blue crosses) and EGIC (black crosses) are also plotted at 260 m. (c): Mean EKE (in cm^2s^{-2}) calculated from satellite altimetry-derived geostrophic velocity anomaly averaged over 2000-2009. Black lines define contours of topography (500 m apart). The red triangle marks the CIS mooring location. Two formation regions are circled: the Reykjanes Ridge region (RR) and the East Greenland-Irminger Current region (EGIC).

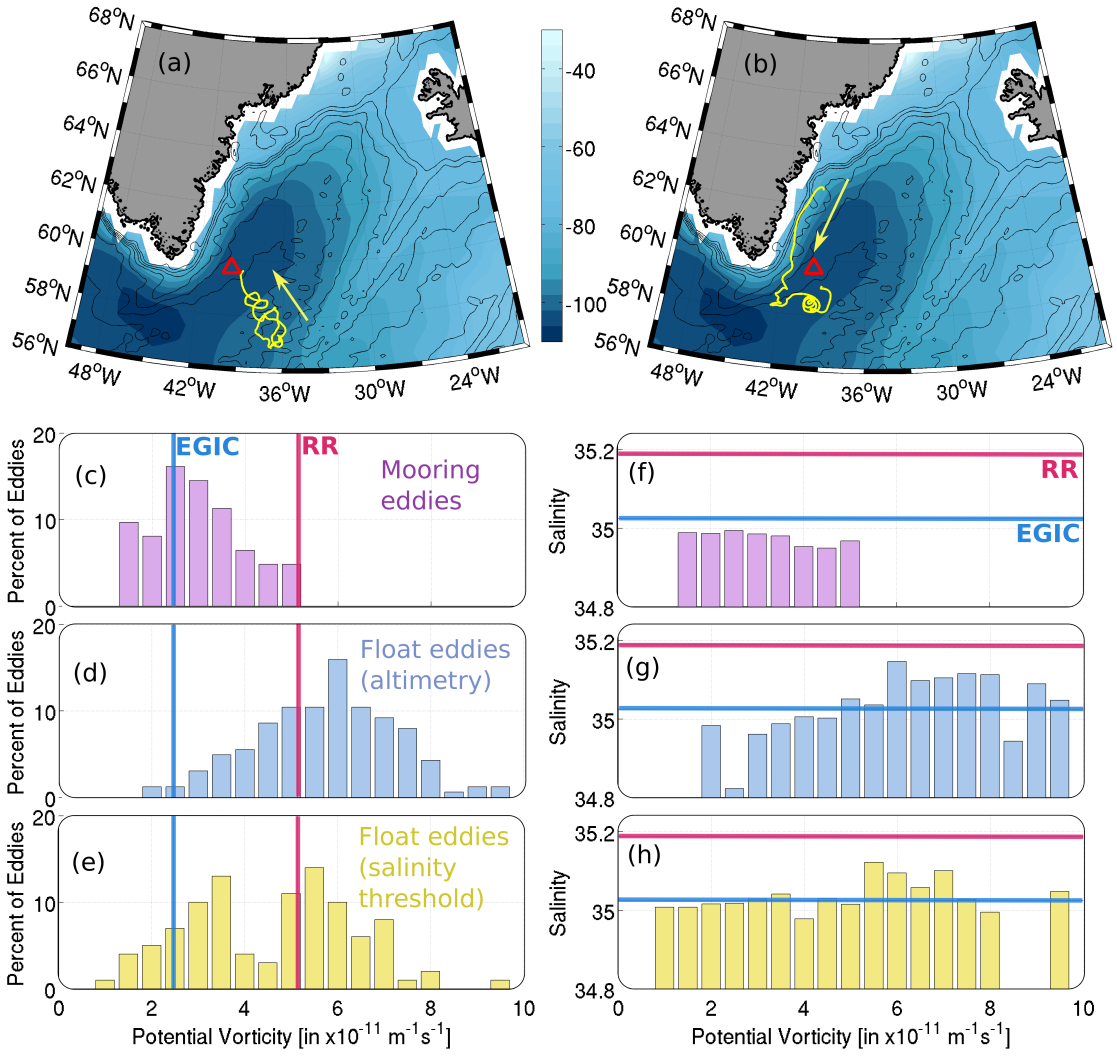

Figure 2.8: Drifter tracks and eddy formation regions. (a) and (b): Drifter tracks showing an instance of an eddy originating from the RR region (a) and the EGIC region (b). The blue color contours represent the mean dynamic topography (in cm) displayed and described in figure 2.1. Black contours show the bottom topography in 500 m increments. Yellow arrows indicate the direction of movement of the drifter. (c): Histogram of 200-700 m averaged PV calculated from mooring anticyclones. (d) Same as (c), but for Argo float anticyclones determined by the altimetry method. (e) Same as (c), but for Argo float anticyclones determined by the salinity theshold method. In panels (c)-(e), the blue line indicates the mean PV at the EGIC region, and the red line, the mean PV at the RR region (determined from Ovide ship measurements). (f), (g), (h): Maximum observed salinity corresponding to each PV bin for anticyclones shown in figures (c), (d), and (e), respectively. The maximum salinities observed at the EGIC and RR regions are shown with the blue and red lines, respectively.

Chapter 3

Quantifying Irminger Sea Budgets

3.1 Abstract

We quantify the terms in the heat and salt budget in the upper (<460 m) layer of the Irminger Sea at the CIS mooring location (59.7 ^oN, -39.7 ^oW). For the case of both heat and salt, surface forcing and eddy advection terms are leading terms in the balance over the 7-year mooring timeseries, whereas the horizontal advection by the mean current is small. Vertical fluxes are small at the base of the 460m layer. Estimates of the magnitude of horizontal heat and salt advection not attributed to the eddy term or advection by the mean current show that its size may be as large as the eddy term over the 7-year period. On very long timescales, these leading terms must balance, but over the 7-year record analyzed a temperature decrease and salinity increase is observed. The correlation between the NCEP surface heat flux and the North Atlantic Oscillation (NAO) index is used to determine that over the mooring time period, surface heat loss is larger compared to a longer-term (150-year) mean. This imbalance is enough to explain the temperature decrease observed. A salinity increase is observed over the 7-year timeseries in the upper layer. Results from NCEP and ECMWF surface freshwater flux products suggest that during the mooring period, less net freshwater than normal is input into the Irminger Basin via surface fluxes, which can explain the salinity increase. Although the decrease in temperature and increase in salinity is controlled by the change in surface forcing, the anticyclones are a controlling factor in the heat and salt budget over the mooring timeseries. Over shorter (1-year) time scales, the magnitude of the an-

ticyclonic eddy heat and salt term remains comparable to the 7-year mean, but the other terms in the budget become large and dominate the balance. We examine the uncertainty of the surface flux terms, and determine that the NCEP freshwater flux is over-estimated by an order of magnitude.

3.2 Introduction

The Central Irminger Sea (CIS) is in the northern region of the North Atlantic Ocean, and has diverse oceanographic influences including the warm and salty subtropical North Atlantic Current and the dense overflow waters formed in the Arctic Ocean (Dickson et al., 2007). From the perspective of global climate, the CIS plays a role in ventilating intermediate mode waters of the North Atlantic through wintertime convection (Pickart et al., 2003). Although the general circulation within the CIS is generally understood (e.g. Lavender et al., 2000; Sutherland and Pickart, 2008), relatively little is known about the variability of the boundary currents, the interior flow, and deep convection.

The upper and intermediate depths of the CIS basin are comprised of Irminger Sea Water (ISW) and Labrador Sea Water (LSW), respectively. The boundary between the two water masses is determined by the 27.7 $kg\ m^{-3}$ isopycnal (Våge et al., 2011b). The LSW layer is characterised by relatively low stratification and low salinity. It has been argued that LSW can be formed in the CIS due to convection forced by atmospheric tip jet events (Pickart et al., 2003), and observations in the CIS have provided evidence that deep mixing did indeed occur in some winters (e.g. Bacon et al., 2003; Våge et al., 2008b). However, the notion of deep convection occuring in the Irminger Sea has been questioned; Yashayaev et al. (2007) argue that weakly stratified intermediate water found in the CIS is predominantly advected from the Labrador Sea on relatively short ($\sim$ 2 years) timescales, and Bersch et al. (2007) suggest that a continuously present intermediate salinity maximum across the Irminger Basin indicates that there was no significant formation of LSW in the CIS after 1991. Despite the unclear origin of the LSW found in the CIS, the LSW forms a significant intermediate water mass found in the CIS, and contributes to the CIS basin's mean properties. Further de-

termining the properties of the basin are influences from the sea surface, how they affect the ISW, and in turn how the ISW and LSW interact. Thus, the variability of the properties of the ISW plays an important role in setting the properties and stratification of the basin as a whole.

An important phenomenon contributing to the variability of the ISW are mesoscale anticyclonic eddies (Fan et al., 2013). These anticyclones carry warm ($>$ 5°C) and salty ($>$ 34.9) water into the CIS basin, with the strongest signal in the ISW layer. They originate from various formation regions along the Irminger Current and propagate into the basin interior. The highest eddy activity was observed in summer and fall months, and vigorous mixing events during winter obscured the eddy velocity signatures, potentially destroying the eddies. Their very homogeneous cores set up a minimum stratification zone locally, but also introduce heat and salt fluxes and subsequent mixing into the gyre interior.

The purpose of this study is to determine how much anticyclonic eddies contribute to the CIS basin heat and salt budget by examining the ISW layer. This is treated as follows. A combination of different observations and reanalyses (section 3.3) is used to calculate the terms in the Reynolds averaged heat and salt conservation equations (section 3.4). The balance of the terms is examined over the 7-year mooring data period (sections 3.6 and 3.7), over longer periods (sections 3.8), and over yearly timescales (sections 3.9 and 3.10). Vertical fluxes are estimated in section 3.12, and conclusions are presented in section 3.13.

3.3 Data

3.3.1 CIS Mooring Data

The CIS mooring is located in the Central Irminger Sea Gyre (at 59.7°N 39.7°W, shown in figure 2.1) in a region of minimum stratification corresponding to the center of the gyre as defined in Våge et al. (2011b). The mooring began its data recording from September 2002 and is presently still active. Since the first deployment, the CIS mooring has been collecting physical variables at 20-minute invervals with Seabird microcats, recording temperature, conductivity, and pressure at approximately 11 different depth

levels, from 100m to 1600m depth. Starting in 2003, a mix of rotary current meters and acoustic doppler current profilers (ADCP) were added. Physical data from the CIS mooring were pre- and post-calibrated at each mooring servicing. A more complete overview of the CIS mooring deployments and calibration techniques is available from Fan et al. (2013) and Karstensen (2005). Apart from the quality control applied to all CIS mooring data, all variables (temperature, salinity, and ADCP velocities) were interpolated onto the common time axis of hourly intervals, and a 10 dB pressure grid. The salinity data are converted to absolute salinity units of kg/kg (Wright et al., 2011). Fan et al. (2013) developed a method to isolate anticyclonic eddies passing the mooring. The resulting statistics associated with these eddies will be used in this study. The method used to estimate eddy fluxes is described in detail in section 3.6.3.

3.3.2 NCEP/NCAR and ECMWF

We use the daily averaged National Centers for Environmental Prediction (NCEP) National Center for Atmospheric Research (NCAR) Reanalysis II gridded product (Kalnay et al. (1996)) for the period of 2002-2010 to determine surface heat and freshwater fluxes at the CIS mooring location. Heat flux variables of interest include sensible and latent heat flux, and long- and short-wave radiation. The NCEP/NCAR Reanalysis is a dynamically consistent reanalysis with data assimilation performed on a horizontal grid of 2.5° by 2.5°. Information and data can be found at their website ($http://www.cpc.ncep.noaa.gov/products/wesley/reanalysis2$). Previous studies have shown that the sensible and latent heat fluxes from the NCEP Reanalysis are biased in the North Atlantic (see Josey, 2001; Bumke et al., 2002). We re-calculate these fluxes according to the methods outlined by Bumke et al. (2002) to eliminate the bias and improve the net surface heat flux uncertainty. Details for this procedure are found in the appendix. Freshwater variables used are precipitation and evaporation (calculated from the latent heat flux).

To compare with the NCEP product, we also use the European Centre for Medium-Range Weather Forecasts (ECMWF) gridded reanalysis product. The ECMWF grid spacing is 100km by 100km. Details about this reanalysis product can be found through Persson and Grazzini (2005), and data can be obtained from their website

($http://www.ecmwf.int/research/era/do/get/index$).

3.3.3 Satellite Altimetry

The gridded merged AVISO product was used in Fan et al. (2013) in order to provide a spatial view of eddy activity. Details about the product can be found in that study. A global eddy census using this dataset was produced by Chelton et al. (2007); it identifies and tracks coherent mesoscale eddies globally from 1992 to 2008. Details of the eddy tracking algorithm can be found in Chelton et al. (2011). The dataset produced by this study will be used as an independent estimate of eddy counts, which lead to estimates of the eddy heat and salt fluxes.

3.3.4 WOA Climatology

World Ocean Atlas 2009 (WOA09) is a set of objectively analyzed (1^o grid) climatological fields of in situ temperature, salinity, and other variables at standard depth levels for annual, seasonal, and monthly compositing periods for the World Ocean. In this study, the temperature and salinity fields are used; their respective detailed descriptions can be found in Levitus and Boyer (1994) and Antonov et al. (2006). The data is publicly available from the National Oceanographic Data Center ($http://www.nodc.noaa.gov/$).

3.3.5 Argo Floats

Argo floats within the Irminger Sea provide profiles of temperature and salinity from the surface to 2000 m depth approximately every 10 days. Each float drifts at 1000 m for about 10 days, then descends to 2000 m and rises to the surface over 6 hours, collecting measurements on ascent. At the surface, data are transmitted and the float's location is determined. The float then dives back to 1000 m to repeat its 10-day cycle. The data from these floats are available through the International Argo Project and can be found through the GODAE project server ($http://www.usgodae.org/Argo/Argo.html$).

This study uses two objectively mapped products resulting from the Argo dataset, as described by Roemmich and Gilson (2009) and by Hosoda et al. (2008). The first we refer to as RG2009 (available at $http://sio-argo.ucsd.edu/RG\_Climatology.html$) and the second, as H2008 (found at $http://www.jamstec.go.jp/ARGO/argo\_web/MapQ/Mapdataset\_e.html$). Both products are 1^o gridded maps of monthly global temperature and salinity values with depth covering 2004-present (RG2009) and 2002-present (H2008). Both datasets use covariance functions with decorrelation scales obtained from observations.

3.4 Equations for upper ocean heat and salt balance

Classically, the upper 'Irminger Sea Water' is defined as the Irminger Sea surface waters with density $< 1027.70\ kg\ m^{-3}$(Våge et al., 2011b). The mean depth of this layer division occurs between 400 m and 500 m depth in the mooring data, with a mean at 460 m. This depth lies below the seasonal mixed layer (except during very deep convection events) and encompasses a large part of the eddy temperature and salinity signal. To simplify the upper layer budget calculation, we define the 'upper layer' to be from the surface to a constant depth of 460 m, and examine the heat and salt budget terms as a depth-average over this layer.

We begin with the upper layer heat tendency equation presented in Moisan and Niiler (1998), assuming a constant layer depth. The heat budget for the upper ocean is calculated from the three-dimensional heat conservation equation,

$$\rho_o c_p \left(H \frac{\partial T_a}{\partial t} + H \mathbf{v}_a \cdot \nabla T_a \right) = Q_{net}, \tag{3.1}$$

where ρ_o is a reference density, c_p the specific heat of seawater, and T_a the depth-averaged temperature and $\mathbf{v}_a$ is the depth-averaged horizontal velocity over the layer. Here, $\nabla \equiv (\partial/\partial x, \partial/\partial y)$ and Q_{net} is the net heat flux across the ocean surface. The layer depth, H is constant at 460 m, as mentioned earlier. We will neglect the vertical terms in the original equation presented in Moisan and Niiler (1998). During very deep convection events we might expect significant vertical heat fluxes to occur. These events are sporadic and do not occur every year (e.g. Vage 2011). We show in section

3.12 that vertical fluxes are small at the mooring location compared to the other terms, even during the deep convection events.

We follow the triple decomposition outlined by Reynolds and Hussain (1972) and by Piquet (1999), where a signal f is decomposed into three components:

$$f = \overline{f} + \widetilde{f} + f' \tag{3.2}$$

Here, $\overline{f}$ represents a mean (time-average) contribution, and is defined as

$$\overline{f} = \frac{1}{t_f - t_i} \int_{t_i}^{t_f} f(t)\, \mathrm{d}t, \tag{3.3}$$

where t_i and t_f are the initial and final points of the time mean. The $\widetilde{f}$ term represents the large-scale *organized* part of the fluctuation in the form of an eddy. We specifically define this term to represent the contribution from the warm and salty anticyclonic eddies observed in Fan et al. (2013). The f' term represents non-organized or longer time-scale motion contributions from scales and phenomena other than the anticyclonic eddies. We define $T_a = \overline{T}_a + \widetilde{T}_a + T'_a$ and $\mathbf{v}_a = \overline{\mathbf{v}}_a + \widetilde{\mathbf{v}}_a + \mathbf{v}'$, and substitute these into (3.1). After simplifying and applying rules of Reynolds averaging, we have

$$\underbrace{H\frac{\partial \overline{T}_a}{\partial t}}_{1} = \underbrace{-H\overline{\mathbf{v}}_a \cdot \nabla \overline{T}_a}_{2} - \underbrace{H\overline{\widetilde{\mathbf{v}}_a \cdot \nabla \widetilde{T}_a}}_{3} - \underbrace{H\overline{\mathbf{v}'_a \cdot \nabla T'_a}}_{4} + \underbrace{\frac{\overline{Q_{net}}}{\rho_o c_p}}_{5}. \tag{3.4}$$

The derivation of equation (3.4) can be found in the appendix. From left to right, terms represent the mean temperature tendency, the advection by the mean current on the mean temperature gradient, the anticyclonic eddy horizontal temperature advection, the horizontal temperature advection from non-eddy and non-mean contributions, and the net heat flux through the surface. Note that the overbar represents a time average over the period of interest. In this study, we perform time averages (overbar operation) over different time scales to examine the budget terms over these scales.

Likewise, we can derive equations for the salt balance using the depth-averaged salinity, $S_a = \overline{S_a} + \widetilde{S}_a + S'_a$. The final equation for the salt balance in the upper 460m is:

$$\underbrace{H\frac{\partial \overline{S}_a}{\partial t}}_{1} = \underbrace{-H\overline{\mathbf{v}}_a \cdot \nabla \overline{S}_a}_{2} - \underbrace{H\overline{\widetilde{\mathbf{v}}_a \cdot \nabla \widetilde{S}_a}}_{3} - \underbrace{H\overline{\mathbf{v}'_a \cdot \nabla S'_a}}_{4} + \underbrace{\overline{P-E}}_{5}. \tag{3.5}$$

From left to right, the terms represent the mean salt tendency, the mean horizontal salt advection of the mean salinity gradient, the anticyclonic eddy horizontal salt advection, the horizontal salt advection from non-eddy and non-mean contributions, and the net surface precipitation minus evaporation equivalent. Again, the overbar representing the time mean is performed over different time scales in this study.

If we consider the balance of terms in equations 3.4 and 3.5 over all time, the tendency term (Term 1) must be zero as a result of heat or salt conservation. This forces the terms 2-5 to balance. Over shorter time scales (the mooring observation period, for example), the terms 2-5 are not required to balance to zero, which yields a temperature or salinity trend over that time scale. A non-zero trend implies that one or more terms are anomalous with respect to their all-time mean. We will examine this idea in section 3.8, but first, we examine the heat and salt balance terms on the 7-year time scale when mooring data are available.

3.5 Observed trends in heat and salt

Figure 3.1 shows the vertically-averaged temperature and salinity data observed by the CIS mooring for the top layer (0-460m), bottom layer (460m-1000m), and all depths (0-1000m). The top layer temperature signal shows a slight decreasing trend primarily over the latter part of the timeseries. It is small compared to the other scales of variability. The most obvious variability is the seasonal cycle, on top of which are shorter-scale fluctuations. The upper layer encompasses most of the all-layer variability, and it appears that the variability in the two layers is somewhat decoupled. We now explain the methods used to calculate the terms in the heat and salt budgets and compare their values.

3.6 7-year Heat Balance Terms

3.6.1 Term 1: Temperature Tendency

Term 1, the temperature tendency, is calculated using depth-averaged temperature measurements from the CIS mooring, interpolated onto a daily time grid. A linear

trend line is fitted to minimize the least squared error while omitting data gaps. Because the large seasonal cycle has the potential to bias the trend estimate, we isolate it using a band pass filter (4 months to 1 year) and remove it from the signal before fitting the trend. The uncertainty for the tendency term comes from the error on the linear fit. The values of the terms in the 7-year heat budget are shown in table 3.1. Term 1, the mean temperature tendency, is -5.09$\pm$4.61x10^{-7} $^oCm/s$ at 90% significance. This corresponds to a 0.24^oC decrease over 7 years. The fitted trend is negative (non-zero) with 93% confidence.

3.6.2 Term 2: Advection of Mean Temperature Gradient by Mean Current

Term 2 represents the advection of the mean temperature gradient by the mean current. Again, the time average is performed over different time scales in this analysis to examine the size of this term at these scales. The term $\overline{\mathbf{v}}_a$ is estimated using the depth-averaged daily CIS mooring ADCP horizontal velocity data, which has an error of 0.01 m/s (Karstensen, 2005). $\nabla\overline{T}_a$ is calculated using the WOA climatology mean temperature field depth-averaged over the upper 500m. The WOA data are provided on a 1^o grid, and gradients are calculated between each successive grid point. Here, we assume that the 7-year mean fields are not too different from the climatological mean, and can be represented by the WOA product.

The value of $\nabla\overline{T}_a$ at the CIS mooring location is taken at the WOA grid point closest to the mooring. The WOA $\nabla\overline{T}_a$ field within the Irminger gyre varies from the value at the mooring location by only 15%, so the choice of location to evaluate this term is not crucial in determining an estimate as long as it remains within the gyre limits. The variability of this term within the gyre gives a estimate for its uncertainty. The uncertainty of the 7-year mean $\mathbf{v}_a$ is very small, so the uncertainty for $H\overline{\mathbf{v}}_a \cdot \nabla\overline{T}_a$ is 15%. The value of this term over the 7-year period is -0.04$\pm$0.006^{-7} $^oCm/s$ (shown in table 3.1). This term is about 3 orders of magnitude smaller than the magnitude of Term 1.

The gridded WOA product does not capture scales of local gradients smaller than the decorrelation scales used in their mapping. Thus, we are omitting a component of

variability and may be under-estimating $H\overline{\mathbf{v}}_a \cdot \nabla\overline{T}_a$. The frequency-wavenumber spectrum of the horizontal temperature field would give the amount of variance contained in scales smaller than 1^o over 7-year periods. We do not have the necessary information to estimate this spectrum, but we can put an upper bound to $H\overline{\mathbf{v}}_a \cdot \nabla\overline{T}_a$ if we were to include variance at eddy-sized scales. The anticyclones we observe have warm cores, and the largest values of $\nabla\overline{T}_a$ are found between the core and periphery. A typical temperature gradient is on the order of 0.3^oC/10km. If this gradient were to persist at the mooring location over 7 years, the estimate of $H\overline{\mathbf{v}}_a \cdot \nabla\overline{T}_a$ would be 0.17x10^{-7} $^oCm/s$. In reality, the steady gradient would not persist, and actual values would be lower. This upper bound estimate is still one order of magnitude smaller than Term 1. Term 2 is largely controlled by the velocity measurements, which become very small in the 7-year mean. Therefore, the upper bound of Term 2 with smaller-scale gradients does not change the fact that Term 2 is small compared to Term 1, and is negligible in the heat balance.

3.6.3 Term 3: Anticyclonic Eddy Heat Component

We use this term to represent the net input of heat by warm anticyclones if they formed at the boundary current and were dissipated inside the gyre interior. The estimate is based on the assumption that each year, the interior eddy field is mixed into the Irminger basin. Supporting this idea is the lack of antciyclones during each winter of the mooring timeseries (see Fan et al., 2013). It is possible that the winter mixing process causes the anticyclones to decay and leave their core water inside the gyre; this particular process is explored in detail in Chapter 4.

Here, we use four different methods to estimate the eddy term. In all methods, we estimate the ratio of total eddy area to the CIS basin area, called p. Assuming that each year, the eddy volume replaces the same volume of CIS non-eddy water, we can estimate an effective heat flux by the eddies as follows:

$$-\overline{H\widetilde{\mathbf{v}}_a \cdot \nabla\widetilde{T}_a} = \frac{pH(T_{eddy} - T_{cis})}{T}. \tag{3.6}$$

T_{eddy} and T_{cis} are the mean depth-averaged anticyclone and CIS non-eddy temperatures from each year, obtained from Fan et al. (2013), and T the time scale of interest. In this

formulation, we always have a positive input of heat from the eddies because T_{eddy} is always greater than T_{cis} in the observations.

The first and second methods both estimate p using satellite altimetry from the gridded AVISO sea level anomaly (SLA). The yearly mean p is calculated from weekly snapshots of SLA; it represents the ratio of area covered by anticyclones having a positive SLA greater than 8cm (the threshold used in Fan et al. (2013) to identify anticyclones in SLA). This method is likely a low estimate because the resolution of altimetry is unable to resolve the small anticyclones observed at the CIS mooring site. Furthermore, the SLA is calculated with respect to the 1992-2005 mean sea surface, so some anticyclones may be missed because their SLA is not anomalously positive compared to that period. Thus, the satellite altimetry method is likely a low estimate for p. The mean p over the 7-year period estimated from this method is 0.05 (5% eddy coverage). The second method uses the results of the Chelton algorithm, which is described in Chelton et al. (2007) and is based on the AVISO gridded product. The Chelton product provides detected eddy tracks and their apparent horizontal size. Eddies detected in the CIS basin are binned into one-week snapshots, and their total coverage is used to calculate yearly p. The 7-year mean p from the Chelton product is 0.12.

The third and fourth methods use the CIS mooring to estimate p. We assume here that the ratio of eddy area covered is equal to the ratio of time that the eddies covered in the mooring data. The third method estimates p by finding the time occupied by the eddy cores (determined from Fan et al. (2013)) in a given year. From this method, the 7-year mean p is 0.09. Because the temperature (and salinity) anomaly was often 2-3 times the horizontal extent of the eddy core, the fourth method estimates p using eddy salinities instead of eddy core information. The time during which the salinity exceeds one standard deviation from the mean is used to estimate p each year. This thresholding method was used to detect the anticyclones in Fan et al. (2013). We estimate the 7-year mean p at 0.19 by this method. The p values produce 7-year mean Term 3 estimates of $3\text{x}10^{-7}\ ^{o}Cm/s$ (altimetry method), $8\text{x}10^{-7}\ ^{o}Cm/s$ (Chelton method), $6\text{x}10^{-7}\ ^{o}Cm/s$ (mooring time method), and $13\text{x}10^{-7}\ ^{o}Cm/s$ (mooring salinity method). The mean of these values is $8\text{x}10^{-7}\ ^{o}Cm/s$, which is on the same order as Term 1 (see table 3.1). The uncertainty, represented by the differences between the four methods, is $5\text{x}10^{-7}\ ^{o}Cm/s$.

It is important to note that the value of this term represents only the anticyclonic eddy component and does not take into account transports from other features of the same scale, such as cyclonic eddies.

3.6.4 Term 4: Non-eddy Horizontal Heat Advection

From the available data, it is difficult to estimate all the processes this term represents. However, we can estimate a magnitude for $\nabla T_a'$ representing the contributions from timescales longer than one month using the monthly gridded temperature fields from the Roemmich and Gilson (2009) study and the Hosoda et al. (2008) study (referred to as RG2009 and H2008, respectively). These studies provide monthly temperature fields on a 1^o grid. Due to the coarse temporal and spatial resolution of these products compared to eddy time and length scales (order 1-2 weeks and 10 km), these gridded $\nabla T_a'$ fields are not expected to capture the eddy-scale variability, and therefore represent time and space scales of fluctuations not related to the eddies. Because the variation of the monthly temperature gradient within the Irminger gyre obtained from these products is large, we estimate decorrelation scales of velocity and temperature to determine an area around the mooring location over which to average the gradient. This is meant to represent the local gradient at the mooring location. Using velocity measurements from surface drifters (described in Chapter 1) and Argo float trajectories, zonal and meridional velocity decorrelation scales ranged between 120 and 180km at the surface, and 110 to 150km at 1000m depth. Because velocity decorrelation scales are similar at these two depths, we assume that the decorrelation scale in the upper 460m layer is similar. The zonal and meridional decorrelation scale in the 0-460m depth-averaged temperature field from both Argo gridded products ranged between 230 and 250km. The temperature decorrelation scale is almost twice that of the velocity decorrelation, so we use the velocity decorrelation scale to determine the size of grid box over which to average. On the 1^o grid of the Argo products, a 120-180km scale corresponds to averaging over 2 to 3 grid points.

The values of Term 4 using a temperature gradient averaged over 2 by 2, 3 by 3, and 3 by 2 grid points around the mooring location are 12.75, 15.87, and 18.81x10^{-7} $^oCm/s$ (RG2009), respectively , and 3.88, 4.15, and 3.93x10^{-7} $^oCm/s$ (H2008). The

range of these values, their mean, and their variability representing the uncertainty is shown in table 3.1. The range of this term is similar to the range of Term 3, the eddy contribution. According to Roemmich and Gilson (2009), the mapped properties and their associated mapping errors are sensitive to the choice of covariance function used in the mapping. It is therefore difficult to know the errors of temperature and salinity gradients derived from these products. This is the reason for presenting Term 4 as a range spanning the two products.

As with the WOA product used to calculate Term 2, the 1^o grid spacing of the Argo monthly products cannot resolve the variability of the temperature field at smaller scales, and the estimate of Term 4 may be missing a component of advection by smaller-scale gradients. However, local temperature gradients calculated from the monthly Argo grids are comparable in magnitude to the typical temperature gradient of an anticyclone. This means that monthly gridded gradient fields capture the magnitude of some of the largest gradients in the area. The Argo monthly fields likely do not capture the time variability at the smaller scales, so it is difficult to estimate how much this would affect the value of this term averaged over 7 years. Ideally, we would need to know the frequency-wavenumber spectrum to obtain the amount of variance present at scales not resolved by the Argo monthly products.

3.6.5 Term 5: Surface Heat Flux

The heat flux is the sum of the latent heat flux, sensible heat flux, longwave, and shortwave radiative heat flux. It is provided by the NCEP and ECMWF reanalyses as a daily product. In the case of the NCEP product, we use the recalculated surface sensible and latent heat fluxes (described in section 3.3 and the appendix). We do not perform a recalculation for the ECMWF heat flux because the recalculation procedure only uses knowledge of the NCEP heat flux biases in the area. The same seasonal cycle removal is performed as was done to calculate Term 1. The uncertainty of Term 5 is the standard error of the mean over the period of interest. The NCEP product yields a mean Term 5 at -18.2$\pm$4.02x10^{-7} $^oCm/s$. The equivalent calculation from the ECMWF heat fluxes gives a Term 5 of +35.1$\pm$4.90x10^{-7} $^oCm/s$. The NCEP value gives a net heat loss which is expected for this region. Because the ECMWF heat flux is positive, there

is likely a large positive bias, and we do not report this value in table 3.1. The ability for the NCEP and ECMWF heat flux products to cause realistic mixed layer properties is examined in detail in section 3.11.

3.6.6 Dominant Terms in the 7-year Heat Balance

The largest contribution to the observed temperature change is from the NCEP surface forcing. The eddy contribution is smaller but of similar magnitude, so the eddy component cannot be neglected in the balance. The advection of the mean temperature field by the mean current is 2-3 orders of magnitude smaller than the other terms, and appears to play a negligible role in the heat balance on the 7-year time scale. This is expected, because the CIS mooring was placed near the center of the gyre, where velocities are expected to be low compared to other regions where the change in dynamic topography would be more prominent. The range of 7-year mean values of terms 3 and 4 show similar magnitudes. Although Term 4 is a rough estimate of non-eddy processes, there is the possibility that it is as large as the eddy term.

Over the 7-year time scale, the expected heat loss due to surface fluxes (Term 5) is much larger than the temperature decrease observed. Within the range and uncertainty of the eddy term (Term 3), the eddy component can replenish enough heat to explain the observed temperature decrease. Term 4, the non-eddy term, likely plays some role in the heat balance at these scales. Regardless of the size of Term 4, the eddy contribution to the heat balance remains an important factor in explaining the temperature variability on the 7-year time scale.

3.7 7-year Salt balance terms

We calculate the salt balance terms in (3.5) in the same way as the heat balance terms described in the previous section, but replace temperature with salinity from the same datasets for each term. Values for the salt balance terms are summarized in table 3.2.

3.7.1 Term 1: Salinity Tendency

Term 1 in (3.5) is estimated using a fitted trend to the mooring depth-averaged salinity data with seasonal variability removed. See section 3.6.1 for calculation details. The value of Term 1 is $1.096 \pm 1.029 \text{x} 10^{-10}$ $kg/kg\ m/s$ at 85% significance. This corresponds to the mean increase in salinity of 0.053 g/kg over the 7-year timeseries, visible in the bottom panel of figure 3.1. The fitted trend is positive (non-zero) at 86% confidence.

3.7.2 Term 2: Advection of Mean Salinity Gradient by Mean Current

Details for this calculation are in section 3.6.2. The $\nabla \overline{S}_a$ field (Term 2 of equation (3.5) is calculated from the WOA product. We use the value at the WOA grid point closest to the mooring location. The variability of the 7-year mean $\nabla \overline{S}_a$ within the central gyre is 20%, which represents the uncertainty of this estimate. This gives an uncertainty of 20% to the value of $-H\overline{\mathbf{v}}_a \cdot \nabla \overline{S}_a$. Its value over the 7-year mean is $2.56 \pm 0.435 \text{x} 10^{-14}$ $kg/kg\ m/s$. This term is 3 orders of magnitude smaller than Term 1.

3.7.3 Term 3: Anticyclonic Eddy Salt Component

Term 3 represents the net eddy input of salt from anticyclones entering the Irminger Gyre and decaying there, as described in section 3.6.3. The eddy salt component is estimated as

$$-\overline{H\widetilde{\mathbf{v}}_a \cdot \nabla \widetilde{S}_a} = \frac{pH(S_{eddy} - S_{cis})}{T}, \tag{3.7}$$

where S_{eddy} is the mean eddy core salinity (obtained from Fan et al. (2013)), and S_{cis} is the mean non-eddy salinity. The salty anticyclone cores make $S_{eddy} > S_{cis}$, and we always have a positive anticyclone salt input. The ratio p is the same as in section 3.6.3. The values for Term 3 (shown in table 3.2) are $3.94 \text{x} 10^{-11}$ $kg/kg\ m/s$ (altimetry method), $8.77 \text{x} 10^{-11}$ kg/kg (Chelton method), $5.61 \text{x} 10^{-11}$ kg/kg (mooring time method), and $15.6 \text{x} 10^{-11}$ kg/kg (mooring salinity method), with a mean value of $8.48 \text{x} 10^{-11}$ kg/kg. The variability representing the uncertainty is $5.8 \text{x} 10^{-11}$ kg/kg. The

value of this term is the same order of magnitude as Term 1, the tendency term.

3.7.4 Term 4: Non-eddy Horizontal Salt Advection

Term 4 in (3.5) is difficult to estimate from the available data. We use the method outlined in section 3.6.4 to get an order of magnitude estimate for this term using the salinity fields provided by the RG2009 and H2008 Argo gridded monthly products. The values of Term 4 using a salinity gradient averaged over 2 by 2, 3 by 3, and 3 by 2 grid points around the mooring location are 10.51, 11.10, and 12.18e-11 $kg/kg\ m/s$ (RG2009) respectively, and 18.21, 10.93, and 19.71e-11 $kg/kg\ m/s$ (H2008). The range of these values, their mean, and their variability representing the uncertainty is shown in table 3.2. The range of this term is similar to the range of Term 3, the eddy contribution.

3.7.5 Term 5: Surface Salt (Freshwater) Flux

The surface freshwater flux is obtained from both the ECMWF and the NCEP products. The ERA-40 product only extends to the end of 2002, and the ERA-Interim run overlaps with the CIS mooring observations. We use values from the ERA-Interim product to compare with other terms in the balance, but will use the ERA-40 product in studying the variability over a longer time period in a later section. For the NCEP product, evaporation is calculated using the latent heat flux. The seasonal cycle is removed in the same way as with the tendency terms. Precipitation observations in both the ECMWF and NCEP products are not directly assimilated in the reanalyses, and these variables will inherently contain uncertainties pertaining to how well the model represents the true physics. Therefore, absolute values of the precipitation and evaporation may have large uncertainties or biases. For example, both the monthly averaged and annual mean precipitation rates provided by the ECMWF model are consistently biased high by about 0.3 mm/day globally (Dee et al., 2011).

Term 5, the net surface freshwater input (precipitation minus evaporation) from the ERA-Interim product has a mean value of 1.5606 meters of water over the 7 years of the mooring timeseries. Assuming that this freshwater replaces an equal volume of Irminger Sea water, Term 5 is estimated at -24.8x10^{-11} kg/kg. Correcting for the

mean bias of 0.3 mm/day (0.1 m/year) over 7 years yields a lower freshwater input, -12x10^{-11} kg/kg. This is of the same order of magnitude as Terms 1, 3, and 4. The NCEP reanalysis reports a mean value of 5.1 meters over 7 years, yielding a Term 5 of -81.044x10^{-11} kg/kg. This NCEP value is likely biased very high compared to the other terms. We report the reanalysis freshwater terms in table 3.2, but it should be noted that their uncertainties are large, likely the same order of magnitude as the signal itself. The uncertainties of the surface forcing terms are discussed in detail in section 3.11. Although the magnitude of the freshwater signal is questionable, we will use information from the interannual *variability* of the freshwater reanalysis terms, which we discuss in the next section.

3.7.6 Dominant Terms in the 7-year Salt Balance

As in the case for the heat balance, the salt advection term is about 3 orders of magnitude smaller than the other terms and is therefore negligible in the 7-year salt balance. It is difficult to gauge how well the surface and eddy terms balance to create the positive salt tendency term because their uncertainties are so large. Later in this study (section 3.11, we determine that the NCEP product likely over-estimates the net freshwater input by an order of magnitude, and this term is better represented by the ECMWF (ERA) product. If we take the ERA-Interim surface term at face value, the eddy and surface terms could produce the salt tendency term and likely both play important roles in the balance over the 7-year period. As with the case for heat, there remains the chance that Term 4, the non-eddy horizontal salt advection, can play a role in the salt balance over the mooring period. Term 4 can be the same size as the eddy term, but this does not discount the conclusion that the eddy and surface terms are important in the salt balance.

3.8 Long-term balances compared to the 7-year timescale

3.8.1 Long-term Heat Balance

Over all time, heat is conserved, and we have a temperature balance equation with zero tendency:

$$\underbrace{0}_{1} = \underbrace{-H\overline{\mathbf{v}}_a \cdot \nabla \overline{T}_a}_{2} - \underbrace{H\overline{\widetilde{\mathbf{v}}_a \cdot \nabla \widetilde{T}_a}}_{3} - \underbrace{H\overline{\mathbf{v}'_a \cdot \nabla T'_a}}_{4} + \underbrace{\frac{\overline{Q_{net}}}{\rho_o c_p}}_{5}. \tag{3.8}$$

Over the 7-year mooring timeseries, Term 1 in (3.4) is negative. This means that one or more of Terms 2-5 is out of balance over this period compared to their values over all time. In this section, we examine which terms are out of balance during the mooring period.

Immediately, Term 2 can be ruled out because we have shown that it is negligibly small compared to the other terms. Term 3, the eddy term, would cause a decrease in temperatures if anticyclone numbers decreased over the 7-year period, or if the anticyclone core temperatures decreased. The eddy counts presented in Fan et al. (2013) show year-to-year variability over the mooring timeseries, but no visible trend in numbers or eddy sizes. As for eddy core temperatures, an increase is observed (see Fan et al., 2013), so this cannot explain the temperature decrease. It is thus unlikely that the eddy term is causing the imbalance. Changes in Term 4 are difficult to estimate with the available data.

It has been widely recognized that the sea surface temperature, largely governed by the surface heat flux, is related to the North Atlantic Oscillation (NAO) index (e.g. Bjerknes, 1964; Rodwell et al., 1999). The NAO has been recorded on a daily basis since the 1860s and provides a dataset much longer than our mooring timeseries. We will use the 150-year time period covered by the NAO for long-term comparison to the surface heat fluxes during the mooring period. Although this period does not represent 'all time', it describes a time scale much longer than our mooring period. Figure 3.2 shows the timeseries for the NCEP net surface heat flux (with heat loss from the ocean being positive) and the scaled NAO index. Both timeseries show the annual average

value (from January to January) and their 10-year running mean (thick line). The NAO index is scaled such that the yearly variability has the same standard deviation as that of the NCEP surface fluxes. The yearly values show correlated peaks and troughs, and the 10-year running means show similar multi-year variability. The correlation function between the two overlapping signals (plotted in the bottom panels of figure 3.2) shows a significant correlation at zero time lag of 0.8, meaning the two timeseries are well correlated. Other significant (positive and negative) correlations exist at $\pm$ 20 and 40 years, which is a reflection of the peak-to-trough time scale in the NCEP surface heat flux variability.

Because the NCEP surface heat flux and the NAO index are well correlated at zero lag, we can use the NAO index to estimate how different the surface heat forcing is during the mooring timeseries compared to a longer term mean. The NAO index mean over the 2002-2009 period is slightly positive. From this, we infer that the ocean surface heat loss is greater over the mooring time period than the long-term mean since the 1860s. The amount of offset during the mooring time period yields a difference of 8x10^{-7} $^{o}Cm/s$ for the surface heat flux term. Over the 150-year period, the net heat flux would then be -10x10^{-7} $^{o}Cm/s$, a value that can balance with the eddy term to produce a zero tendency, if the eddy term is held constant over this longer period. Thus, we have shown that the surface heat loss during the mooring period is likely anomalously high, and can entirely explain the observed temperature decrease. However, we cannot determine if Term 4 is anomalous over the mooring period, and it may have some effect on the temperature trend. Although the temperature trend cannot be explained by a change in the eddy heat transport, the eddy component remains an important term that sets up the heat balance over 7 years and longer time periods.

3.8.2 Long-term Salt Balance

As with the heat balance, the conservation of salt requires that the salt tendency is zero over all time:

$$\underbrace{0}_{1} = \underbrace{-H\overline{\mathbf{v}}_a \cdot \nabla \overline{S}_a}_{2} - \underbrace{H\overline{\widetilde{\mathbf{v}}_a \cdot \nabla \widetilde{S}_a}}_{3} - \underbrace{H\overline{\mathbf{v}'_a \cdot \nabla S'_a}}_{4} + \underbrace{\overline{P-E}}_{5}. \tag{3.9}$$

Over the 7-year time scale, Term 1 is positive, meaning that one or more of terms 2-5 is out of balance over this period compared to their values over all time. We will identify which terms in (3.9) are out of balance over the mooring period.

As with the case of long-term heat balance, Term 2, the salt advection term, cannot cause the imbalance because its magnitude is negligible compared to other terms. The eddy component (Term 3) can produce a salinity increase in the basin if the number of eddies increases or if eddy core salinities increase. As mentioned in the previous section, the numbers of anticyclones does not appear to change in a significant way. Regarding eddy core salinities, it is shown in Fan et al. (2013) that there is indeed an increase in core salinities over the mooring period. Assuming the eddies form from Irminger Current water, typical changes in Irminger Current salinity can be used to estimate the corresponding change in Term 3. Våge et al. (2011b) report an Irminger Current salinity increase of about 0.1 psu over 10 years (from 1990s to 2000s). We use the average number and size of eddies reported in Fan et al. (2013) to estimate the corresponding change in Term 3. With a constant CIS non-eddy salinity of 34.88, we expect the total salt content to increase by $7.9\text{x}10^{5}$ kg over 7 years in the CIS basin. This translates to a $7.8\text{x}10^{-17}$ kg/kg change in Term 3. This change is negligible compared to the size of the salt tendency term, so typical changes in the eddy core properties do not change the salt balance enough to explain the observed salt tendency.

The changes in Term 4, the non-eddy salt advection term, are difficult to estimate with the available data, so the possibility remains that this term can have some effect on the imbalance of (3.9). Finally, Term 5, the surface freshwater flux, is compared to the NAO index like the comparison done with the surface heat flux in the previous section. Figure 3.3 shows the timeseries of daily P-E anomaly for the ERA-40, ERA-Interim, and NCEP products as well as the timeseries of annual average NAO index. The NAO index is scaled such that its standard deviation is the same as that of the ERA-40 product. The three P-E signals are rescaled to have the same standard deviation in the bottom panel of figure 3.3 so their variabilities can be compared. None of the P-E curves show a significant correlation with the NAO at zero lag. However, all three P-E anomaly curves show a negative anomaly during (or close to) the mooring time period, 2002-2009. This implies less freshwater input than previous years. Less precipitation during the mooring

observations is supported by Dickson et al. (2002), who correlate small magnitude cold-season mean NAO with less storm activity over the North Atlantic (and hence, less precipitation) during this time. These results imply that over much longer time periods, there is more freshwater input compared to the mooring period. This can explain the salinity increase observed by the mooring. Although magnitudes of the imbalance are difficult to estimate given the large uncertainties of Term 5, there is evidence that this term can cause the observed salinity increase during the mooring period. We cannot discount the effect of Term 4 on the imbalance, and it is possible that both Terms 4 and 5 are responsible for the salt tendency.

3.9 Yearly heat balance

The yearly terms in equation 3.4 are calculated similarly to the 7-year means, but averages are performed over January-January periods each year. The only difference is in the calculation of the horizontal temperature and salinity gradients used in Term 2. WOA climatology does not have year-to-year variability information, so we use the monthly gridded Argo float products instead. The horizontal gradients are calculated at every depth level at each monthly snapshot, and the depth-average gradients each year are calculated at the grid point closest to the mooring. Although we had used decorrelation scales in the calculation of Term 4 on 7-year time scales, we use the gradient value at the closest grid point to the mooring for the yearly balance because averaging over one year smooths the monthly variability in gradients around the mooring. As mentioned in section 3.6.4, the mapped properties and their associated mapping errors are sensitive to the choice of covariance function used in the mapping. It is therefore difficult to know the errors of temperature and salinity gradients derived from these products. Here, we show the range of values each term exhibits in order to compare magnitudes of variability.

The range of values of the heat budget terms are summarized in table 3.3. From year to year, the temperature tendency term is quite variable, ranging from -170 to 120x10^{-7} $^{\circ}Cm/s$. This yearly variability is one order of magnitude larger than the tendency over the 7-year mean (section 3.6). Compared to the yearly Term 1, Terms 2

and 5 exhibit comparable ranges of variability, while the anticyclonic eddy term shows the smallest values. This suggests that on the yearly timescale, the eddy input of heat is small compared to the advection and surface terms and likely plays a small role in the balance. The yearly anticyclonic eddy term is of the same order of magnitude as its value for the 7-year mean (section 3.6), but the other terms in the budget have much higher yearly values. As mentioned earlier, the horizontal advection terms have large uncertainties associated with them, but it is reassuring that similar ranges of variability are exhibited by both products. The dominant terms on the yearly time scale appear to be the mean advection, non-eddy advection, and surface flux. This is contrasted with the 7-year (and presumably longer) time scale where the importance of the mean horizontal heat advection diminishes, while the anticyclonic eddy heat contribution becomes important to balance with the surface heat fluxes.

3.10 Yearly salt balance

The yearly salt balance is estimated in the same way as the yearly heat balance. The variability of the salt budget terms is summarized in table 3.4. We again use the two Argo products to estimate horizontal gradients, and the two reanalysis products for surface freshwater flux. Term 2 estimated from the two Argo products yields similar magnitudes of ranges. The surface P-E from the ERA-Interim products shows a range that is much smaller than the NCEP-derived estimates, so the uncertainty of the surface flux estimate is large. Although we cannot close the budget, we can see that the anticyclonic eddy term variability is of similar magnitude to its mean value over the 7-year mean (section 3.7), but the range of yearly values for the other salt budget terms all increase by one order of magnitude, thus making the anticyclonic eddy contribution small on yearly timescales. This suggests that, like the case of yearly heat balances, the anticyclonic eddy salt component is not an important term for the salt budget over each year. This is contrasted with the 7-year case where the anticyclonic eddy term becomes an important term in the budget.

3.11 Regarding the uncertainty of the NCEP and ECMWF surface fluxes

We have shown that both the surface heat and salt flux terms are vital to the heat and salt balance, but their large uncertainties make it difficult to compare to actual data. Because actual observations of surface heat flux, precipitation, and evaporation are sparse at the mooring location, we use a simple 1D mixing model to examine whether the NCEP heat and salt fluxes can reproduce observed mixed layer depths and properties from the CIS mooring. This mixing model follows closely the 1D mixing model outlined by De Jong (2010), and equations for the mixing model are found in that text. Mooring temperature and salinity profiles are taken at the beginning of each year's winter cooling (from NCEP), and a new surface wind-mixed layer temperature and salinity are calculated at each time step throughout the cooling period. A simple stability criterion is evaluated at each step: if the surface layer is more dense than the layer immediately below, vertical mixing of properties occurs. This mixing is done in depth steps of 5m (although results at smaller steps are similar) until the surface mixed layer is statically stable. The initial wind-mixed layer depth is taken at 70 m at each new time step, the same as the one used in De Jong (2010) and reflects the observations of Ekman layer depth in the region (Våge et al., 2008a).

Mixed layer properties resulting from three scenarios are plotted in figure 3.4: 1) using the NCEP heat flux (no re-calculation) and zero freshwater flux, 2) using the re-calculated NCEP heat flux and zero freshwater flux, and 3) using the re-calculated NCEP heat flux and NCEP precipitation minus evaporation. Between scenarios 1) and 2), we observe the best correspondence between modeled and actual mixed layers, temperature, and salinity while using the corrected NCEP heat flux with zero freshwater flux. Compared to this, using the uncorrected NCEP heat flux values consistently gives a low bias in mixed layer temperature. This bias was the original reason for the heat flux correction (explained in the appendix), and gives some assurance that the correction brings the NCEP heat fluxes to more realistic values.

On yearly time scales, the mixed layer properties resulting from re-calculated NCEP heat fluxes do still have some mis-match with the observations. We have shown

in table 3.3 that on yearly time scales, Term 3, the eddy term, is small, so the other horizontal advection terms (Terms 2 and 4) must be responsible for the remaining mismatch of properties on yearly scales. On 7-year time scales, we have shown in table 3.1 that the eddy term is large, and offsets a large part of the surface heat flux. This effect is not obvious in figure 3.4 because the 7-year mean heat flux represents the residual heat flux after smoothing over shorter time scales (i.e. yearly). Although not shown, the same experiment is performed using the ECMWF heat fluxes. Recalling the large positive value of the ECMWF 7-year mean heat flux (see section 3.6.5), this large positive bias is reflected in mixed layer depths that are much too shallow each year compared to observations, and mixed layer temperatures that are much too warm at the end of each mixing season. This reinforces the fact that the ECMWF heat flux has a large positive bias over the mooring period and on yearly time scales.

Comparing scenarios 2) and 3), using the corrected NCEP heat flux and freshwater fluxes together produces mixed layers that are consistently too shallow compared to the observations. Correspondingly, the mixed layer salinities in the model are much lower compared to the observations, suggesting that the NCEP freshwater fluxes are largely overestimated. This over-estimation is reflected in the very large values of Term 5 in the salt balance (see table 3.2). If we believe that the salt transport due to the anticyclones balances the surface freshwater input over the 7-years, we can run the mixing model using the value for Term 3 in table 3.2. Assuming this rate of freshwater input over every winter, the mixed layer properties are very similar to observations. This suggests that the balance between surface and eddy salt flux can give realistic mixed layer properties. If the surface term were to balance Term 3, the 7-year mean P-E value would be one order of magnitude smaller than what the NCEP product currently reports (table 3.2). The NCEP product is overestimating the surface freshwater flux by an order of magnitude at this location. The ECMWF surface freshwater flux produces a much more realistic Term 5 and is comparable in magnitude to Term 3 (shown in table 3.2 with a global bias correction). However, because the ECMWF heat fluxes were largely over-estimated, it is difficult to evaluate the ECMWF suite as a whole.

3.12 Vertical fluxes

So far, we have ignored the vertical flux of heat and salt through the bottom of our layer in the budget calculations. We can estimate the vertical flux using the salinity signal. From the mooring observations, the upper 460 m layer is always more salty than at greater depths, so we assume that increases in the 460-1000 m layer salinity are entirely attributed to vertical exchange from the upper layer. This gives an estimate of an upper limit of the magnitude of vertical fluxes, ignoring horizontal fluxes. We define an upper and lower layer salinity, $S1i$ and $S2i$, respectively, at a starting time step i. We calculate the depth D equivalent of $S1i$ water that must have mixed into $S2i$ in order to produce the salinity of the lower layer at the next time step, $S2f$:

$$D = \frac{S2f - S2i}{S1i - S2i} H2. \tag{3.10}$$

Here, $H2$ is the constant lower layer thickness. This calculation is done using daily salinity measurements from the CIS mooring, and the resulting D is shown in figure 3.5. There appears to be no significant difference between winter periods (during convection) and summer non-convecting periods, suggesting that vertical fluxes may not be larger than usual during deep convection events as we had suspected.

Converting the depth D to the same units as the the salt balance terms in equation 3.5 results in a mean salt contribution of 1.6x10^{-12} $kg/kg\ m/s$ over the mooring time period. This value is one order of magnitude smaller than the tendency, eddy, and surface salt balance terms over 7 years, justifying our neglecting it in our equations.

The temperature balance term is estimated by assuming that the salt flux (SF) can be explained by a vertical velocity advecting the vertical salt gradient.

$$SF = H_o \overline{w} \overline{\frac{\partial S}{\partial z}} \tag{3.11}$$

Here, we estimate the vertical velocity w by calculating the vertical salinity gradient $\partial S/\partial z$ between $S1$ and $S2$ over the distance between the mid-point of the two layers, H_o. This gives a vertical velocity of -7.3x10^{-8} m/s. Using the two layer average temperatures, we calculate the vertical temperature gradient. Using the vertical velocity and the vertical temperature gradient, we arrive at a vertical temperature flux estimate.

Converted to the same units as in equation 3.4, we obtain a mean vertical temperature term of 7.8x10^{-8} $^{o}C\ m/s$ over the mooring period. This value is one order of magnitude smaller than the heat tendency, eddy, and surface flux terms, and thus justifies our neglecting it in the budget for both heat and salt.

3.13 Conclusions and Discussion

The heat and salt budget terms were examined over a 7-year mooring period as well as on yearly time scales. Anticyclonic eddy statistics from Fan et al. (2013) are used to quantify the eddy heat and salt input over these periods. For the case of both heat and salt, the tendency term can be explained by the eddy and surface flux terms, which are the dominant terms in the 7-year balance. The value of the non-eddy non-mean advection term can be as large as the eddy term. The observed temperature decrease of the ISW layer between 2002 and 2009 can be attributed to more heat loss to the atmosphere compared to longer time scales. The decrease in temperature was likely not caused by the dynamics of the anticyclonic eddies. The observed salinity increase was also attributed to the change in surface fluxes, and not to a change in eddy input of salt. Over the mooring time period, the surface freshwater input appears to be weaker than over longer time scales, causing the ISW layer salinity to increase. Evidence from Dickson et al. (2002) supports less freshwater input during the mooring measurements, attributed to a small NAO index which corresponds to less storms over the region. Over this period, it is difficult to estimate whether the non-eddy horizontal advection (Term 4) plays a role creating the observed temperature decrease and salinity increase.

On yearly time scales, the anticyclone component of the heat and salt balance becomes small compared to the other terms, and it appears that the dominant terms are the horizontal advection (mean and possibly non-eddy non-mean) and the surface fluxes. The anticyclonic eddy term transitions from being dominant to small between the 7-year and one-year time scales in the CIS basin. This suggests that anticyclones are important to the ISW interannual variability. Despite not having caused the heat or salt changes observed over the 7-year period, a steady input of heat and salt from the anticyclones sets up the balance over the long term.

Previous studies have shown that in the neighboring Labrador Sea (see figure 2.1), 'Irminger Current Anticyclones' are responsible for between 25 and 100% of the heat needed to balance the surface heat loss during winter convection (Lilly et al., 2003; Katsman et al., 2004; Hátún et al., 2007; Rykova et al., 2009) and can be an important contributor to the salt (or freshwater) budget (Hátún et al., 2007; Schmidt and Send, 2007). In the Norwegian Sea, anticyclones observed in the Lofoten Basin (see figure 2.1) have been shown to be essential in maintaining the heat balance (Nilsen and Falck, 2006; Köhl, 2007; Rossby et al., 2009a). The anticyclones observed in the CIS basin are very similar to the ones found in the Labrador Sea and Lofoten basins in that they are all formed from boundary current water and thus provide an input of heat and salt to the basins. Although the CIS anticyclones do not appear to be responsible for year-to-year variability, over the 7-year mooring time period (and presumably longer), the anticyclones are an essential component to setting up the heat and salt balance with surface forcing.

The NCEP and ECMWF products were used to estimate surface fluxes. Using a simple 1D vertical mixing model, we were able to show that the recalculated NCEP heat flux alone (with no freshwater input) results in realistic mixed layer depths, temperature, and salinity properties. The ECMWF heat flux (no recalculation applied) shows a large positive bias which results in the production of mixed layers that are too shallow and warm each winter. Incorporating the NCEP surface freshwater fluxes into the mixing model yielded mixed layers that were much less saline and depths much too shallow compared to observations each year. For the NCEP net freshwater flux to reflect observed mixed layer properties, the value of this term would need to be at least one order of magnitude smaller than what the product reports. If the surface freshwater flux were to balance the eddy input of salt over 7 years, the 7-year mean freshwater flux from NCEP would likewise need to be about 10 times smaller. The 7-year mean ECMWF freshwater flux shows a value in the proper range to balance the eddy salt transport and drive realistic mixed layer properties. Over yearly time scales, the ECMWF product appears to obtain realistic net freshwater flux values, but has a large positive bias in heat fluxes. In contrast, the recalculated NCEP product provides realistic values for heat fluxes, but the net freshwater flux is overestimated by an order of magnitude.

Chapter 3 would have not been possible without the work of the co-authors, Uwe Send and Johannes Karstensen. Funding for the CIS mooring was provided by the European Ocean Observatory Network (EuroSITES). Altimeter data was provided via the AVISO website (*www.aviso.oceanobs.com*). Argo data was provided by the USGADAE Project website ($http://www.usgodae.org$). Argo gridded fields were provided by the UCSD Argo website ($http://www.argo.ucsd.edu/Gridded_fields.html$). NCEP Reanalysis Derived data was provided by the NOAA/OAR/ESRL PSD, Boulder, Colorado, USA, from their website ($http://www.esrl.noaa.gov/psd/$). The ECMWF Reanalysis data was provided by the European Centre for Medium-Range Weather Forecasts, 2009: ERA-Interim Project, available online at $http://rda.ucar.edu/datasets/ds627.0/$. The World Ocean Atlas (WOA) climatology datasets were provided by the NOAA National Oceanographic Data Center (NODC) and are available at $http://www.nodc.noaa.gov/OC5/WOA09/pubwoa09.html$.

Table 3.1: Summary of heat balance term values and their uncertainties for 7-year average time period.

Term	Value (in $10^{-7}\ ^{o}C\ m/s$)	Uncertainty (in $10^{-7}\ ^{o}C\ m/s$)
$H\overline{\frac{\partial T_a}{\partial t}}$	-5.1	4.6
$-H\overline{\mathbf{v}}_a \cdot \nabla \overline{T}_a$	-0.04	0.006
$-H\overline{\widetilde{\mathbf{v}}_a \cdot \nabla \widetilde{T}_a}$	3-13 (mean 8)	5
$H\overline{\mathbf{v}'_a \cdot \nabla T'_a}$	4-19 (mean 10)	7
$\overline{\frac{Q_{net}}{\rho_o c_p}}$	-18	4.0

Table 3.2: Summary of salt balance term values and their uncertainties for 7-year average time period.

Term	Value (in $10^{-11}\ kg/kg\ m/s$)	Uncertainty (in $10^{-11}\ kg/kg\ m/s$)
$H\overline{\frac{\partial S_a}{\partial t}}$	11	10
$-H\overline{\mathbf{v}}_a \cdot \nabla \overline{S}_a$	0.003	0.0004
$-H\overline{\widetilde{\mathbf{v}}_a \cdot \nabla \widetilde{S}_a}$	4-16 (mean 8.5)	6
$-H\overline{\mathbf{v}'_a \cdot \nabla S'_a}$	11-20 (mean 14)	4
$P-E\ \ (ERA-INT)$	-12	$O(10)$
$P-E\ \ (NCEP)$	-81	$O(10-100)$

Table 3.3: Summary of ranges of yearly-averaged heat budget terms.

Term	Range of Values (in 10^{-7} $^oC\ m/s$)
$H\overline{\frac{\partial T_a}{\partial t}}$	-170 to 120
$-H\overline{\mathbf{v}}_a \cdot \nabla \overline{T}_a$ (RG2009)	-20 to 40
$-H\overline{\mathbf{v}}_a \cdot \nabla \overline{T}_a$ (H2008)	-90 to 130
$-H\overline{\widetilde{\mathbf{v}}_a \cdot \nabla \widetilde{T}_a}$	2 to 5
$\frac{\overline{Q}}{\rho c_p}$	-50 to 10

Table 3.4: Summary of ranges of yearly-averaged salt budget terms.

Term	Range of Values (in 10^{-11} $kg/kg\ m/s$)
$H\overline{\frac{\partial S_a}{\partial t}}$	-210 to 110
$-H\overline{\mathbf{v}}_a \cdot \nabla \overline{S}_a$ (RG2009)	-80 to 120
$-H\overline{\mathbf{v}}_a \cdot \nabla \overline{S}_a$ (H2008)	-130 to 140
$-H\overline{\widetilde{\mathbf{v}}_a \cdot \nabla \widetilde{S}_a}$	6 to 10
$P-E$ (ERA Interim)	-30 to -20
$P-E$ (NCEP)	-140 to -90

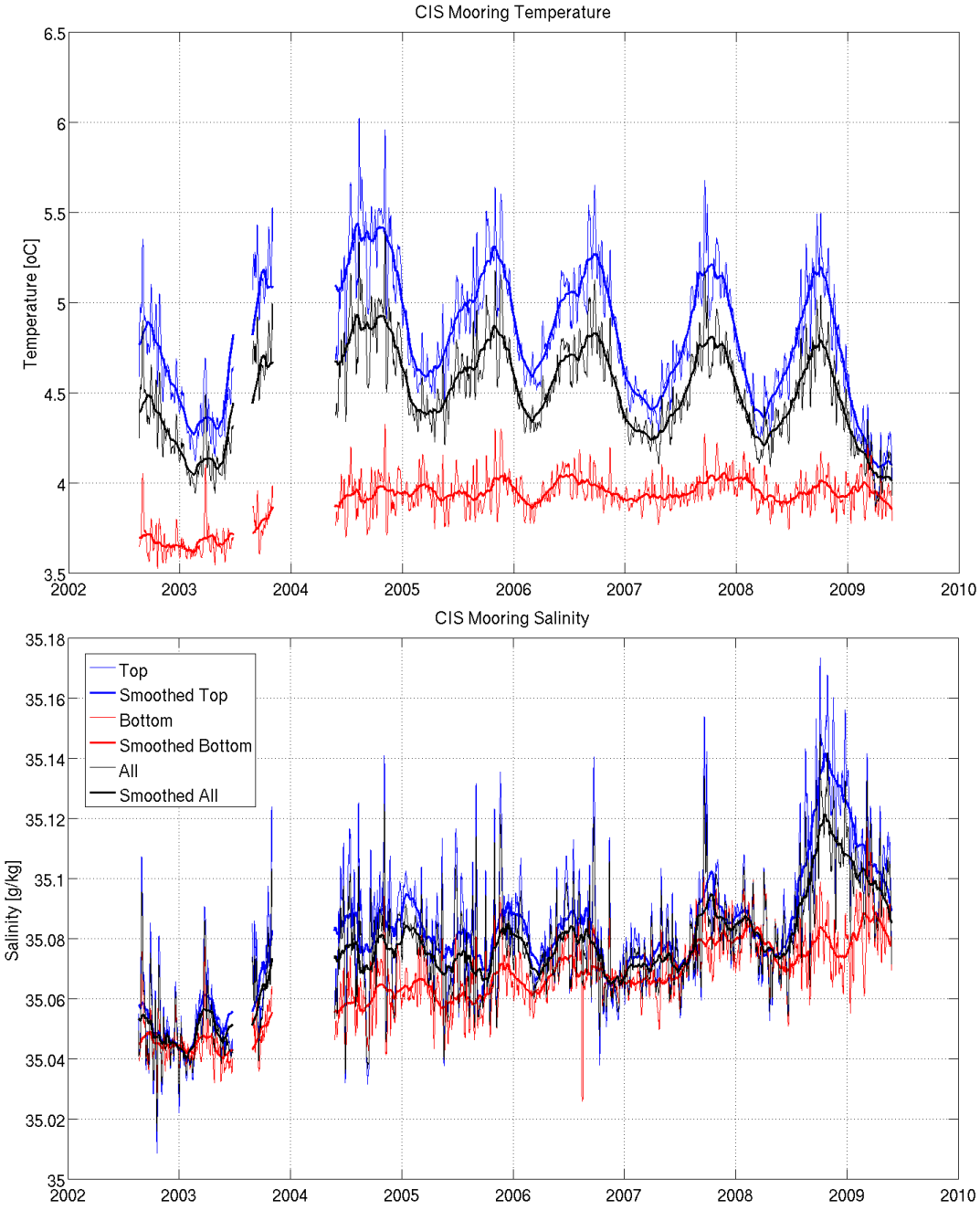

Figure 3.1: CIS mooring vertically-averaged temperature (top) and salinity (bottom). The 'Top' layer refers to an average from the surface to 460m, 'Bottom' layer is 460-1000m, and 'All', is surface to 1000m. The thicker line represents a 30-day smoothing.

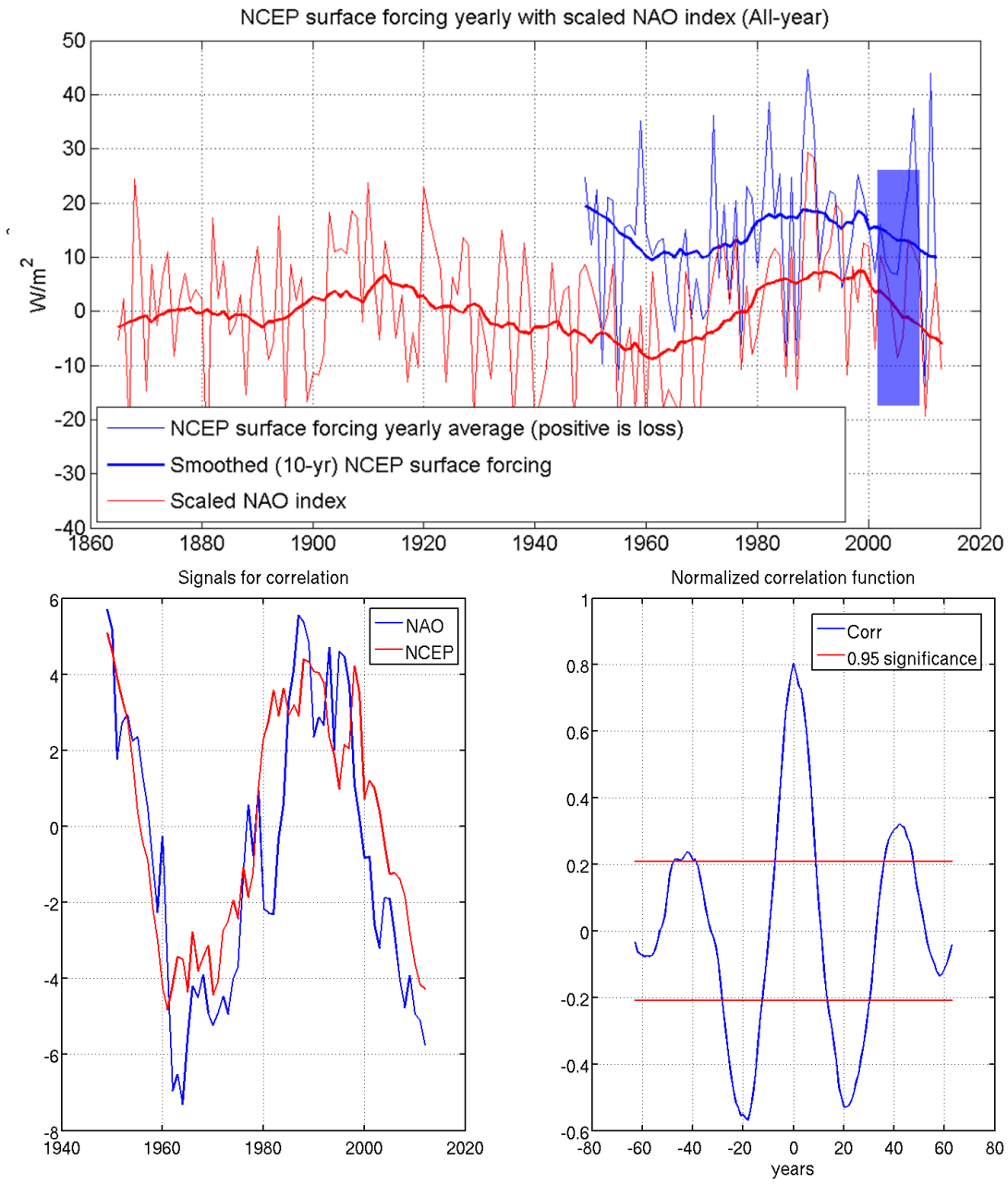

Figure 3.2: Correlations between NAO index and NCEP surface heat flux. Top: scaled NAO index (red) and NCEP surface heat flux (blue). Thin lines represent yearly (January to January) averages, while thick lines represent a 10-year running mean. Positive heat flux values represent a heat loss from the ocean to the atmosphere. The blue box highlights the time period overlapping with the mooring observations (2002-2009). Bottom left: zoom in of 10-year smoothed NCEP surface heat flux (blue) with mean removed and NAO (red). Bottom right: Normalized correlation function plotted with time lags. 0.95 significance level plotted with red lines.

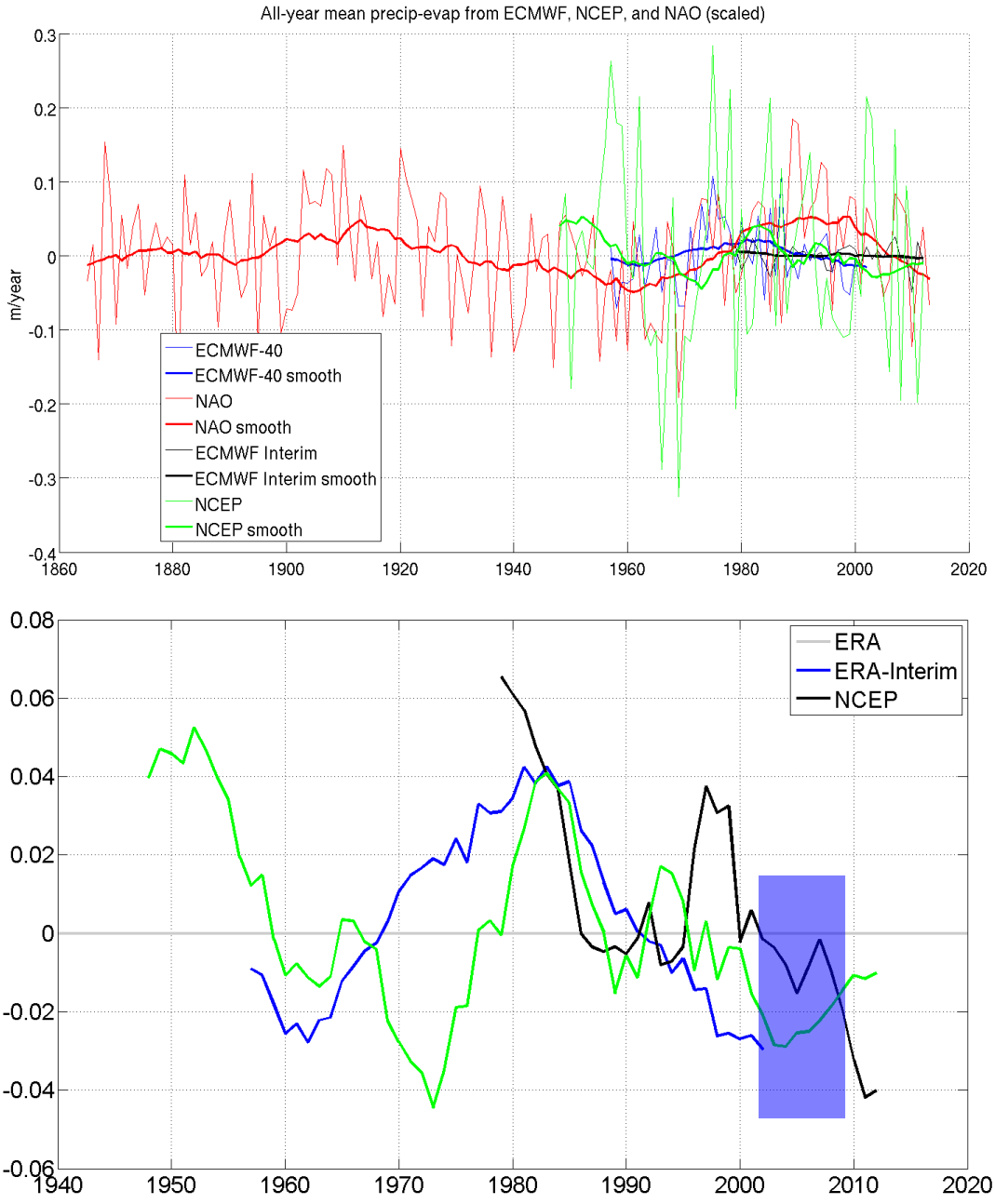

Figure 3.3: Correlations between NAO index and NCEO net freshwater flux. Top: scaled NAO index (red), ERA-40 (blue), ERA-Interim (black), and NCEP (green) reanalyses precipitation minus evaporation anomaly in units of meters per year. The solid lines represent a 10-year running mean. Bottom: Zoom in for overlapping region from top panel showing 10-year smoothed values of net surface freshwater anomaly in m/year. The anomalies are calculated with respect to the means of each dataset. The blue box highlights the time period overlapping with the mooring observations (2002-2009).

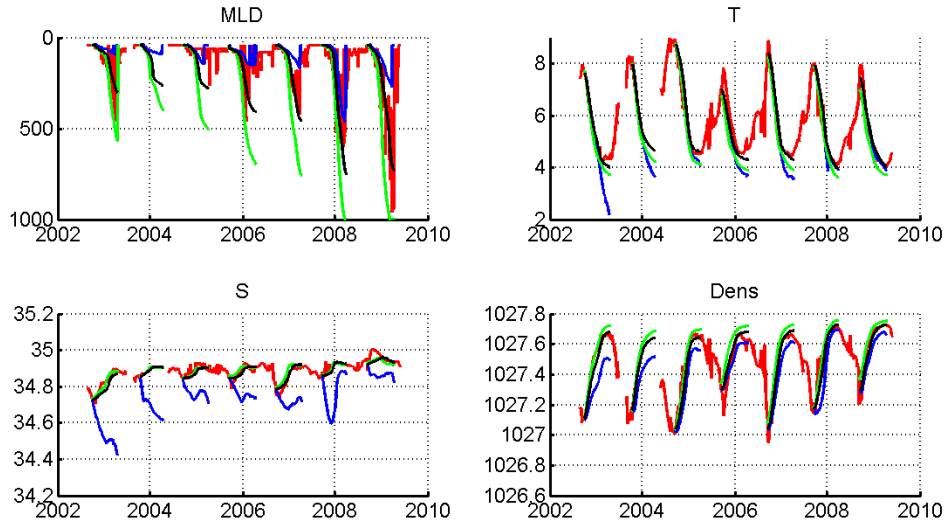

Figure 3.4: Mixed layer model results using different NCEP heat and freshwater fluxes. Colors in all plots show actual mooring observations (red), results from the mixed layer model using uncorrected heat flux from NCEP and zero net freshwater input (green), corrected heat flux from NCEP and precipitation/evaporation values from NCEP (blue), and corrected heat flux from NCEP with zero net freshwater input (black). All NCEP values are taken at the grid point nearest to the mooring location.

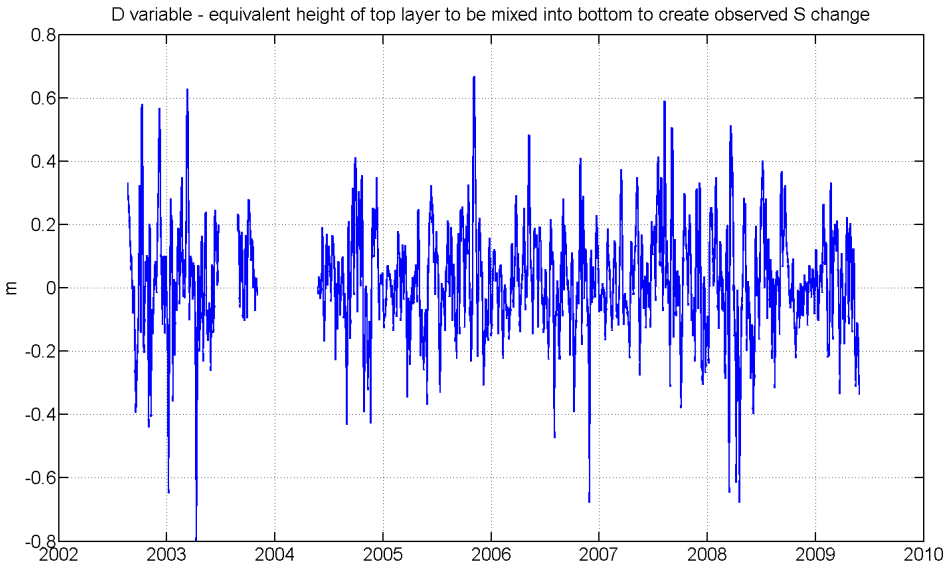

Figure 3.5: Equivalent *D* from equation 3.10

.

Chapter 4

Eddy decay during winter mixing

4.1 Abstract

We examine a possible mechanism to explain the lack of anticyclonic eddy observations during the winter months (January to June) at the CIS mooring location and throughout the Irminger basin. It was determined by various model studies (e.g. Dewar and Killworth, 1995; Katsman et al., 2003) that mixed barotropic-baroclinic anticyclones can abruptly enter a state where fast growth of unstable modes induces the decay of the eddy. In 2- and 3-layer simulations, this state occurred when the eddy flow is counter-rotating, meaning the bottom layer is rotating in the opposite sense to the upper layer. We examine the stability of our observed anticyclones by testing their sensitivity to changes in their barotropic component after a period of winter mixing. Using a simple 1D vertical mixing model, we observe a 10-20% reduction in the barotropic component of velocity after sustained periods (150 days) of surface heat loss and subsequent vertical mixing. This reduction resulted from the non-linear effects of the density profiles on buoyancy loss for a given heat flux over the eddy core compared to its periphery. This created deeper, denser mixed layers at the eddy core, which in turn created a larger decrease in dynamic height over the core after mixing, hence reducing the barotropic component. The decrease in barotropic velocity is enough to push the observed anticyclone into a counter-rotating state, where the idealized simulation studies described above show a state of instability. A general decrease in barotropic velocity is found in high salinity features at the mooring site, and basin-wide sea level anomaly (SLA) from

satellite altimetry shows larger decreases in SLA over anticyclones versus non-eddies over the winter period. We hypothesize that the preferential decrease in barotropic velocity may explain a mechanism for anticyclones to decay during winter mixing. If anticyclones are destroyed within the Irminger Gyre each winter, they will introduce a net heat and salt transport into the center gyre.

4.2 Introduction

In the previous chapters, we have observed warm and salty anticyclonic eddies in the Irminger Sea using various datasets. We have quantified the heat and salt input of these eddies and have compared the values to other terms in the heat and salt budget. The heat and salt input from the eddies appears to be vital in maintaining the temperature and salinity balance of the upper layer of Irminger Sea water over 7-year and longer time scales. Throughout these estimates, we have assumed that the anticyclones enter the basin from the boundary current and then do not leave the basin, thus depositing their warm and salty water into the basin. This assumption was suggested by the mooring observations, where there is a clear lack of eddy identifications using the method outlined in Fan et al. (2013) during winter months. This led us to believe that eddies could be destroyed during the winter period of heat loss and vertical mixing. The obvious question then follows: how are the anticyclones affected during winter mixing, and does this process promote eddy decay?

Model studies performed by Dewar and Killworth (1995) and Dewar et al. (1999) show the time evolution of 2-layer mixed barotropic-baroclinic vortices under a rigid lid and their growth of unstable modes. Katsman et al. (2003) perform a similar model study using a free surface and applying the same stability analysis to observed rings using various numbers of layers. In these studies, the 'barotropic' component explicitly refers to the component of velocity induced from a sea surface height anomaly. All studies show generally the same stability behavior: co-rotating rings remained coherent while counter-rotating or weakly co-rotating rings tended to become unstable, eventually splitting or decaying much faster than their strongly co-rotating counterparts. The Katsman et al. (2003) study used an anticyclonic model similar to our eddy observations; namely,

their vortices had dipping isopycnals (baroclinic component) and a doming surface expression (dynamic height representing the barotropic component). In the case of their 2- and 3-layer models, as the barotropic component increased in a counter-rotating regime, the growth rate of the first 9 unstable modes was quickly dampened upon passing the compensation point (where the lower layer is motionless). This point corresponds to the onset of co-rotation, where the barotropic component is large enough to create the same direction of rotation in both the upper and lower layers. Results were less clear for a 4-layer model using parameters fit to two realistic oceanic eddies. In that case, growth rates showed a local minimum near the compensation point, but favored large growth for both co- and counter-rotating regimes.

This chapter will explore the barotropic and baroclinic structure of the anticyclones observed by the mooring and whether wintertime mixing can affect the barotropic component to push the eddies to a point of instability. This could explain their lack of occurrences during winter and justify our assumptions that eddies can input their heat and salt into the Irminger Sea because they do not leave the basin after entering. The study is structured as follows. Section 4.3 describes the data used, and section 4.4 reiterates the seasonal cycle observed in the anticyclones. Section 4.5 shows the structure of a typical anticyclone, and section 4.6 compares the differences between anticyclones before and after winter mixing using observations and a 1-D mixing model. Section 4.7 explores how the non-linear effects in density affect how the anticyclone's barotropic component of velocity responds to winter mixing, and a discussion follows in section 4.8.

4.3 Data/Methods

We use a combination of mooring, Argo float, and satellite altimetry data, all described in previous chapters. To evaluate the effects of vertical mixing on eddy profiles, we use the 1D mixing model mentioned in section 3.11 of Chapter 3, which is the same mixing model described in detail in De Jong (2010).

4.4 Seasonal cycle of eddies in the Irminger Sea

To reiterate the seasonal cycle of eddy observations, the reader is referred to 2.2 showing the mooring timeseries between 2002 and 2009 with eddy identifications indicated by white circles. There is a clear lack of eddy detections in the months between January and June of each year. One does observe patches of high salinity anomalies during this time, but the accompanying velocity signals of these features do not match the eddy detection criteria outlined in that chapter. These features could be eddies that have been affected by winter mixing. We will examine this possibility in detail shortly.

The eddy seasonal cycle can also be observed using satellite altimetry and Argo floats. Figure 4.1 shows eddy count statistics from three products: the Chelton eddy detection algorithm, thresholds in sea level anomaly (SLA) from altimetry, and from Argo floats profiling in the basin. The Chelton algorithm uses a set of criteria to identify closed contours of sea surface height that correspond to a positive anomaly (anticyclone) compared to its surrounding waters. Counts of identified anticyclones are made for each month of the year from 1992 to 2008. Interestingly, the Chelton datasets shows higher eddy detections during the first half of the year, and lower detections during the second half, the opposite of the mooring observations. The SLA from altimetry is also examined using a simple threshold and its result is shown in the middle panel of figure 4.1. At each altimetry time step, we remove the basin-wide SLA from the signal. This eliminates biases due to the SLA being calculated with respect to the 1992-2005 mean as well as the basin-wide seasonal cycle fluctuations. We calculate the mean percent coverage of SLA greater than 1 cm in the Irminger basin for each month over the years 1992-2009. The results show a larger percent coverage in the latter half of the year compared to the first half, corresponding to our mooring observations. The reason for opposing seasonal variability of anticyclones shown by the Chelton product and direct SLA thresholding is unclear; it is possible that the Chelton product identifies those anticyclones that are large and well-formed. These eddies may be strong enough to withstand the effects of winter mixing and may last longer than smaller, weaker eddies.

The Argo float profiles show a seasonal cycle that is very similar to the SLA threshold method and the mooring observations. The results are shown in the right panel of figure 4.1. The profiles within anticyclones are identified using the salinity

thresholding method explained in the appendix of Chapter 1 for data between 2004 and 2009. As explained in that chapter, eddies identified by this method include the smaller eddies that are not observed by satellite altimetry, and include eddies that are similar in origin to the mooring eddies. Here, we see the percent of float profiles in anticyclones is highest in the latter half of the year versus the first half. Because this dataset is more similar to that of the mooring eddies, we can confirm that the eddy seasonal cycle observed at the mooring is also observed throughout the basin. The seasonal cycle in SLA is similar and supportive of these observations. The eddy seasonal cycle from these various datasets indicates that processes during the winter period may be changing and eroding the anticyclones. We will now examine the differences between non-winter and winter anticyclones.

4.5 Typical eddy structure observed by mooring

Properties from a typical eddy observed by the mooring are shown in figure 4.2. The top left and middle panels show the temperature and salinity profiles of the eddy as it passes the mooring. The anticyclones all have a warm and salty core causing the dipping isopycnal shape associated with the eddies. Again, we follow the definitions of barotropic and baroclinic components used in Katsman et al. (2003); namely, that the barotropic component of velocity results from the sea surface height anomaly, and the baroclinic component results from the dipping isopycnals deeper in the water column. The top right panel shows the hodographs of velocity measurements at various depths from the mooring ADCP during the eddy passing. Notice the coherence of the signal with depth which suggests that various layers of the eddy flow in the same direction (co-rotating state). The hodograph shape and symmetry imply that the eddy was sliced near the center of its core, according to the methods outlined by Fan et al. (2013).

This specific eddy's core radius and translation vector were estimated by Fan et al. (2013). The translation vector is removed from the velocity measurements, and the resulting velocity component perpendicular to the eddy translation path is shown in the bottom left of figure 4.2. The anticyclonic sense of rotation in the eddy is evident. The estimated eddy radius provides the horizontal scale with which to calculate

geostrophic velocities. The bottom middle panel of figure 4.2 shows the geostrophic velocity relative to 600m (Vg^i_{600}). We can calculate the absolute geostrophic velocity by using a depth-averaged reference from the ADCP measurements. We take the reference to be the mean between 400m and 800m (centered around 600m), called V_{ref}, and add it to the geostrophic velocity calculations referenced at 600m to obtain the absolute velocity ($V^i_a = Vg^i_{600} + V_{ref}$) shown in the bottom right panel of figure 4.2. The barotropic component is large and dominates the circulation such that the overall eddy rotation is anticyclonic.

4.5.1 Eddy Stability Prescribed by Katsman et al. (2003)

Katsman et al. (2003) performed a linear stability analysis on rings using an N-layer shallow water model on an f-plane. They examined the stability of the basic state (described in their equation 2a) when subject to infinitesimally small wave-like perturbations (described in their equation 3). The growth rate of the first 9 modes was examined. In their N=2 (2-layer) analysis, the growth of all unstable modes decreases by one order of magnitude shortly after the eddy passes its compensation point. This stability point occurs when

$$g\overline{h_1} = g'_2\overline{h_2}, \tag{4.1}$$

where h_1 and h_2 are the sea surface deviation and interface deformation, respectively, and $g'_2 = g(\rho_2 - \rho_1)/\rho_1$ is the reduced gravity of the bottom layer. While $g\overline{h_1} < g'_2\overline{h_2}$, the ring is counter-rotating, and $g\overline{h_1} > g'_2\overline{h_2}$ gives a co-rotating ring. They extend their analysis to 3- and 4-layer rings to approach more realistic ocean stratification.

Various parameters including layer thicknesses and deviations, and the shape and size of the modeled rings differ from the observations of anticyclones made by the CIS mooring. Therefore, it is unclear how using parameters reflecting our observed anticyclones would change the result of the stability analysis. The setup most closely reflecting the structure of our observed rings is that of the 3-layer model in Katsman et al. (2003). In this setup, layer thicknesses were set at $H1 = 40m$, $H2 = 500m$, and $H3 = 3000m$, using their definition shown in their figure 1. Simplifying our observed eddy structure in figure 4.2 into a 3-layer structure, the top layer would occur near the surface where isopycnals begin dipping (above 200m), and the second layer would

be approximately 600m thick corresponding to the layer of the maximum dipping of isopycnals. In the stability analysis of the 3-layer model ring, Katsman et al. (2003) find a similar result to the 2-layer case: growth of unstable modes is suppressed once the rotation of the bottom layer co-rotates with the top two.

To examine the level of co-rotation in our observed anticyclone (and thus, the stability criteria for growth of unstable modes), we plot the average velocity over layers 1 and 2 with the average velocity over layer 3 within the eddy core, shown in figure 4.3. The black dashed line indicates the point of complete co-rotation, when the velocities in the upper and lower layers rotate together at the same rate. The observed anticyclone's layer velocities are shown with grey crosses, and a line is fit to the data indicating a positive slope. Positive slopes in this case mean that we have a co-rotating flow. A more weakly positive slope corresponds to weaker co-rotation. A negative slope would indicate a reversal of flow in the bottom layer and a counter-rotating regime. Here, our observed eddy is co-rotating, satisfying the stability criterion in the 3-layer model in Katsman et al. (2003).

4.6 Comparison of eddy structure before and after winter mixing

We have observed a marked lack of eddy identifications during the winter mixing period from observations. In order to identify what process during winter mixing could be influencing the stability of anticyclones, we examine the structure of these eddies before and after the mixing period using both observations and the 1D mixing model described in Chapter 2.

4.6.1 Observations

An example of what appears to be an eddy that has undergone some mixing during the winter immediately following the eddy is shown in the top panels of figure 4.4. We can identify this feature from its still dipping isopycnals below the mixed layer, and also the salinity anomaly near its core (although much less defined than that of a

non-mixed eddy). The temperature and salinity profiles are shown on the top left and middle panels of figure 4.4. Here, the mixing has reached about 400m depth, and the eddy's dipping isopycnal shape still remains visible below this depth. The top right panel of figure 4.4 shows the velocity hodograph at various depths. Contrasting with the hodographs in figure 4.2, these do not exhibit a clear and coherent pattern at different depths, suggesting that the feature is no longer strongly co-rotating, as in the unmixed eddy. It should be noted that although this feature appears to be an eddy resulting from winter mixing, it is not identified as an eddy using the methods outlined in Fan et al. (2013) because it does not exhibit convincing hodograph shapes that one would expect. Again, this is an example of a potential eddy that is mixed, but likely not the result of winter mixing on the same eddy shown in figure 4.2.

4.6.2 Mixing Model

We start with the stable, co-rotating eddy shown in figure 4.2 and apply the 1D mixing model on every profile during its crossing. Again, the mixing model follows the one outlined by De Jong (2010). The result of applying a constant heat flux of -100 Wm^{-2} for 150 days on each profile is shown in the bottom panels of figure 4.4. The heat flux chosen in this example produces a mixed layer depth similar to the actual maximum mixed layer depth observed by the mooring that winter. Qualitatively, the temperature, salinity, and density profiles for the observed mixed eddy and the modeled mixed eddy are very similar. Within the homogeneous mixed layer, we can still observe some horizontal temperature and salinity gradients, although much weaker than in the unmixed eddy. Below the mixed layer, the dipping isopycnals are still preserved. Although we haven't taken into account any horizontal mixing in the 1D mixing model, it appears that vertical mixing alone can create a property profile in the eddy very similar to mixed eddies in the observations.

We examine the dynamic height, DH, defined as

$$DH = \frac{1}{g}\int_p^0 \frac{1}{\rho(S,T,p)} - \frac{1}{\rho(35,0,p)}dp \tag{4.2}$$

where $g = 9.8ms^{-2}$, and $\rho(S,T,p)$ is the in-situ density. The DH values are referenced to 1000 dbar, and we assume no change in the reference level from original to mixed

profiles. The *DH* calculation represents the steric response of the sea surface height to winter heat loss, and the associated change in sea surface height anomaly above the eddy is reflected in changes of *DH*. These changes in *DH* are shown in the left panel of figure 4.5 and are plotted with respect to the *DH* value at the end of the transect so the relative changes can be compared. For both the original and mixed eddy, elevated dynamic heights occur near the eddy core compared to the outskirts of the eddy. After surface heat loss and vertical mixing, *DH* decreases for all profiles (buoyancy loss), but the *DH* decrease is more pronounced over the eddy core than the periphery. This effect may seem counter-intuitive; one might expect the same *DH* change given the same heat removal over the entire anticyclone. We discuss the reason for this in section 4.7. The larger decrease of *DH* over the eddy core is more pronounced for more heat removal. This effect reduces the horizontal gradient of sea surface height which is responsible for the barotropic component of the eddy velocity. It is important to note here that the barotropic velocity derived from sea surface height is different from the depth-averaged velocity over the entire water column in cases where the baroclinic component is large. We calculate the the barotropic velocity, V, resulting from *DH* using geostrophy:

$$fV = g\frac{\partial DH}{\partial x}, \tag{4.3}$$

where g is gravity, f is the Coriolis force, and x is the direction across the profile. The right panel of figure 4.5 shows V values from the original eddy as well as the V resulting from various constant heat fluxes. The corresponding percent change in peaks of V after mixing are also displayed, showing a larger decrease in V with more heat removal. Here, winter heat removal and subsequent mixing can cause a weakening of the barotropic component of an anticyclone.

We can use the change in the barotropic velocity ($V_{corr} = V^i - V^{mixed}$) as a correction to estimate the effect on the total eddy velocity for a given constant heat flux, shown in the bottom right panel of figure 4.2. Here, V^i is the barotropic velocity resulting from the initial DH before mixing, and V^{mixed} is the barotropic velocity after mixing. Next, mixed absolute geostrophic velocities are calculated for each mixed profile such that

$$V_a^{mixed} = Vg_{600}^{mixed} + V_{ref} - V_{corr}, \tag{4.4}$$

where, V_a^{mixed} is the absolute geostrophic velocity of the mixed eddy, and Vg_{600}^{mixed} is the geostrophic velocity of the mixed eddy relative to 600 m. Absolute geostrophic velocity fields resulting from varying levels of heat loss are shown in figure 4.6. At a constant heat flux of -100 Wm^{-2}, the total velocity is tending toward the compensation stage. Compared to the original absolute velocity where the barotropic component was prominent throughout most of the 1000m-deep column, we can see near-zero velocities toward the bottom of the profiles. Once we reach a heat flux of -200 Wm^{-2}, it is obvious that the eddy is no longer co-rotating, and the baroclinic component is now large enough compared to the barotropic component to produce rotation of the opposite sign over the bottom half of the velocity structure.

For the different heat losses, the level of co-rotation (and thus stability) is shown in figure 4.3. Plotted is the mean upper layer (1-2) velocity versus the lower (layer 3) velocity within the eddy core for each different surface forcing case. The colors correspond to the same colors used in figure 4.6 for different heat losses. Again, we start with the grey crosses and fitted line showing a positive slope, indicating co-rotation (before mixing). As the heat loss is increased, we move toward a weaker positive slope, meaning the eddy moves towards a weaker co-rotating state. At a heat flux of -200 Wm^{-2} (black crosses and line), a reversal in the bottom layer flow is evident in the negative slope, and the eddy has entered a counter-rotating regime. According to the stability analysis of Katsman et al. (2003), if this eddy were like their 3-layer model, it would have entered a state where growth of unstable perturbations occurs, leading to the break-up of the eddy.

As mentioned earlier, the barotropic velocity derived from sea surface height expression does not equate to the depth-averaged velocity over the entire eddy in cases where the baroclinic component is large. However, we can examine the depth-averaged velocity of anticyclone features from the mooring ADCP data to gain insight into their rotational state throughout the year. A strongly co-rotating anticyclone will produce a large depth-averaged velocity magnitude, and a strongly counter-rotating anticyclone will have a small velocity in the depth-average because the opposing velocities will cancel. We use measurements between 2004 and 2006 (over 2 winter periods) where we have good velocity coverage at depths between 200m and 800m. We isolate salinity

anomalies using the same thresholding for salinity described in Chapter 2 (namely, features with salinity larger than one standard deviation from the mean salinity at a certain depth are considered anomalous). Most of these features were identified as anticyclones between June and January of each year, but they were excluded from identification between the winter months of January to June because their velocity signatures did not match the criteria prescribed in Chapter 2. Each salinity anomaly feature is isolated 3 days before and after its encounter with the mooring. The mean of the maximum depth-averaged velocity is calculated for features occurring in each month of the year, and shown in figure 4.7 for a given month of year. Between 5 and 10 features are identified each month of the year between 2004 and 2006. Depth-average velocity magnitudes begin high in the beginning of winter, and there is a clear decrease over the winter months. This observation supports the process we have been describing; as heat loss progresses through the winter, the anticyclone features experience a decrease in depth-average velocity associated with moving to a weaker co-rotating state. The decrease in the depth-average velocity is on the order of 10 to 20% of the maximum barotropic velocity shown in figure 4.5, and is large enough to move the eddy towards counter-rotation. These observations confirm the results from the 1D mixing model.

4.6.3 Observations from satellite altimetry

The preferential decrease in sea surface height above an anticyclone can also be observed in satellite altimetry. We can identify anticyclones using a simple sea level anomaly (SLA) cutoff; here, we will assume that positive (greater than zero) SLA can be considered anticyclones, and negative SLA is not. The method using Argo floats to identify anticyclones (mentioned earlier and described in Fan et al. (2013)) is also used to identify locations of anticyclones. Corresponding SLA from anticyclones identified by Argo floats and positive SLA are binned into each month for the years 2004-2010. The mean monthly SLA values are shown in figure 4.8 with their means removed. Obviously, seasonal variability will affect both eddy and non-eddy SLA, apparent in the figure. However, the variability within anticyclonic eddy values is much larger than non-anticyclone values. This observation directly supports our results from the mixing model, that changes in dynamic height (or sea surface height, or SSH) over an anticy-

clone are larger than changes over non-anticyclone. Not only is the SSH change more negative over an anticyclone after winter mixing, the change is more positive over an anticyclone after the Spring/Summer restratification period.

It is important to note that the mean monthly SLA values do not follow a single eddy, so they do not explain the time progression of an eddy through the different seasons. Instead, they are a snapshot of the current eddies in the basin. It may at first seem counter-intuitive that the monthly SLA shows a larger positive change during restratification, which could suggest a stronger barotropic component. However, if one is following a single eddy through the winter, the vertical mixing would have destroyed much of the density profile shape such that the restratification would not increase the barotropic component to the same extent as an eddy that has not experienced winter heat loss. Hence, the larger positive effect on SLA we observed in figure 4.8 shows the response of un-mixed, stable eddies under surface heating.

4.7 Non-linear Response in Dynamic Height from Given Heat Loss

During the process of winter mixing due to heat loss from the surface, we have observed that the dynamic height over the eddy core decreases faster than the eddy periphery given a constant heat loss. This weakens the horizontal gradient in dynamic height and reduces the barotropic component of velocity. This effect is due to the non-linear response of the dynamic height for a given heat flux. Numerous studies (e.g. Huang, 2010) show that for a given heat flux, the associated buoyancy change is not a conserved quantity. The buoyancy flux associated with a given heat flux Q and salt flux S, is

$$B_{flux} = \frac{g}{\rho c_p}\alpha Q + g\beta(E-P)S. \tag{4.5}$$

Here, α and β are the coefficients of thermal expansion and saline contraction. Because both α and β depend non-linearly on the actual temperature, salinity, and pressure, the total buoyancy removed for a given surface forcing depends on the properties of the profile.

Buoyancy content for a layer from the surface to depth Zo can be defined, following Schmidt and Send (2007), as

$$BC(Zo) = -g \int_{Zo}^{0} \rho(Zo) - \rho(z) dz. \tag{4.6}$$

This means that to mix vertically down to a certain depth Zo, the amount of buoyancy $BC(Zo)$ must be removed from the profile above Zo. According to Gill (1982), the coefficients α and β both increase with increasing temperature and salinity at a given pressure. Because our anticyclones have cores with high temperature and salinity compared to surrounding water, the buoyancy loss given the same surface forcing will be larger in the core of the anticyclone versus the periphery. The effect of this larger buoyancy loss is a deeper and denser mixed layer at the eddy core than what would be expected in the linear case. The resulting dynamic height is lower over the eddy core than the periphery in the non-linear case. In the linear case, we expect the change in the dynamic height after mixing to be the same regardless of whether we examine core or periphery profiles.

The non-linear response from a given heat loss can be quantified using our 1D mixing model. This model uses temperature and salinity values separately to predict mixing depth and mixed layer properties instead of a lumped buoyancy flux in order to account for the non-linear effects in the density calculation. We can evaluate how large this effect is by evaluating the mixing model's static stability criteria using the linear equation of state for seawater following Vallis (2006):

$$\rho = \rho_o - \alpha (T - T_o) + \beta (S - S_o) + \gamma (P - P_o) \tag{4.7}$$

where T_o, S_o, and P_o are the reference temperature, salinity, and pressure, respectively. These reference values are taken as the mean over the eddy profiles and is constant for each individual profile being mixed. For the purposes of this example, we use constant values of $\alpha = 1.21x10^{-4}\ {}^{o}C^{-1}$, $\beta = 8x10^{-4} psu^{-1}$, and $\gamma = 4.5x10^{-6} dbar^{-1}$; these values are similar to those reported in Marshall and Schott (1999) for the Labrador Sea and produce a density curve similar to the non-linear density for each profile. In the linear mixing example, we calculate the dynamic heights (DH, given in (4.2)) before and after mixing using the linear in-situ density calculated by the method above. The dynamic height sections before and after mixing for the linear and non-linear case are then compared.

The left panel of figure 4.5 shows the dynamic height before and after mixing using the linear and non-linear densities. The starting profiles are again from the example eddy shown in figure 4.2, and the non-linear dynamic height is identical to the one shown in the top right panel of figure 4.5. It is immediately clear that in the linear case, the dynamic height change over the eddy core after mixing is much smaller than the non-linear case. This effect is more pronounced with a greater negative heat flux. The resulting barotropic velocities are shown in the right panel of figure 4.5. Negligible change in barotropic velocities is produced in the linear case, and only the non-linear case can explain the change in the barotropic component after mixing. The sections of velocity change so little that when they are plotted together on the same scale as the non-linear barotropic velocity, their difference is barely visible.

4.8 Discussion

Because we have observed fewer anticyclone occurrences during winter months using mooring and float measurements, we examine the effect of winter mixing on anticyclones observed in the Irminger basin. Vertical mixing appears to have a strong effect on eddy profiles. Results from a simple 1-D mixing model are quite similar to features containing high salinity anomalies and are likely eddies experiencing vertical mixing. Although eddy properties are quite homogeneous in the mixed layer, the eddy retains its dipping isopycnal shape below the mixed layer. Hodographs at various depths within these features show a less coherent shape than their non-mixed counterparts, suggesting that the barotropic component of velocity has eroded. However, the mixing does not appear to have much effect on the baroclinic component because horizontal gradients are still preserved.

The non-linear response to buoyancy forcing creates a stronger response in the eddy core. This effect preferentially decreases the dynamic height at the eddy core more than the eddy outskirts after a period of steady heat loss to the surface. This decreases the horizontal gradient in dynamic height and thus weakens the barotropic component of velocity. Evidence of this phenomenon can be found using both satellite altimetry and Argo floats. Sea surface height anomaly over eddies identified with both datasets

show a larger decrease over anticyclones compared to basin averages during the winter period. We have shown using the 1-D mixing model that the barotropic weakening is enough to push our example eddy out of its co-rotational state. Numerous model studies using various simple 2- or 3-layer eddies show an abrupt growth of unstable modes when leaving the co-rotational state. Here, we compare our eddy to a 3-layer analysis by Katsman et al. (2003); layer thickness parameters are comparable, but it is unclear whether other parameters (eddy size, shape of decay with radius, and magnitudes of the layer deviations) produce a different stability analysis. Tests done by Katsman et al. (2003) using a 4-layer model showed an unclear relationship between stability and the rotational regime. However, the parameters used in the 4-layer model were made to reflect other observed eddies which were quite different from the ones we have observed. In any case, we have shown that the non-linear affect of winter mixing can decrease the barotropic component of an anticyclone to the point of counter-rotation. Whether counter-rotation for our specific eddy is a criteria for growth of unstable modes is uncertain and requires further testing. If this does indeed lead to instability, we may have found a mechanism by which anticyclones are destroyed during winter mixing, and hence contribute their core water to the heat and salt budget of the Irminger Sea. Further work is required to determine the extent of the instability and eddy decay time scales to explain the lack of observations of anticyclones during the winter months.

Here, we have explored one possible mechanism for anticyclone decay. However, numerous studies have explored different aspects of the observed coherence of long-lasting vortices that have not been examined in this study. For Gulf Stream warm core rings, the location of formation from the boundary current traps the rings between the current and continental shelf, thus facilitating their recapture by the current (Brown et al., 1986). In the case of Agulhas rings, interactions between topographic features or neighboring rings in the retroflection area promote fast decay in the first 5 months of their life (Kamenkovich et al., 1996; Schonten et al., 2000), and only when the rings enter the South Atlantic subtropical gyre do they remain coherent for many years (Gordon and Haxby, 1990; Schonten et al., 2000). Furthermore, satellite observations have revealed systematic correlations between warm sea surface temperature (SST) anomalies and enhanced local wind stress in the tropics and subtropics (e.g. Chelton et al., 2001;

Hashizume et al., 2001; Polito et al., 2001; ONeill et al., 2003; Chelton et al., 2004). It is argued that the enhanced winds over warm water is maintained by downward fluxes induced by convective instability, and can thus contribute to convective instability in a warm core eddy. Finally, the interaction between anticyclonic eddies and internal waves has been shown in theory and ray-tracing simulations to trigger diapycnal mixing (Kunze, 1985; Kunze et al., 1995). Observations show elevated dissapation rates beneath eddy cores, thus contributing to their decay (Padman et al., 1990; Kunze et al., 1995). It is possible that numerous processes described above contribute to the stability and eventual decay of the anticyclones in the Irminger Sea. Further studies are needed to examine these processes individually and how they contribute to the decay of the anticyclones we have examined.

Chapter 4 benefited from the co-author, Uwe Send, who provided valuable guidance and insight in this work. Funding for the CIS mooring was provided by the European Ocean Observatory Network (EuroSITES). Altimeter data was provided via the AVISO website (*www.aviso.oceanobs.com*). Argo data was provided by the USGADAE Project website ($http : www.usgodae.org$).

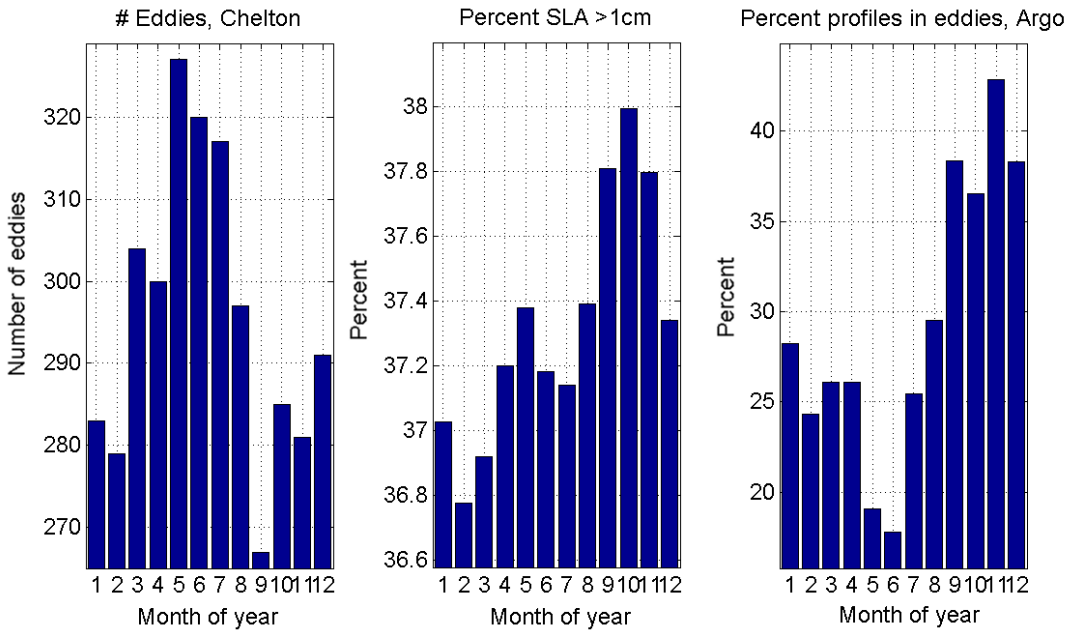

Figure 4.1: Total counts of anticyclones encountered in each month of the year determined by the Chelton algorithm, SLA, and Argo floats. Left: Total counts of anticyclones encountered in each month of the year determined using the Chelton eddy tracking algorithm. Values are totaled for data between 1992 and 2008. Middle: Percent coverage of values greater than 1cm using SLA from altimetry data. The mean SLA over the entire basin area is removed at each time step to eliminate the effect of the seasonal cycle and the original SLA data representing values with respect to the 1992-2005 mean. The mean percent of each month is calculated for fields from 1998 to 2008. Right: Percent of Argo float profiles within anticyclones determined by using the salinity threshold method outlined in the appendix of Fan et al. (2013). Values are calculated for profiles between 2004 and 2010.

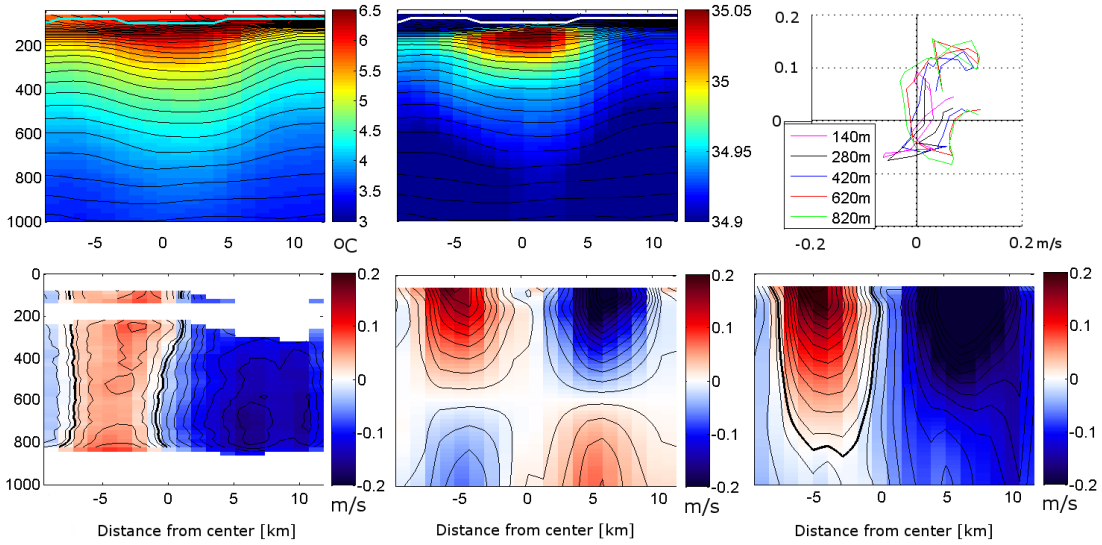

Figure 4.2: Property profiles and velocity structure of a typical anticyclone encountered by the mooring. Top left: Temperature profiles (color) with isopycnals (black). Top middle: Salinity profiles (color) with isopycnals (black). Top right: hodograph from mooring ADCP at various depths during the anticyclone passing. Bottom left: Velocity perpendicular to transect corresponding to a constant eddy translation speed and direction determined in Fan et al. (2013). Red represents velocities into the page. Bottom middle: Geostrophic velocities relative to 600m calculated using the estimated eddy radius and density profiles. Bottom right: Absolute geostrophic velocity using the geostrophic velocity relative to 600m and 400-800m depth-averaged ADCP velocity as reference.

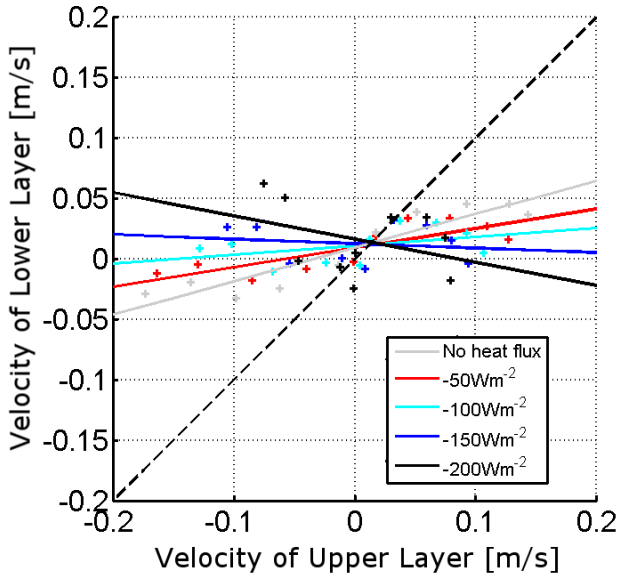

Figure 4.3: Mean upper layer (x-axis) versus lower layer (y-axis) anticyclone absolute geostrophic velocity within the eddy core resulting from different values of surface heat loss. The crosses represent actual values, and the solid lines represent lines fitted to those values. The dashed black line represents the complete compensation point, where the upper and lower layer flows rotate in the same direction and speed. Colors represent the original anticyclone with no forcing (grey), and the resulting velocity field after 150 days for a constant heat loss of -50Wm^{-2} (red), -100Wm^{-2} (cyan), -150Wm^{-2} (blue), and -200Wm^{-2} (black). A positive fitted slope means co-rotating flow. A flat (zero slope) line means compensated flow, where the bottom layer is stationary. A negative slope represents a counter-rotating flow.

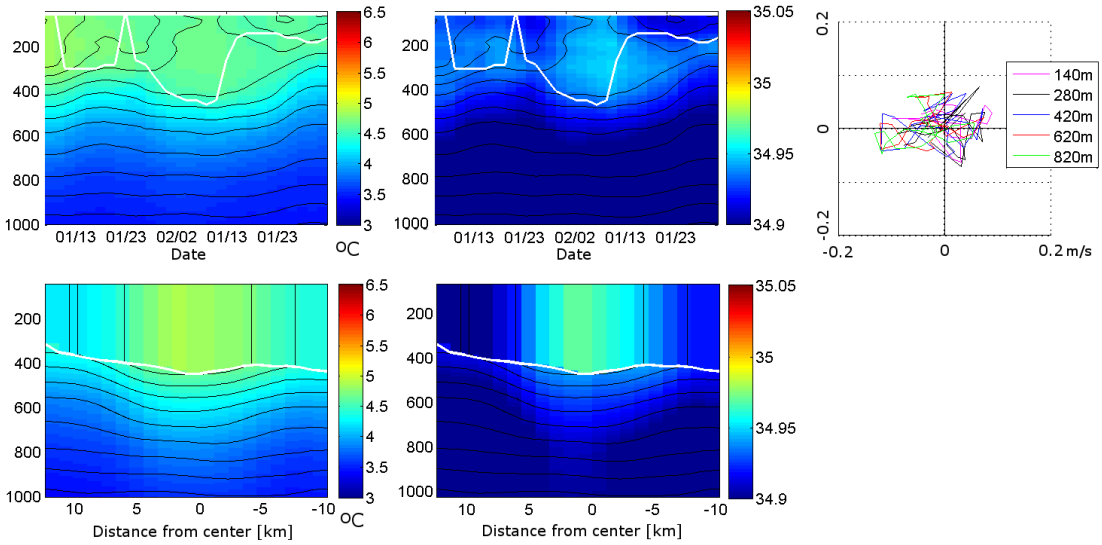

Figure 4.4: An example of an anticyclone after experiencing winter mixing. This feature was found in the winter immediately following the anticyclone example shown in figure 4.2. Top left: Temperature profiles (color) with isopycnals (black). Top middle: Salinity profiles (color) with isopycnals (black). Top right: hodograph from mooring ADCP at various depths during the anticyclone passing. Bottom: Result of the eddy shown in figure 4.2 with the 1-D mixing model applied to represent the effect of vertical mixing. Bottom left: Temperature profiles (color) with isopycnals (black). Bottom middle: Salinity profiles (color) with isopycnals (black).

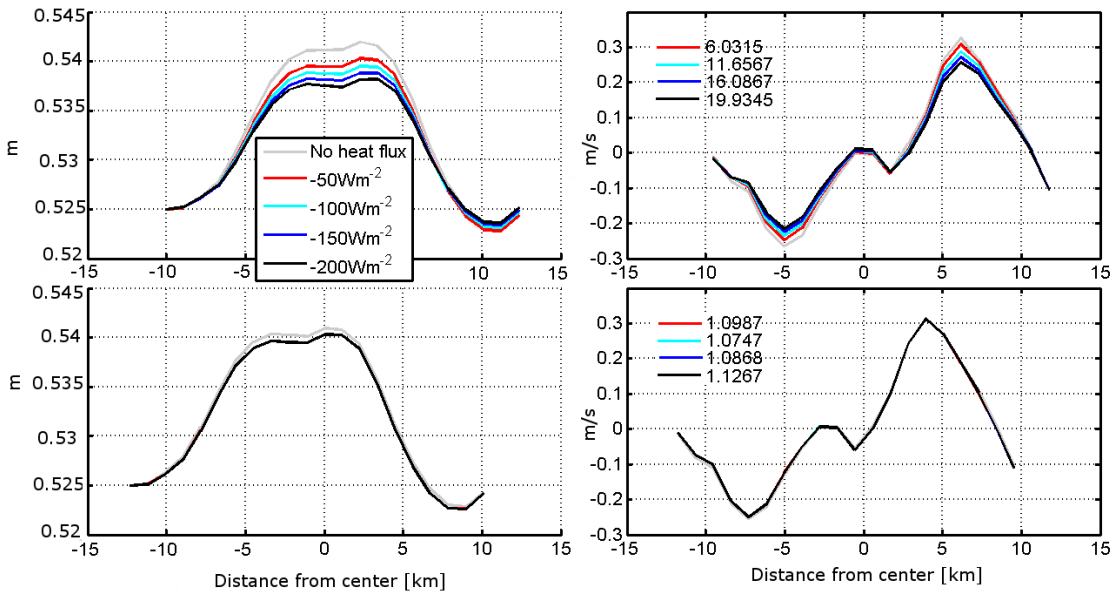

Figure 4.5: Change in dynamic height and barotropic velocity given progressively more heat loss from the surface, as predicted by the mixing model. Top left: Dynamic height relative to 1000m over the example anticyclone shown in figure 2.1 using the mixing model. The grey line represents no heat loss (original), and the resulting dynamic height after 150 days of constant heat loss is shown for -50Wm^{-2} (red), -100Wm^{-2} (cyan), -150Wm^{-2} (blue), and -200Wm^{-2} (black). The original profiles and the mixing model use the actual density profiles and non-linear density calculations. Top right: The resulting barotropic velocity calculated using geostrophy from the dynamic heights in the top left panel. The numbers represent the percent change in maximum magnitude of barotropic velocity change experienced compared to the original (grey) line for the different heat loss values. Bottom panels: The same dynamic height (left) and resulting barotropic velocity (right) as the top panels but using a linear density profile and linear mixing scheme. Note that in the linear case, the different colored lines representing different heat loss values show so little difference that they overlap, making them not visible.

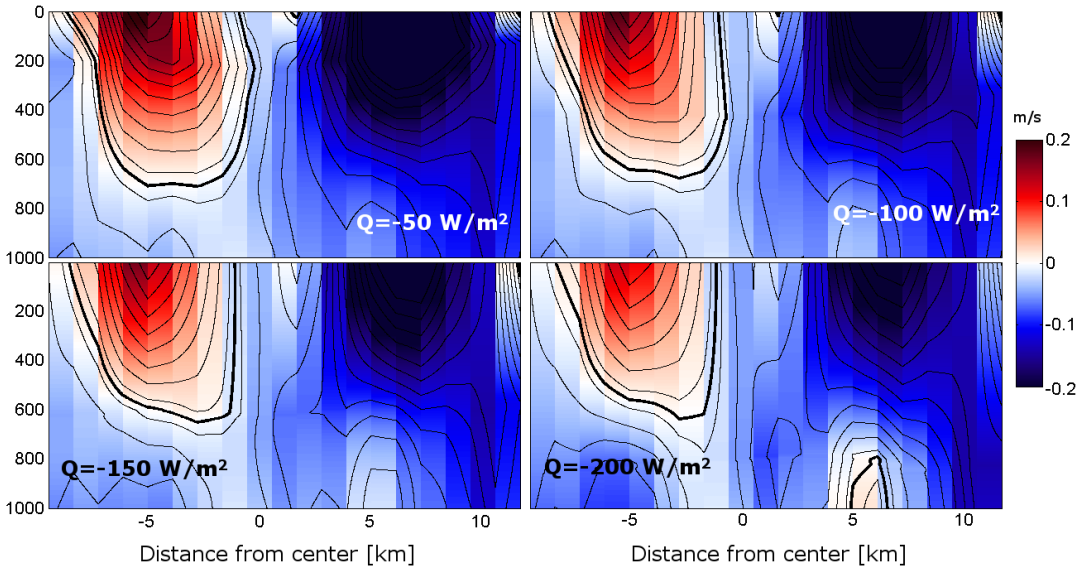

Figure 4.6: The resulting absolute geostrophic velocity expected after using the mixing model and same heat loss intervals described in figure 4.5. The change in the barotropic component corresponds to what is shown in the top right panel of figure 4.5. The velocity profiles are shown for a 150 day constant heat loss of -50Wm^{-2} (top left), -100Wm^{-2} (top right), -150Wm^{-2} (bottom left), and -200Wm^{-2} (bottom right).

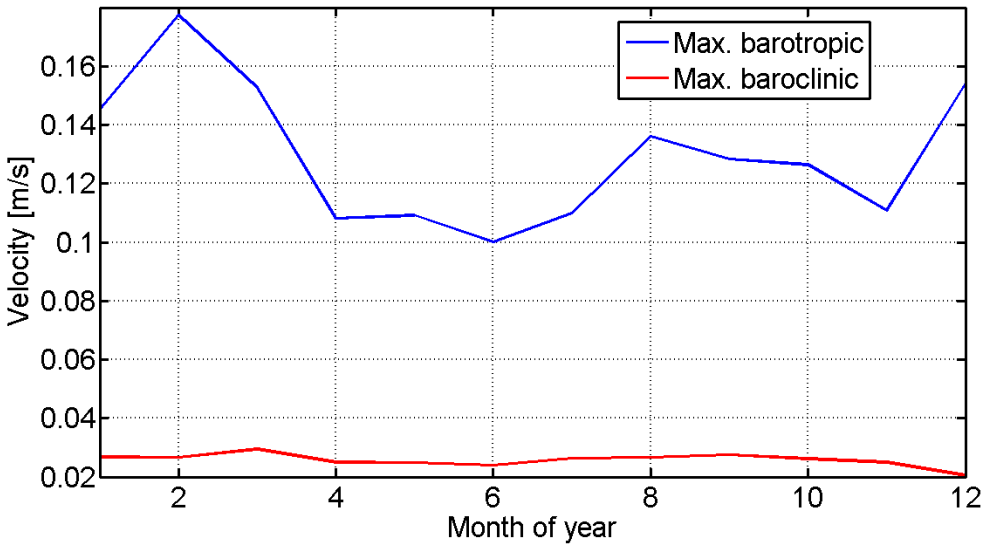

Figure 4.7: The mean of the maximum depth-averaged velocity of high salinity anomaly features observed by the mooring each month between 2004 and 2006.

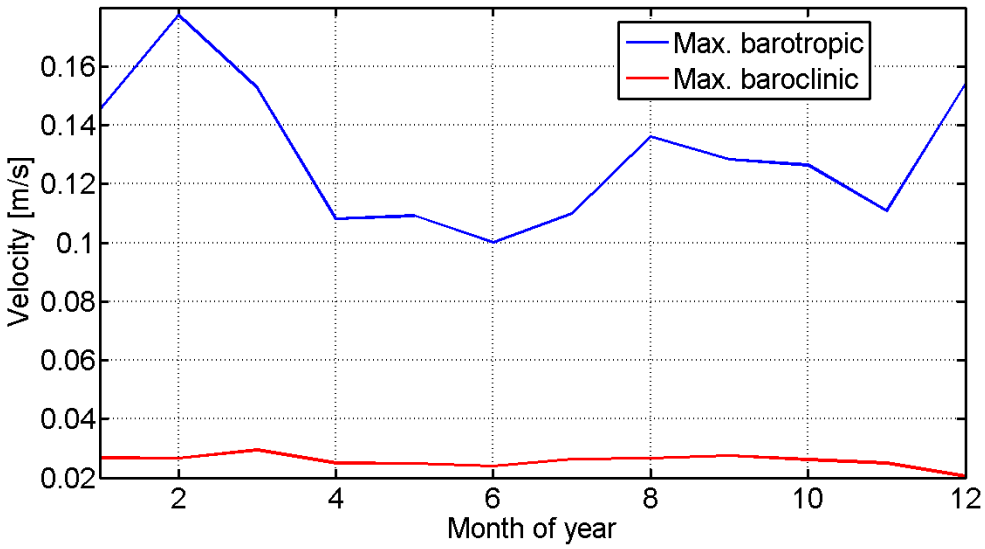

Figure 4.8: The mean anomaly in SLA experienced by features with positive SLA (blue) and negative SLA (black) from satellite altimetry for each month of the year for data from 1998 to 2008. The SLA corresponding to times and locations where Argo float profiles identify anticyclones is used to calculate the mean anomaly in SLA each month, shown with the red line.

Chapter 5

Anticyclones in the VIKING20 model

5.1 Abstract

We examine the output of a high-resolution regional eddy-resolving model for the time period coinciding with CIS mooring measurements. The model properly reproduces temperature values and seasonal variability in general, whereas it consistently overestimates salinity values. Mixed layer depths are reproduced well both at the mooring location and throughout the Irminger basin. The onset of the model winter mixing tends to precede observations by one or two months. Warm, salty anticyclones are widespread throughout the Irminger Sea in the model and share structural similarities with observed anticyclones. However, model anticyclones are consistently found to exhibit a larger temperature and salinity anomaly, and are more energetic. A method is developed to identify model anticyclones using the geometric structure of the velocity field. Statistics from identified anticyclones show a percent horizontal area coverage similar to those of the 4 methods used in Chapter 3. Large eddy features appear to stay in the eastern part of the basin, whereas smaller features stay in the west, coinciding with the size distribution of anticyclones throughout the Irminger basin proposed in Chapter 2. There is no clear seasonal cycle in eddy counts, which contrasts with eddy observations from various sources. One large anticyclone is tracked over the winter period. Using the model-prescribed diffusivity and viscosity, we determine that the decay of the tracked anticyclone core can almost entirely be attributed to model diffusivity of a tracer field and model viscous effects on the momentum field. Thus, the model eddies' decay

is largely controlled by model parameters and likely not by actual physical processes, like the one discussed in Chapter 4. This can explain why there is no clear seasonality in the eddy counts in the model as we have seen in observations.

5.2 Introduction

There has been a marked improvement in coupled ocean-atmosphere models due to many factors including a better understanding of the physics and more powerful hardware and software to deal with increased model resolution. However, most global models do not resolve eddy-scale dynamics at high latitudes. Therefore, it is difficult to reproduce various eddy-scale phenomena that may play an important role in the physics in the North Atlantic. For example, anticyclonic eddies have been shown to be a common phenomenon in the Irminger Basin (Fan et al., 2013) and provide an important contribution of heat and salt to the basin property budgets. Therefore, we examine output from an eddy-resolving regional model, VIKING20 (Behrens, 2013) to evaluate its ability to properly reproduce the anticyclones we have described in previous chapters. This model has been shown to be useful in improving the characterization of the effect of Greenland ice melt on neighboring ocean basins (Behrens, 2013), and is based on the NEMO ocean engine which has been used extensively in the study of properties and variability in the North Atlantic region (e.g. Böning et al., 2006; Biastoch et al., 2008; Griffies et al., 2009; Behrens et al., 2013).

The purpose of this study is to compare the eddies produced by the model to the anticyclones observed in the two previous chapters. The ultimate goal is to evaluate the ability of the VIKING20 model to reproduce eddy-scale features and variability in the basin to determine the accuracy of eddy heat, salt, and energy fluxes. Various eddy statistics are examined and compared to observations. The model eddy budgets of heat and salt will be effected by the way these features are portrayed. The structure of this study is as follows. The model description is presented in section 5.3. The model temperature and salinity fields are discussed in section 5.4. A method for eddy identification is developed in section 5.5, and individual eddy structure is explored in section 5.6. General model eddy statistics are shown in section 5.7, and eddy origins are

discussed in section 5.8. Finally, the fate of the anticyclones is examined in section 5.9 followed by a discussion in section 5.10.

5.3 VIKING20 Model Description

The model used in this study is based on the NEMO (Nucleus for European Modelling of the Ocean) model (Madec, 2008). This model uses the Boussinesq approximations of the hydrostatic primitive equations on a discretised Arakawa C-grid (Arakawa and Lamb, 1977). The VIKING20 is a newly developed configuration using a nested North Atlantic domain embedded into a global domain. The VIKING20 configuration is run on an eddy-resolving grid a horizontal resolution of $1/20^o$ (about 3 km resolution) and has 46 vertical depth levels. For details on the model configuration, parameters, and initial conditions, please see Behrens (2013). For this study, we use a time period overlapping with the CIS mooring data (see Fan et al., 2013) with a temporal resolution of 5 days.

5.4 Model Temperature and Salinity

We will first examine how well the model reproduces properties observed in the Irminger basin. The left panels of figure 5.1 show snapshots of the temperature and salinity fields at 50m depth on July 15, 2003, produced by the model runs. For comparison, scatter plots of temperature and salinity observations at 50m from Argo floats between 2004 and 2009 are shown in the right panels. The model shows generally warm and salty water on the eastern portion of the basin, with cooler and less saline waters toward the center of the gyre. This zonal gradient is apparent in the Argo float fields and is reproduced by the model. However, the model consistently produces salinities higher than found in observations at this depth. Nevertheless, the basin-scale gradients have a similar structure to observations. The warm and salty Irminger Current can be seen in the model as it moves northward near the Reykjanes Ridge, and then wraps around to flow southward off the east coast of Greenland. This structure is an established flow pattern shown in figure 2.1 of Chapter 2.

Figure 5.2 shows the model temperature and salinity timeseries with depth at the grid point closest to the CIS mooring location from 2002 to 2010 (left panels), and the CIS mooring temperature and salinity timeseries (right panels). Again, the model appears to produce the correct temperature values, but is consistently biased high in salinity compared to the observations. The seasonal variability in temperature appears quite consistent with observations. The seasonal variability of the model salinity signal has a less pronounced correlation with observations. A recurring deepening freshwater layer is produced each year in the model, but this pattern is not as consistent in the mooring observations. In the observations, the salinity signal is dominated by high salinity patches in the upper 600m layer, but these features are less obvious in the model output. In terms of variability over the 7 years, there exists a general warming of the model water below the seasonal thermocline that is not reflected in the observations. However, the increase in salinity over the water column observed over the mooring timeseries is indeed reproduced by the model runs.

Mixed layer depths at the grid point closest to the mooring, as well as maximum mixed layer depths in the basin, are compared to Argo and CIS mooring mixed layer depths in figure 5.3. The Argo mixed layer depths are the compilation of individual profiles found throughout the Irminger, whereas the mooring mixed layer depth shows local vertical mixing at the mooring location. All mixed layer depths reach about 400m during winters of 2002 through 2007. Deeper mixed layers indicating deeper convection appear in the winters of 2008 and 2009 appear in the model and mooring mixed layer depths, but less so in the Argo dataset. The Argo dataset, having limited horizontal coverage, may not have encountered a location of deep mixing during those times because it is a highly localized process (Marshall and Schott, 1999). The model appears to properly reproduce these deeper mixed layers. In general, the timing of the onset of winter mixing occurs slightly earlier in the model than in observations. At the mooring location, the model's mixed layers begin deepening as early as September of a given year, compared to the mooring which usually begins its winter mixing in November/December. The maximum mixed layer depth in the basin reported by the model also begins increasing earlier than what is reported by the Argo dataset. The earlier onset of deep mixing in the model may have effects on the regional budgets as well as how mesoscale phenomena

respond to a different length of winter forcing.

5.5 Identifying Model Eddies

The temperature and salinity fields from the model (figure 5.1) show a mesoscale eddy field both near the boundary currents and in the center of the Irminger Gyre. Our interest in this study is focused on the anticyclones produced by the model. We first examine whether the model produces anticyclones similar to those observed in the previous studies by the CIS mooring and other datasets. Because we have velocity fields, we follow the eddy detection method outlined by Nencioli et al. (2010). Another popular method using the Okubo-Weiss parameter (e.g. Chelton et al., 2007) was tested, but due to the fine resolution of the model grid, the results using this method contained too much noise to identify mesoscale eddies. The Nencioli et al. (2010) method tests each grid point as a potential eddy center location using four constraints:

(i) the meriodinal velocity must reverse sign across the eddy center in a zonal transect, and its magnitude must increase away from the center;

(ii) the zonal velocity must reverse sign across the eddy center in a meriodinal transect, and its magnitude must increase away from the center;

(iii) the velocity magnitude has a local minimum at the eddy center; and

(iv) the velocity vectors must change with a constant sense of rotation around the eddy center to produce a closed cyclone or anticyclone. We will use this method to identify anticyclones and obtain their statistics.

5.6 Structure of Model Eddies

Figure 5.4 shows an example of one anticyclone in the VIKING20 model compared to an example of an anticyclone encountered by the CIS mooring. A clear coherent structure of high salinity is produced by the model, surrounded by velocities rotating in an anticyclonic manner. A local minimum in the velocity magnitude exists near the center of the high salinity patch, and velocities increase as we move away from the center (located at about -37.5 ^{o}). After reaching a maximum in velocity magnitude about 28km

away from the center, the velocity magnitudes drop off as the transect leaves the eddy periphery. This type of horizontal structure is very similar to the eddies observed by both the moorings as well as the gliders in Fan et al. (2013). However, actual salinity values in the model are higher overall than the observations, and the salinity in anomaly in the model eddy core is about twice that of the observations.

The salinity profiles from the model eddy show a homogeneous layer extending down to about 500m near the eddy core. The core appears to be more simple and homogeneous in structure compared to the observed mooring eddy. Properties below the homogeneous surface layer become similar in the eddy center and its periphery, suggesting that the eddy is surface-intensified. This observation is also supported by the structure of the magnitude of velocity, where the largest velocities occur near the surface and decrease with depth. The anticyclonic sense of the rotation is clear from the velocity magnitude. Observations of model eddies almost always have surface-intensified homogeneous property and velocity cores. Observations from the mooring show a surface-intensified salinity core, but the velocity structure is more barotropic. The maximum velocities achieved by the model eddy are 4 times greater than what is observed. In general, the model tends to produce eddies with faster rotation and larger core anomalies when compared to observations. Below about 800m, the model eddy velocities appear to diminish rapidly, and the main velocity structure coincides with the homogeneous property core down to about 500m.

5.7 Model Eddy Statistics

We use the eddy identification scheme described earlier to gather statistics on the model anticyclones. The left panel of figure 5.5 shows the percent of model anticyclones having different salinity anomalies. The salinity anomalies represent the 200-700m depth-averaged salinity anomaly with respect to the mean over the entire Irminger Basin designated by the ellipse in figure 2.1 of Chapter 2. This range of depths encompasses the largest signal in the model eddy cores. Although most model anticyclones have a positive salinity anomaly, the model anticyclones are identified by their velocity vectors and do not always contain high salinity anomalies. Anticyclones without a sig-

nificant high salinity anomaly are likely either locally-formed (not originating from the boundary current), or are at a decaying state where their salinity anomaly is no longer prominent. The following anticyclone statistics are calculated from anticyclones having a salinity anomaly more than one standard deviation larger than the mean salinity of the basin in the model. This threshold is shown as the red line in the left panel of figure 5.5 and is also the threshold used to identify positive salinity anomalies from observations in Chapter 2. The right panel of figure 5.5 shows the temperature anomaly corresponding to the same 200-700m depth average as the salinity distribution. In the model, most of the anticyclones have anomalously warm cores. From Chapter 2, a typical anticyclone had a salinity anomaly of 0.03 and a temperature anomaly of 0.28°C. In the model, the anticyclone salinity and temperature anomalies reach up to 0.3 and 3°C, respectively. The model anticyclones appear to have stronger anomalies at least an order of magnitude larger than in observations.

Figure 5.6 shows histograms of the model eddy anticyclone radii for a given year. The radius is defined, as in Fan et al. (2013), as the distance from the center of the eddy to the maximum velocity magnitude. Here, this distance is calculated in 4 directions (north, south, east, and west) from the eddy center, and the mean of the 4 radii is reported. This takes into account the often slightly asymmetric nature of eddy structure. Most eddies exhibit radii between 20 and 40km, making the model eddies larger than most eddies observed by the mooring. Due to the $1/20^o$ grid spacing, one would expect the smallest resolvable model eddy to have a radius of 10-15km, which appears to be the cutoff of the eddy sizes in the analysis. Many of the eddies observed by the mooring are smaller than 10km radius, so these eddies cannot be resolved by the model, and only the largest mooring eddies are reproduced.

From the eddy size statistics, we calculate the percent area coverage by the anticyclones throughout the Irminger basin. In Chapter 3, this parameter was used to determine the total eddy heat and salt input by the eddies using four different methods. Figure 5.7 shows the percent area coverage by the anticyclones in the Irminger basin. Percentages each year usually range between 10 and 30%, which are similar to the range of percentages (ratios) obtained from the 4 methods using different observations in Chapter 3. This suggests that the model is able to produce realistic statistics regard-

ing the amount of Irminger Gyre water occupied by anticyclones. Total eddy counts (not shown) range from 5 to 20 each year, and their curve looks almost identical to the percent area coverage plots of figure 5.7. The mean correlation coefficient between the percent area coverage and eddy numbers at zero lag over the 8 years of model output is 0.84, meaning eddy horizontal coverage and eddy numbers are highly correlated. This suggests that the variability in the eddy area coverage over the basin is largely controlled by the number of eddies in the basin and not by changes in eddy size.

Recall from Fan et al. (2013) that the mooring observations showed less anticyclone occurrences during the winter period coinciding with convection and deep mixing. Eddy percent coverage (and counts) from the model do not show a consistent seasonal cycle from year to year as clearly as the observations. Some years, eddy occurrences peak in the summer, as with observations, but other years (2003, for example), the model shows eddy coverage (and counts) consistently increasing as winter approaches. This suggests that the model may be neglecting a factor of the seasonal cycle that directly affects the anticyclones in the real ocean.

5.8 Eddy origins and formation regions

The origins of the salty anticyclones were discussed in Fan et al. (2013). There was strong evidence for the eddies to be formed from the Irminger Current surrounding the basin, and then propagating into the interior. Two formation regions were identified: one on the western part of the Irminger Current near the southern tip of Greenland, and the other on the western flank of the Reykjanes Ridge. Potential vorticity (PV, defined as vertical stratification) was used to separate eddies coming from either site. We attempted to use the same method to trace eddy origins in the model. However, the model did not show two distinct potential vorticity values at the formation sites, and the anticyclones' distribution of potential vorticity was also unclear. It appears that the model vertical stratification does not fully capture what is seen in observations along the current and within the eddies, and is not a useful tracer to use in determining eddy origins in the model.

As in Fan et al. (2013), we examine the Eddy Kinetic Energy (EKE) from the

model to look for likely formation regions containing high EKE. Figure 5.8 shows the surface EKE calculated with respect to the mean velocity over the model period. This can be compared to the surface EKE available from satellite altimetry, also shown in figure 5.8 for reference. The magnitude of EKE in the model is very high compared to the observations from altimetry. This is not surprising, as the altimetry represents the geostrophic component of flow at scales coarser than the model resolution, and thus does not contain energy at smaller scales which the model can resolve. The model, in general, shows high EKE in the two formation regions found in the altimetry EKE, highlighted in the bottom panel of figure 5.8. The model also displays generally high EKE widespread throughout much of the southern part of the basin. This high EKE is not apparent in the altimetry observations. It is possible that the altimetry is not capturing much of the eddy activity in this region because the eddies are too small to resolve, or that the model is producing spurious eddies in this region. Nevertheless, regions of high EKE at the EGIC and RR formation regions do exist in the model output and can be a source for the anticyclones found in the center of the gyre.

We attempted to track anticyclone paths to determine their formation region. Our first attempt to identify eddy origins in the model made use of the eddy identification algorithm to trace eddies' pathways back to their first appearance in the model. Moving back in time, identified anticyclones were traced so that at a previous time step, if a feature was found within a certain radius, it would be considered the same eddy. This method proved difficult because often, the algorithm was too strict in identifying anticyclones so that no other anticyclones were found within a reasonable distance from the feature. Adding to this problem was the 5-day resolution of the model output which was often too coarse to follow a single coherent feature. Because of this, we adopted a more broad definition of the anticyclones using salinity to track them.

We assume that the high salinity anomalies we observe in the middle of the Irminger Basin are brought there via anticyclones because there are no local sources for this high salinity water. We can apply the same principles from the appendix of Fan et al. (2013) used to identify Argo float anticyclones using salinity anomalies. We calculate the large-scale smoothed salinity field by spatially smoothing the salinity at 200m depth for each model timestep with a window size of 150km. This size window

will preserve the basin-scale horizontal gradients. We subtract this smoothed field from the actual field at each time step, and contour salinity anomalies which are larger than one standard deviation above the mean salinity at each grid point. We call a feature an anticyclone if salinity contours are closed. This offers a more flexible eddy identifying method because the model produces eddies which are often distorted so that they do not appear to be a perfectly circular vortex, but are sheared or are in the process of interacting with other flow features. In this way, we can observe the movement of the high salinity anomalies being brought into the Irminger basin via anticyclonic eddies. We track these salinity anomalies by searching for the nearest salinity anomaly within 25km at the next time step. This is the maximum distance we expect an anticyclone to move in 5 days using the eddy translation speeds reported by Fan et al. (2013).

Visually, the high salinity patches all leave from the Irminger Current, appearing to peel off from both sides of the current surrounding the basin. Smaller features can be identified as coming off of the western formation region, and much larger features originate from the eastern region. Figure 5.9 shows the size distribution of high salinity patches throughout the basin. The equivalent radius is calculated such that the area covered by each patch would occupy a circle of that radius. There is a clear size gradient of features from the western to the eastern part of the basin, with the largest features found in the eastern part. In Fan et al. (2013), smaller anticyclones were determined to originate from the western EGIC region, while larger eddies formed from the eastern RR region. This distribution of size classes for anticyclones appears to be reproduced in the model output. This size distribution can be explained by examining the baroclinic Rossby radius. Assuming that the anticyclones form from baroclinic instabilities in the boundary current, we can expect the eddies to scale with the first baroclinic Rossby radius, defined as $R_1 = NH/\pi f$, where N, the buoyancy frequency, is

$$N = \sqrt{\frac{-g}{\rho_o}\frac{\partial \rho}{\partial z}}, \tag{5.1}$$

H is the layer height, and f the coriolis frequency. This scale is determined by the vertical density stratification ($\partial\rho/\partial z$), which we have also defined as Potential Vorticity (PV) in (2.6) of Chapter 2. From figure 2.8 of Chapter 2, the PV of the western formation region (EGIC) is 2-3 times smaller than that of the easter (RR) region. Thus, we expect

anticyclones forming from the western region to be smaller than those forming from the eastern region. This is what we observed in the basin (see Chapter 1) and in the VIKING20 model.

5.9 Fate of eddies

One important consideration in calculating the eddy heat and salt budgets from Chapter 2 was the fate of the anticyclones once they had entered the Irminger basin. To create a net heat or salt input, the eddies must enter the basin but not leave; in other words, they must stay there or be destroyed there. The CIS mooring measurements showed a clear lack of anticyclones during the winter months compared to other times of the year. A possible mechanism contributing to this seasonal signal was explored in Chapter 4. Here, we examine the behavior of the model anticyclones and their ultimate fate.

As mentioned earlier, the velocity algorithm used to identify eddies proved too strict to actually track the eddy movements, especially due to the 5-day resolution of the model data. We use the more relaxed eddy definition described in the previous section to look at the pathway taken by the high salinity features. For eddy tracks having at least 25 days of data, a total of 196 eddies is identified. Of these, 103 eddies enter the ellipse designated in figure 2.1 of Chapter 2. Ninety-two of these features enter inside the basin and stay, while only 11 leave after being inside. For eddies having tracks of 50 days or longer, a total of 59 eddies are found. Forty eddies enter the basin, 33 eddies stay within the basin, and only 7 eddies leave after having entered. From this analysis, it is obvious that most salty features associated with the anticyclones are not leaving the Irminger basin after they enter, and thus can contribute to the total salt (and heat) budget there.

Although most model anticyclones that enter the Irminger basin stay, there is no consistent, obvious annual cycle in model eddy counts (shown in figure 5.7), contrary to the mooring observations. This may be due to the mismatched timing of the onset of winter mixing between the model and observations, or other processes that the model is not capturing in order to create the same eddy seasonal cycle. It can be illuminating to

closely examine one eddy along its track. The 5-day time stepping in the model output is rather coarse for this type of detailed examination; however, we examine a period over 1997-1998 where daily model output is available. One large anticyclone was tracked manually through the winter convection period. The initial salinity field on October 13, 1997 and the eddy track is shown in figure 5.10. The minimum magnitude inside the salinity anomaly is assumed to be the eddy core center, and this point is tracked through July, 1998. Figure 5.11 shows a horizontal slice at 400m at different stages of its life. The strength and size of the salinity anomaly clearly diminishes throughout the eddy's life.

The eddy core temperature and salinity at various depths between the surface and 1000m following the eddy are plotted in the top panels of figure 5.12. The solid red line corresponds to 400m, the depth at which the horizontal slices shown in figure 5.11 are taken, and the blue lines show properties above 400m depth. The dashed red line indicates the basin-wide mean property at 400m depth. The seasonal cycle in the upper layer temperature is obvious as the eddy progresses through winter to summer. At depths of 400m and below, the eddy does not feel the temperature restratification in spring, and a steady temperature decrease is observed throughout the eddy lifetime. The temperature (and salinity) anomaly in this model eddy exists primarily in the upper 800m of the water column, and as the eddy signature fades, the temperature at 400m decreases to approach the mean temperature of the Irminger Basin at that depth. A similar overall decrease in salinity is observed in layers shallower than 800m. The 400m salinity decays throughout the eddy's life such that it approaches the mean basin salinity at that depth, meaning its salinity anomaly has eroded to meet ambient levels. It is interesting to note the step-like structure in the temperature and salinity timeseries following the eddy. Because we have the highest temperature and salinity anomaly near the surface, we observe a step-like increase in these properties in progressively deeper layers as the winter convection mixes deeper into the water column over time.

Along with the decreasing property anomalies, we also observe a decrease in the dynamic strength of the eddy measured by its maximum velocity and relative vorticity, shown in the bottom panels of figure 5.12. The maximum velocity is the maximum magnitude of velocity encountered when looking both zonally and meridionally across the

eddy. The vorticity is defined as $\partial v/\partial x - \partial u/\partial y$ and describes the strength of rotation of the eddy. The obvious steady decrease in maximum velocity and the tendency to zero of the relative vorticity indicate that the anticyclone is losing is rotational strength as it is decaying.

To examine the mechanism by which this model anticyclone decays, we assume a simple horizontal balance for salinity tendency:

$$\frac{\partial S}{\partial t} = -K\nabla^2 S - \vec{v}\nabla S. \tag{5.2}$$

Here, we assume the salinity signal is controlled by the model tracer diffusivity K and the horizontal advection of S. The model was run with a constant diffusivity $K = 60m^2s^{-1}$. We use the model salinity fields at each time step to calculate each term in the above equation at each model grid point. The results at 400m are shown in figure 5.13 for a point just outside of the eddy maximum velocity (top panels) and the point following the eddy center (bottom panels). The right panels show the time-integration of the terms shown in the left panels, plotted such that they start at a common point.

Outside the eddy center, the tendency term appears to be mostly controlled by the horizontal advection of the tracer. The diffusion of salinity at this point has a slight negative offset, resulting in a slight decrease in the salinity signal in the timeseries. This decrease is reflected in the salinity timeseries shown in the left panel. At the eddy center, the horizontal advection term plays a much smaller role in the salt tendency (as expected, since velocities are very small here). The diffusion term is large, and its influence in decreasing the salinity in the eddy core is apparent. The difference between the left and right sides of (5.2) is shown with the cyan lines in figure 5.13. These represent what is not captured by our simple horizontal balance assumption, and is likely attributed to the vertical fluxes. The large spike around mid-February in the eddy core balance occurs at the time the increase in salinity is observed in the top right panel of figure 5.12. This is when winter mixing penetrates 400m depth, and is when we expect a large vertical flux (apparent in the cyan line at this time).

Because the diffusion term is large, we can conclude that within the eddy core, the decreasing salinity shown in figure 5.12 can be largely attributed to the model diffusivity, and thus may not properly reflect real eddy decay processes. The same can be said about the model eddy viscosity. Although we have not shown it here, the model

eddy viscosity produces a large decrease in the observed vorticity fields in the eddy center. Thus, the eddy's tracer and velocity dissipation that we observe in the model is due to the model's choice of diffusivity and viscosity and likely does not reflect real eddy decay mechanisms. This can explain the discrepancy between the observed seasonal cycle of the eddies and the lack of seasonal cycle in the model eddies. If the model is not properly reproducing the eddy decay during winter mixing, we may not expect to see the same observed seasonal variability of eddy occurrences.

5.10 Discussion

We have examined various aspects of Irminger Sea anticyclones and how they are represented in the VIKING20 model. Compared to observations, the model reproduces values of temperature quite well, but consistently overestimates salinity. However, seasonal variability in both temperature and salinity show close resemblance with observations. Mixed layer depths at the mooring location reflect mooring values consistently, but the timing of the onset of winter mixing tends to be earlier in the model compared to observations. Despite this mismatch, the timing of the spring restratification appears to coincide well with observations.

The model is able to produce warm, salty anticyclones as were observed by observations. Their core structure contains a homogeneous layer usually extending to 500m depth. Compared to observed anticyclones, this structure is rather simplified, but captures the essence of the vortex features. The model does not reproduce fresh water caps above the anticyclones which are often encountered in observations. The velocity structure of model anticyclones shows a nearly linear profile of increasing magnitudes while moving from the center to the edge of the core, suggesting a vortex structure in solid body rotation. The maximum velocities occur near the surface and decrease with depth, but a strong barotropic component is present, as with the observed anticyclones. An algorithm for anticyclone detection was developed, and the results show that most anticyclonic eddies coincided with high salinity and temperature anomalies compared to basin-averaged properties. Anticyclone size distributions showed most model eddies ranging between 20 and 40km radius. These eddies are at the high end of the range

of eddy sizes observed by the mooring, but due to the model resolution, we do not expect to see eddies smaller than 10-15km. Thus, the model resolves the largest eddies observed by the mooring, and larger eddies not found at the mooring location. Estimates of percent eddy coverage over the basin are within range of the yearly estimates made by 4 different methods in Chapter 3 using various observations, suggesting that the model is properly reproducing the spatial extent of anticyclones in the Irminger Gyre. However, the seasonal cycle of anticyclone occurrence is not reproduced by the model.

Model EKE shows regions of high energy coinciding with the two formation regions discussed in Chapter 2, as well as a general high EKE region in the southern portion of the basin. High salinity features in the model show a clear size gradient from the west to the east of the gyre, with the largest features occuring in the eastern region. This analysis supports the idea presented in Chapter 2 that larger eddies originate from the Reykjanes Ridge (eastern) region, and smaller eddies come from the East Greenland Irminger Current (western) recirculation.

An example of one anticyclone was followed through its lifetime in the 1-day resolution model runs from October to July of the following year. The strength of its property anomalies in its core and its rotational strength decreases through its lifetime until the feature is no longer identifiable. Using the model horizontal eddy diffusivity prescribed in the VIKING20 runs, it appears that the eddy core dissipation is largely controlled by the model diffusion. The same situation occurs for the eddy momentum; the eddy is largely dissipated by the model horizontal eddy viscosity. Thus, the break-up of this anticyclone in the model cannot be contributed to eddy physical processes and is largely governed by the model parameters. This might explain the lack of clear seasonal cycle in the eddy occurrences in the model compared to observations. Because we see a clear lack of eddies in the wintertime observations, we presume that processes during the winter contribute to the decay of eddies at that time. The model does not show an obvious difference in rates of tracer (salinity) dissipation or decrease momentum over the winter period compared to spring and summer. Instead, a steady decline of eddy core anomalies and eddy strength occurs throughout the eddy life cycle. It is possible here that the model is incorrectly prescribing processes that determine its eventual decay. Even though most model anticyclones do not leave the center of the basin after entering,

the timing of the eddy decay may reflect incorrectly on the amount of transport of heat and salt is achieved by the eddies.

Because eddies have been shown to be an important contribution to the heat and salt budgets in the Irminger Sea (see Chapter 3) and in other North Atlantic basins (e.g. Gelderloos et al., 2011; Hátún et al., 2007; Nilsen and Falck, 2006; Köhl, 2007), properly representing these features in regional ocean circulation models is crucial to the accurate simulation of basin properties and processes. Mesoscale eddy features are often represented by either a parametrization of eddy-induced transport velocity (i.e. Gent et al., 1995), or by resolving eddy features themselves, as is done in the VIKING20 simulations used in this study. A comparison of eddy-induced heat fluxes between a low-resolution eddy parametrization and a high-resolution eddy resolving model using the NEMO engine (the same model engine used in the VIKING20 simulations) was performed in the Labrador Sea by Saenko et al. (2014). Their results show that although the low-resolution simulation qualitatively captures eddy buoyancy transport along the boundary current, it fails to reproduce the convergence of heat by eddies closer to the interior of the basin that the eddy-resolving simulation and observations show. Thus, the importance of resolving and correctly reproducing the mesoscale eddy features in this simulation prove to be essential in correctly quantifying the eddy-induced heat (or salt) transport in the region. In this study, we have the opportunity to compare observed eddies to model-resolved eddies, thus setting a gauge for how well the model simulations can reproduce realistic eddy transports.

Chapter 5 benefited from Uwe Send, co-author, who provided insight in this study. Thank you to Erik Behrens, co-author, who performed the VIKING20 model simulations and provided the data and support. Funding for the CIS mooring was provided by the European Ocean Observatory Network (EuroSITES). Altimeter data was provided via the AVISO website (*www.aviso.oceanobs.com*). The Chelton eddy identification dataset is provided on their website at $http://cioss.coas.oregonstate.edu/eddies/$. Argo data was provided by the USGADAE Project website (*www.usgodae.org*).

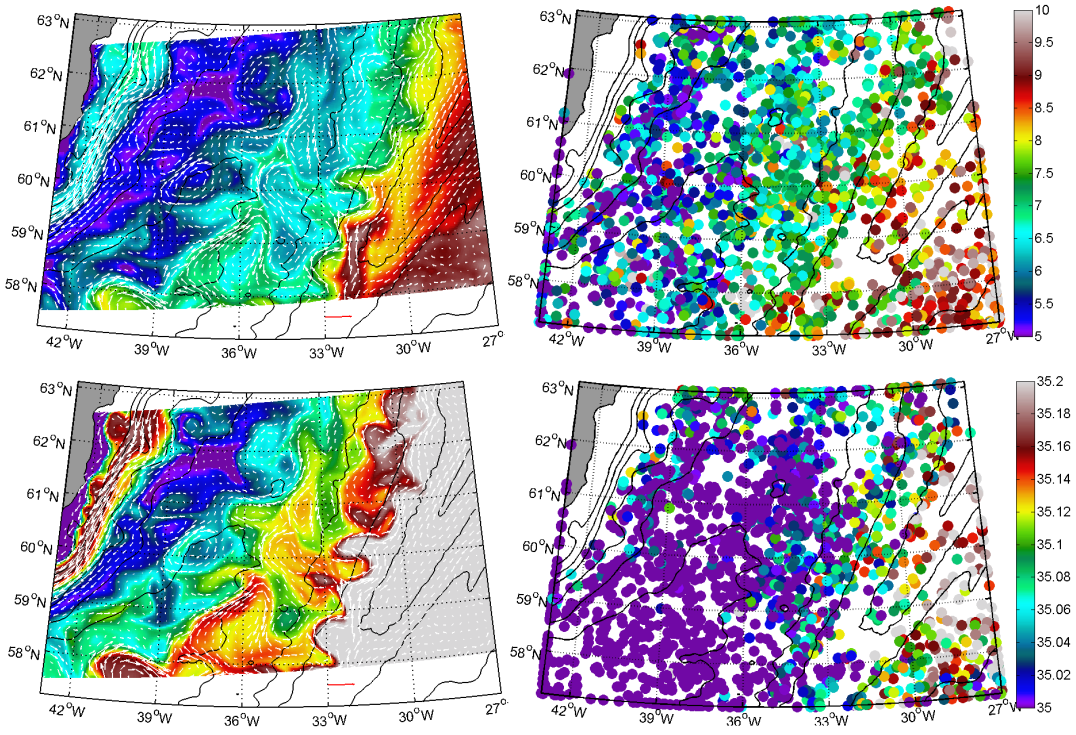

Figure 5.1: Example snapshots of fields from VIKING20 and comparison with Argo float data. Top Left: Temperature at 50m depth from VIKING20 model on July 15, 2003. Bottom left: Salinity at 50m depth from VIKING20 model on July 15, 2003. Top right: Compilation of Argo float temperature at 50m between 2004 and 2009. Bottom right: Compilation of Argo float salinity at 50m between 2004 and 2009.

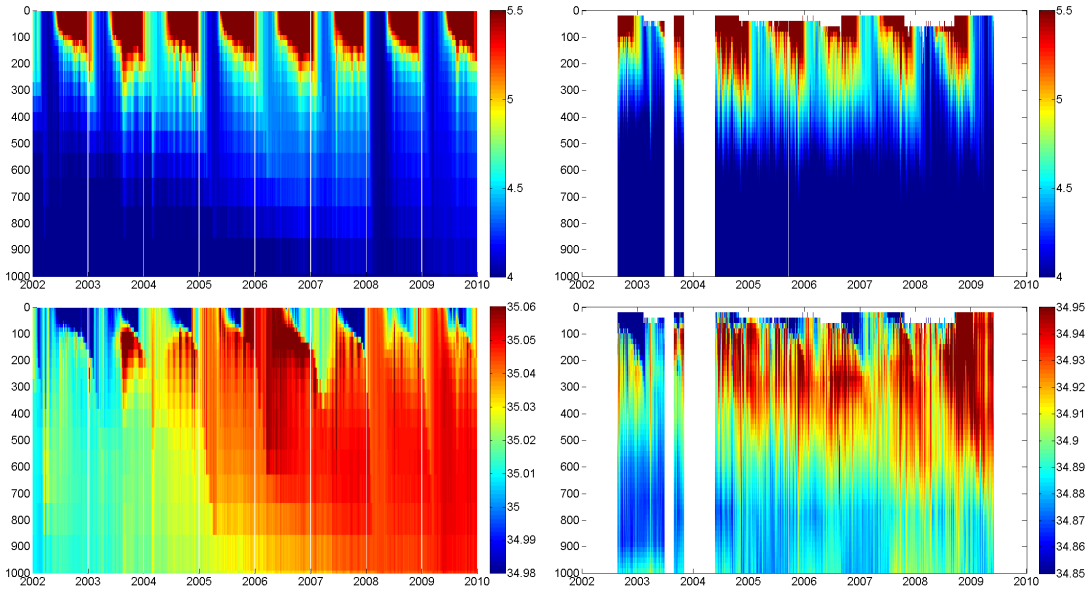

Figure 5.2: Temperature and salinity timeseries at various depths at grid point closest to CIS mooring location. Top left: Temperature time series with depth at grid point closest to CIS mooring location in VIKING20 model. Bottom left: Salinity time series with depth at grid point closest to CIS mooring location in VIKING20 model. Top right: Mooring temperature timeseries. Bottom right: Mooring salinity timeseries.

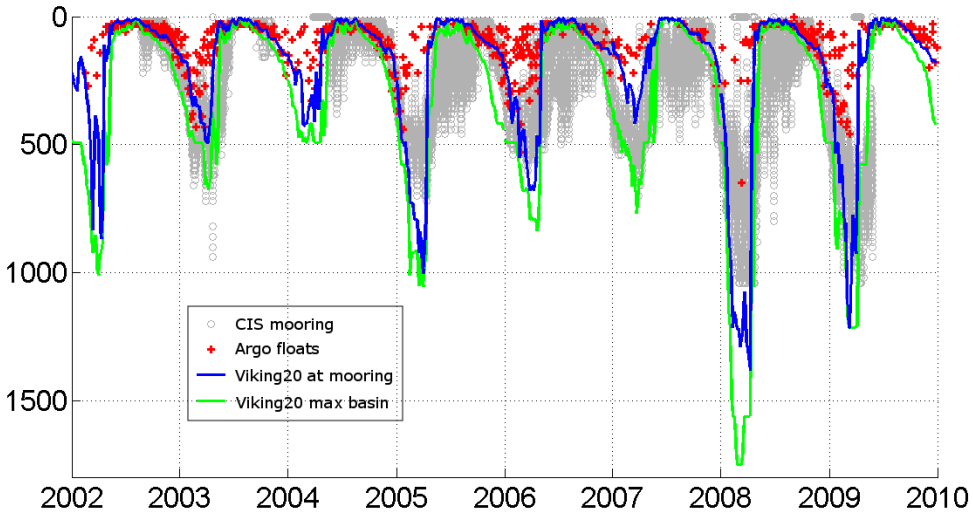

Figure 5.3: Mixed layer depths calculated using a density threshold of 0.01 kgm^{-3}. The grey circles represent mixed layer depths from the CIS mooring. The blue line shows mixed layer depths from the VIKING20 model at the grid point closest to the CIS mooring. The green line represents the maximum mixed layer depth inside the Irminger Gyre from the model output. The red crosses represent a compilation of Argo float mixed layer depths found throughout the CIS basin between 2004 and 2009.

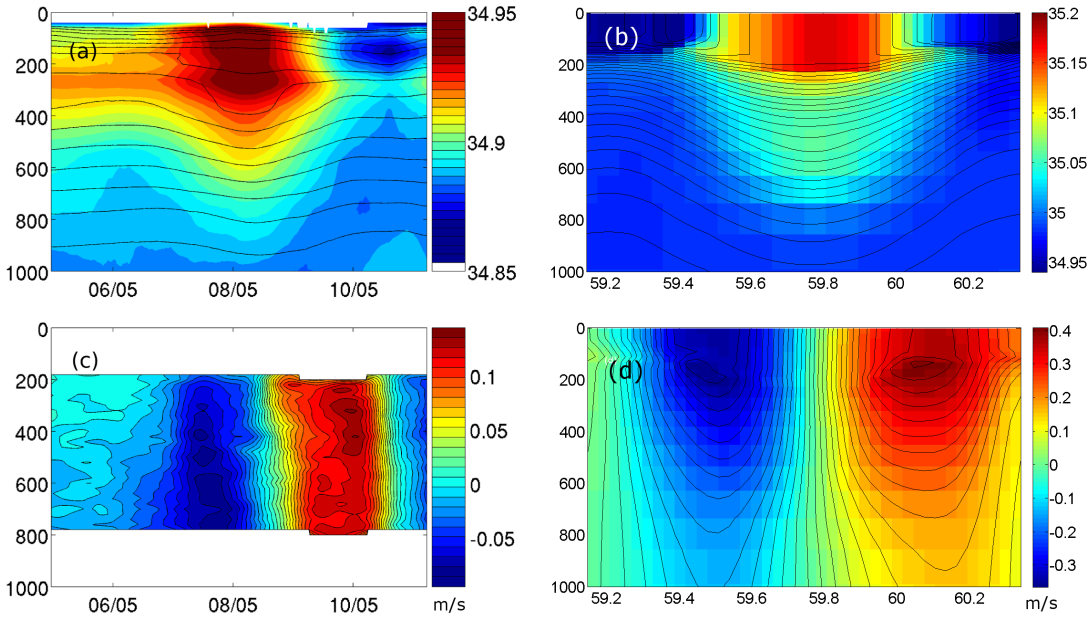

Figure 5.4: Example of an anticyclone observed by the mooring, also shown in figure 2.3 of Chapter 1. (a) the salinity field with depth (color) and isopycnals (black contours). (b) Example of an anticyclone in the model output. The salinity field with depth (color) is shown with isopycnals (black contours). (c) The eddy velocity field associated with the feature shown in the top left panel. The velocity is the component perpendicular to the path through which the eddy transects the mooring, and its translation velocity is removed. (d) The zonal velocity of a meridional slice taken through the eddy center of the example model eddy.

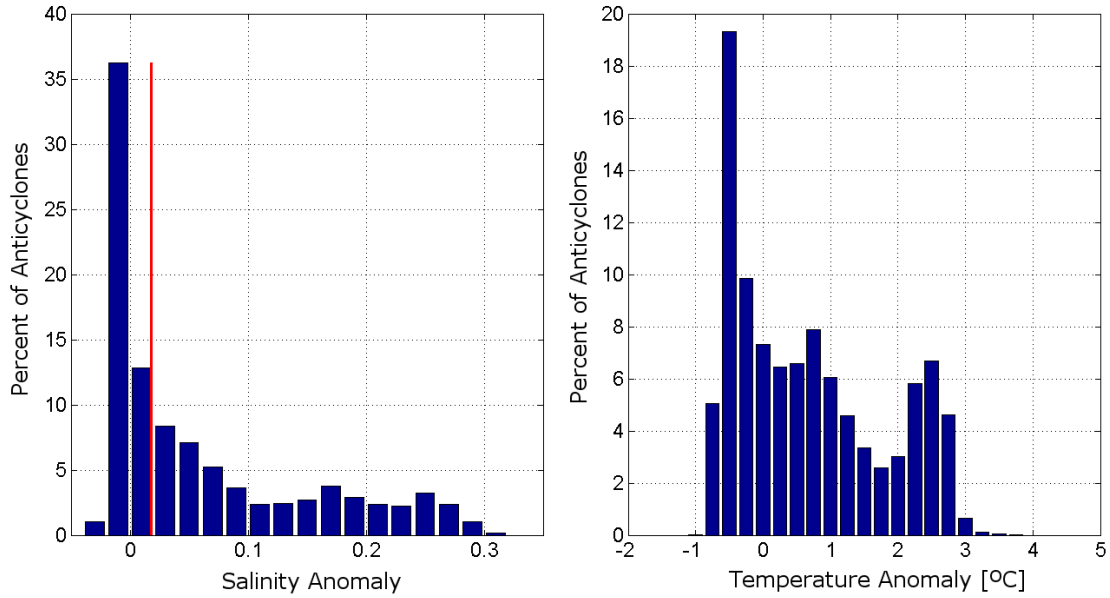

Figure 5.5: Histograms of model salinity and temperature anomalies in CIS basin. Left: Histogram of the percent of anticyclone features at various salinity anomalies. Anomalies represent the average over 200-700m with respect to basin-averaged salinity over same depth range. The red line represents one standard deviation from the mean basin average salinity. Right: Histogram of the percent of model anticyclones with various temperature anomalies. Temperature anomalies are calculated in the same way as the salinity anomalies. The features are found in the model output between 2002 and 2010.

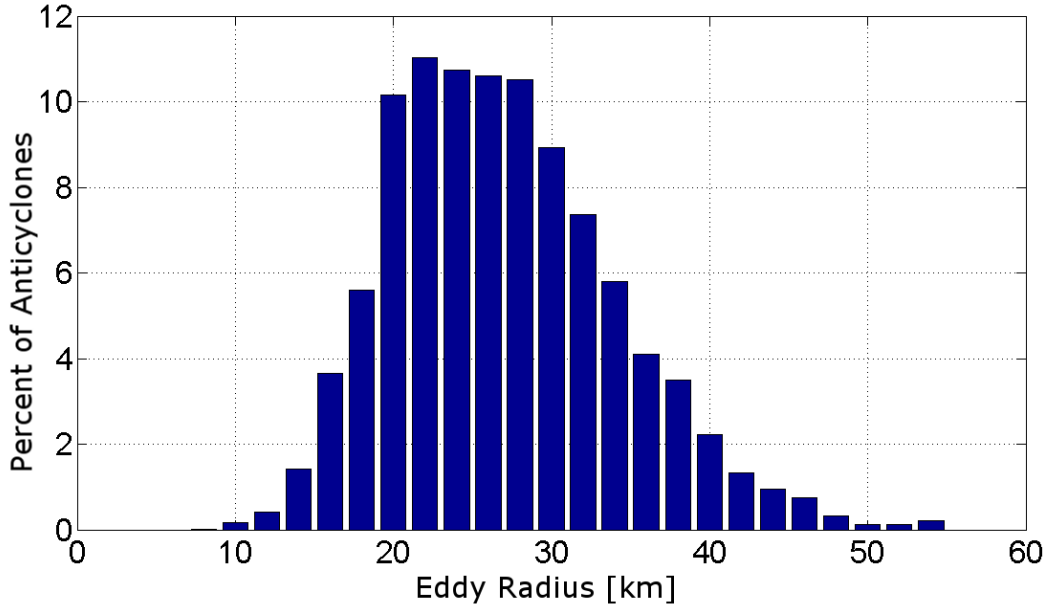

Figure 5.6: Histogram of percent of model eddies having given radii each year (defined as the distance from the estimated eddy center to the maximum velocity magnitude). Shown are anticyclones with positive salinity anomalies only.

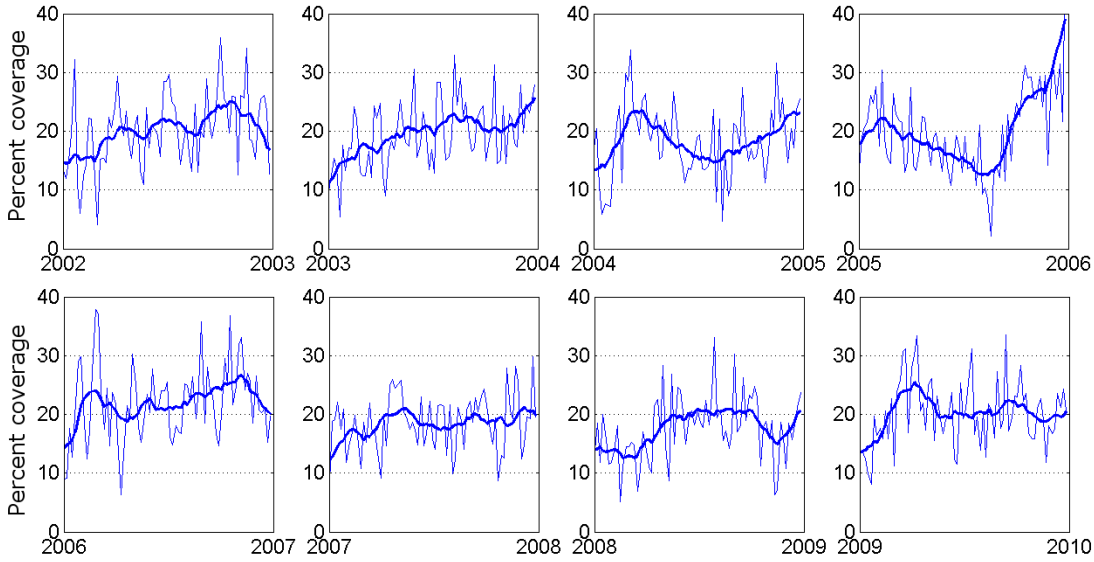

Figure 5.7: Model percent horizontal area coverage by anticyclones. Shown are anticyclones with positive salinity anomalies only.

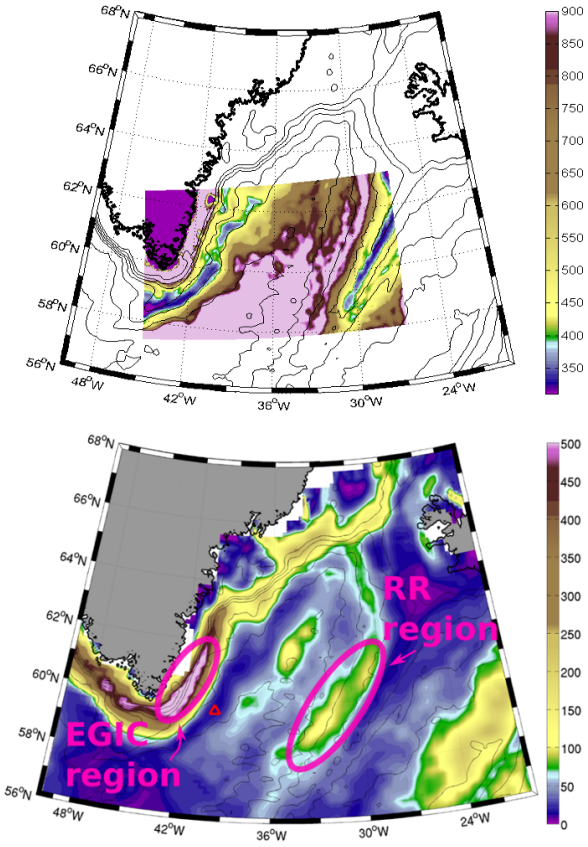

Figure 5.8: Model EKE compared to EKE from satellite altimetry. Top: Model mean surface eddy kinetic energy (EKE, in cm^2s^{-2}) with respect to the 2002-2010 mean velocities from the model. Bottom: reproduction from Fan et al. (2013) showing EKE from satellite altimetry with two proposed formation regions of anticyclones. EKE is calculated from satellite altimetry-derived geostrophic velocity anomaly averaged over 2000-2009, shown in cm^2s^{-2} .

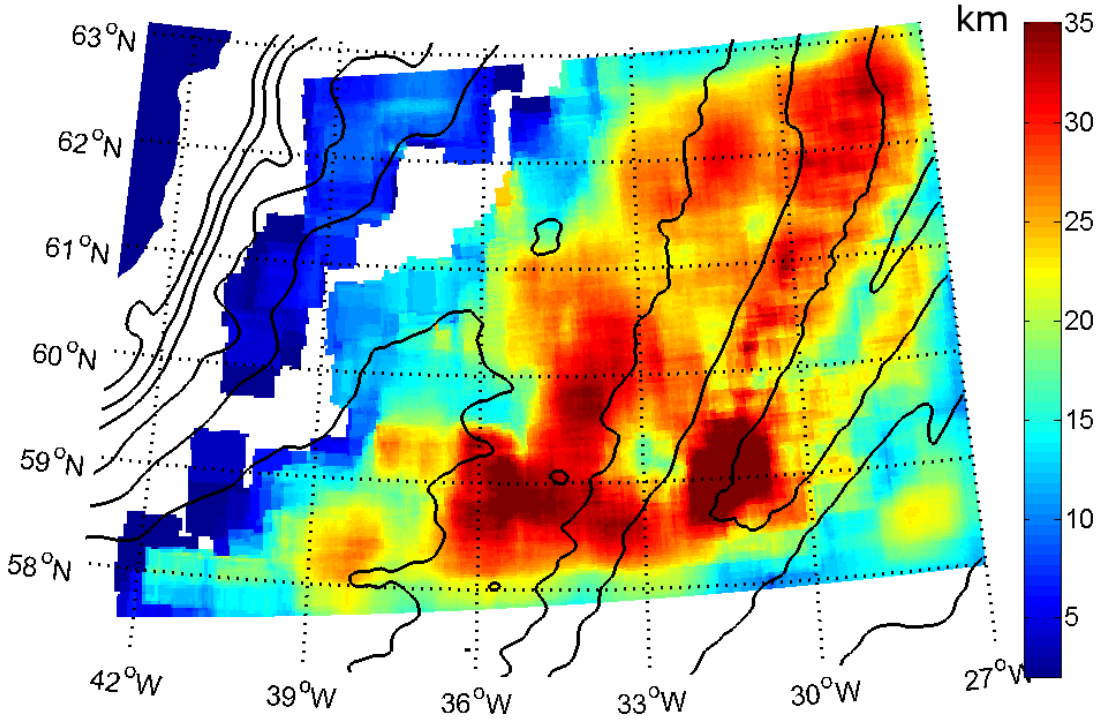

Figure 5.9: Equivalent anticyclone radii of high salinity features found using salinity threshold criteria. The radii are calculated such that the horizontal area coveraged by the high salinity feature is equivalent to a circle with that given radius. Radii values are shown in km.

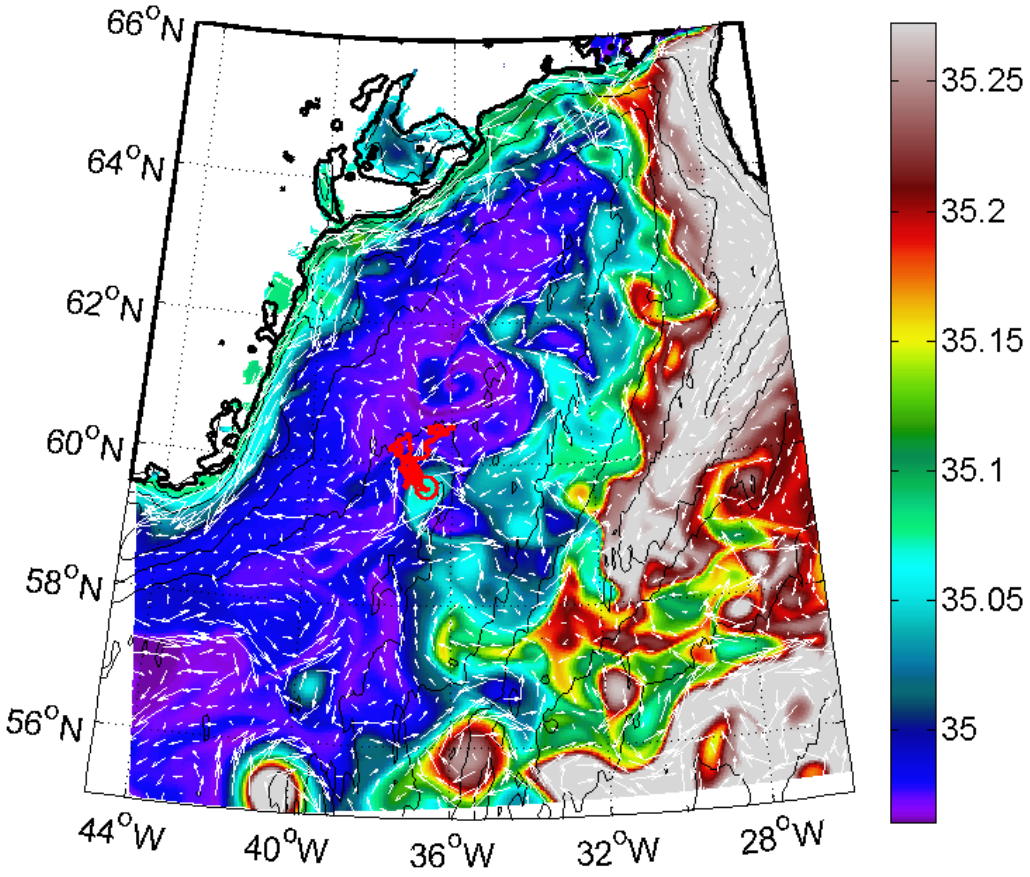

Figure 5.10: Visualization of example eddy tracked in the VIKING20 model. The snapshot shows the 400m salinity field on October 13, 1997. The line red shows the path that the anticyclone takes through its life, from October 1997 to August 1998.

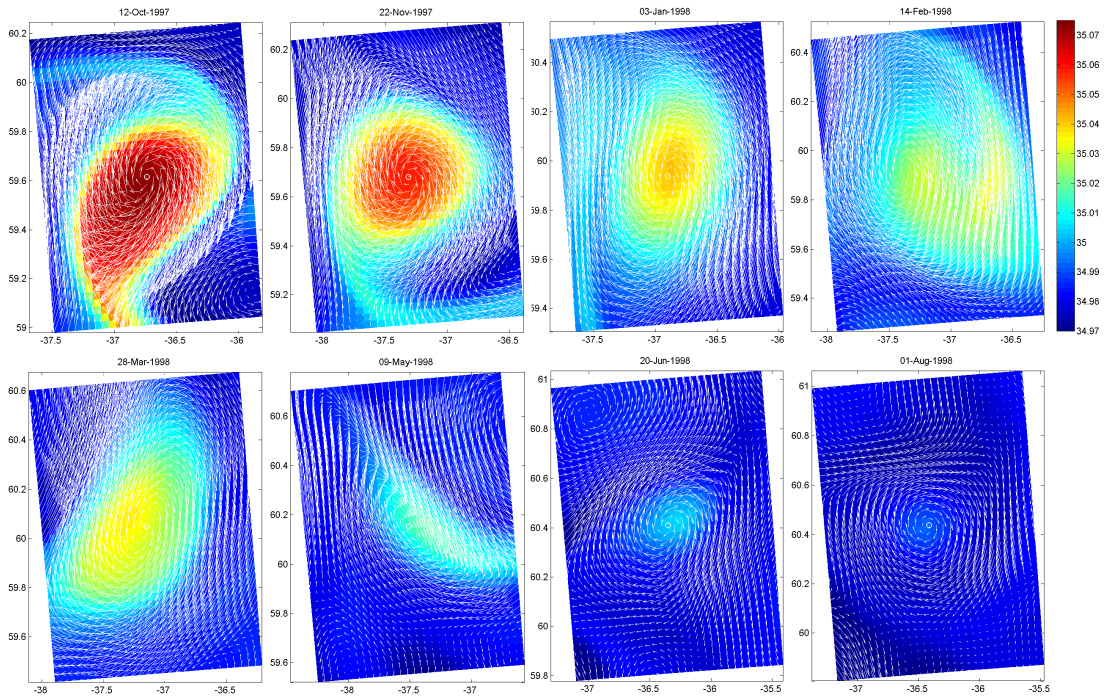

Figure 5.11: Snapshots of the horizontal 400m salinity field at different points in time following the example anticyclone. White vectors show the 400m velocity.

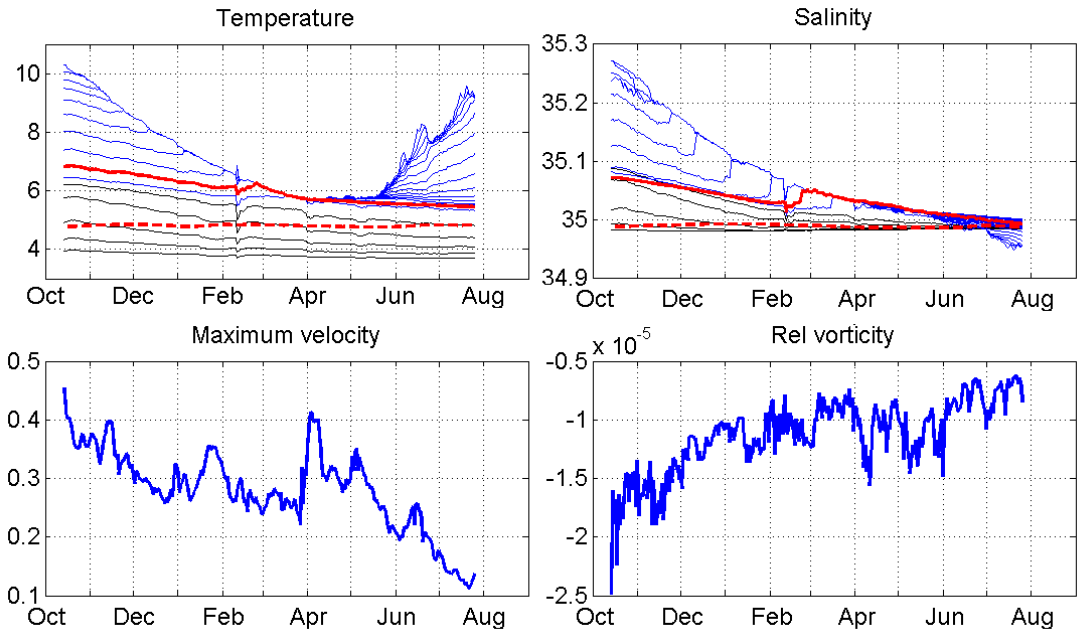

Figure 5.12: Timeseries of temperature, salinity, maximum velocity, and relative vorticity following the center (core) of the tracked anticyclone. Top left: Timeseries of temperature (in $^{\circ}C$) following the example anticyclone at the center of its core at various depths between the surface and 1000m. Top right: Timeseries of salinity following the example anticyclone at the center of its core. For both temperature and salinity plots, the blue lines represent the profiles in the top 400m. The thick red line indicates the 400m property timeseries coinciding with the property fields shown in figure 5.11. Bottom left: Timeseries of maximum velocity (in m/s) following the eddy core. Maximum velocities are found by searching for the maximum in four directions (north, south, east, and west) from the eddy center. Bottom right: Timeseries of relative vorticity (in s^{-1}) following the eddy core. Relative vorticities represent the mean relative vorticity within the eddy core maximum velocity in each of the four directions.

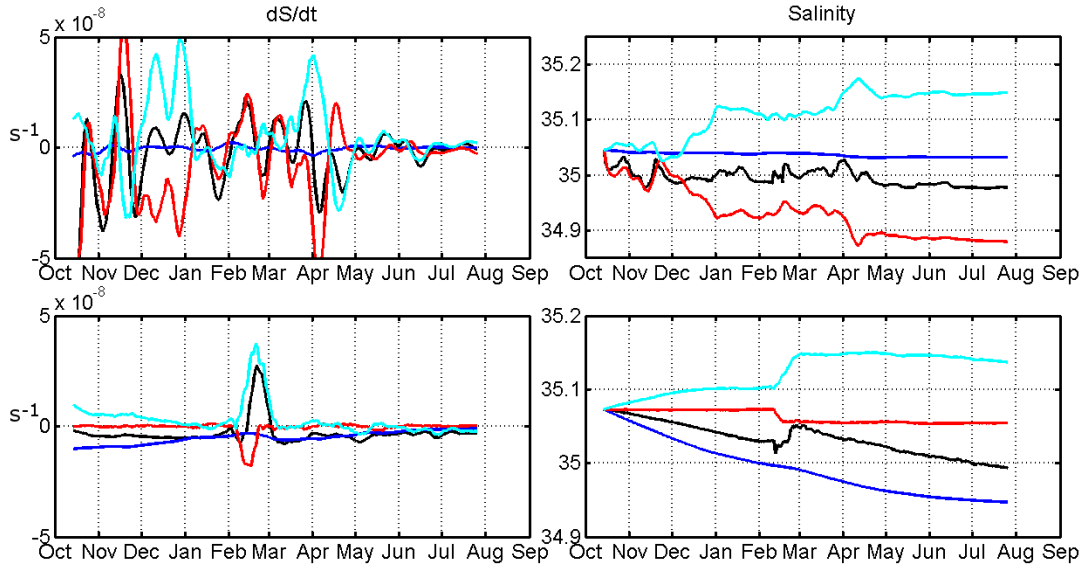

Figure 5.13: Timeseries of horizontal salinity balance terms. Left panels: Timeseries of terms in equation (5.2). These terms are $\frac{\partial S}{\partial t}$ (black), $-K\nabla^2 S$ (blue), $-\vec{v}\nabla S$ (red), and $\frac{\partial S}{\partial t} + K\nabla^2 S + \vec{v}\nabla S$ (cyan). Right panels: Time integrated values of the same terms represented in the left panels with a constant offset such that they start at the same point. The top plots represent the timeseries for a point just outside of the maximum velocity defining the eddy core. The bottom plots show the same timeseries for the center of the eddy.

Chapter 6

Advances Resulting from the Dissertation and Potential Future Work

Studies have shown that anticyclones are an essential contributor to the heat budget (Lilly et al., 2003; Katsman et al., 2004; Hátún et al., 2007; Rykova et al., 2009) and salt budget (Hátún et al., 2007; Schmidt and Send, 2007) in numerous regions of the North Atlantic Ocean. In the Norwegian Sea and the Labrador Sea, eddies have been extensively observed and documented, but an equivalent analysis of eddies in the Irminger Sea did not yet exist. Eddies in the Irminger Sea appear in numerous observations (e.g. Holliday et al., 2007; De Jong, 2010; Daniault et al., 2011; Våge et al., 2011a; De Jong et al., 2012), but only a few studies have quantified their size and examined their properties. Likewise, the potential for the eddies in the Irminger Sea to affect budgets had not been explored. This dissertation serves to fill this gap. We present detailed observations of warm, salty anticyclones in the Irminger Sea and we quantify their impact on the heat and salt budgets of the gyre (Chapters 2 and 3).

The techniques developed to analyze eddies from a single mooring provided a new way to objectively estimate the actual eddy size, which adds to previously developed techniques (Lilly and Rhines, 2002; Lilly et al., 2003). Anticyclones were found to originate from two different formation regions along the Irminger Current. The CIS mooring primarily observed small anticyclones presumably originating from the west-

ern source which was closest to the mooring. Curiously, no larger anticyclones from the eastern source were encountered. Thus, it is difficult to draw conclusions about the larger anticyclones from the mooring data alone. Satellite altimetry and Argo float profiles have shown that the larger anticyclones do indeed exist. As with most observational studies in the ocean, more observations would greatly improve the budget estimates. It will be interesting to examine the variability of anticyclone properties as we obtain more data from the CIS mooring in the coming years. Over the time period of 2002 to 2009, the eddy input of heat and salt to the basin remained relatively steady despite some year-to-year variability in eddy numbers and properties. The question of whether their contribution remains consistent over much longer time scales still remains, and estimates will improve with more observations in the coming years. The CIS mooring is currently still operational, so the same analyses could be applied to this longer record and results can be tested with data until present. With the most recent CIS mooring data, the observed temperature and salinity trends and the anticyclone transport variability described in Chapter 3 can be verified and put into the context of observed trends in water mass properties and wintertime deep convection described in numerous studies (e.g. Pickart et al., 2003; Bacon et al., 2003; Våge et al., 2008a).

One possible mechanism for the death of the anticyclones was examined in Chapter 4. We have shown that during a period of surface heat loss, the barotropic component of an anticyclone can be reduced such that the vortex flow can change from co-rotational to counter-rotational. Simulation studies using very simplified vortices 2- and 3-layer vortices show that the growth of unstable modes increases by one order of magnitude when entering the counter-rotating state. However, a 4-layer simulation with parameters fit to an observed anticyclone in Katsman et al. (2003) did not show an obvious preference for stability in the co-rotating regime. The eddy used in this simulation had larger radii and core property anomalies, and had layer deflections about 4 times larger than the anticyclones we observed in the Irminger Sea. It is suggested in Katsman et al. (2003) that the results are indeed sensitive to the choice of parameters in the simulation, and performing the stability analysis using parameters from our observed anticyclones would be an important next step to determining under what flow regimes our anticyclones can enter an unstable state. It would be enlightening to develop a full

process model to reproduce the eddies and their behaviour under cooling.

If the non-linear response in dynamic height change during surface forcing is enough to change the structure of flow in anticyclones, one might expect this effect to also be present in other features, like cold core cyclones, for example. Studies have suggested that cyclones with doming isopycnals can create a region of locally deeper mixing due to their low stratification in their core. It would be a useful next step to examine the responses of the rotational structure after winter heat loss as well as spring restratification. An interesting question which remains is whether the non-linear density effects are a ubiquitous process driving changes in stability in all vortices. We have examined only one possible mechanism for anticyclone decay, and other mechanisms need to be studied to determine their contributions to eddy dissipation. These mechanisms include interactions with a boundary current (Brown et al., 1986) and topography (Kamenkovich et al., 1996; Schonten et al., 2000), eddy propagation pathways (Gordon and Haxby, 1990; Schonten et al., 2000), interactions with the surface wind stress field (e.g. Chelton et al., 2001; Hashizume et al., 2001; Polito et al., 2001; ONeill et al., 2003; Chelton et al., 2004), and the effects of diapycnal mixing triggered by internal waves (Kunze, 1985; Kunze et al., 1995). It is possible that the processes described above all contribute to some extent to the stability and eventual decay of the anticyclones in the Irminger Sea. Further studies are needed to examine these processes individually and how they contribute to the decay of the anticyclones we have examined.

The VIKING20 high-resolution output was used to examine how well such an eddy-resolving model could reproduce eddies and general properties of the Irminger basin. The model successfully reproduced many features, including seasonal mixed layer depths and overall shape of currents and basin-scale gradients. Although temperatures throughout the water column were reproduced realistically, the model consistently reported higher salinity values than our observations. The model reproduced many warm, salty anticyclones which qualitatively looked and behaved similarly to observations, but the temperature and salinity anomalies within the cores of these features was often one order of magnitude larger than the observations. Model eddies appeared much more energetic than observed eddies, having rotational velocities often one order of magnitude larger as well. The model produced a horizontal area covered by the an-

ticyclones very similar to our observations, suggesting that the eddy field (in terms of size and number of eddies) is realistic. One might suggest that since these parameters are reproduced, eddy transports calculated from the model output can be realistic. However, because the eddy core temperature and salinity anomalies are much higher than observations, eddy input of heat and salt would yield much larger values than what we have estimated in Chapter 3. The next logical step using the model output is to quantify the heat and salt budget terms in the Irminger basin, and compare those values to our estimates from observations.

We had observed a consistent seasonal cycle in anticyclone occurrences, but the VIKING20 model was unable to reproduce this variability. Upon tracking one eddy through winter mixing and restratification, a steady decrease in property anomalies and velocity was observed. The effect of the model diffusivity on salinity (treated as a tracer) and viscosity on the vorticity field proved to be the driving factors in the model eddy decay. If the model is destroying individual vortices on the time scales on its prescribed diffusive and viscous time scales, we may not expect to see a clear seasonal cycle because individual eddies will be at different stages of decay at different times. This makes it difficult for us to test the hypothesis of decay described in Chapter 4. It is useful to know that although many features of the model eddy field are similar to observations, the diffusivity and viscosity in this particular simulation were large enough to control the eddy's decay, and thus does not capture the actual physical processes governing the eddy's death. This is useful for future high resolution model simulations that attempt to resolve individual eddies.

Observations of eddies are increasing in every part of the ocean with the improvement of different data platforms and analyses. The anticyclones examined in this dissertation have been shown to be a ubiquitous feature throughout many basins in the North Atlantic, and similar features exist throughout the world's oceans. The anticyclones in the Irminger Sea are important in controlling the heat and salt budget locally, which can have impacts on the properties and variability of properties of the gyre, the stratification, and even the possibility for deep convection to exist. They make an important contribution to the exchange of water between the boundary current and the interior gyre, and this likely extends to other ocean basins, where eddies have been observed

breaking off of most large ocean boundary currents. The extent to which the eddies have an effect on water masses depends heavily on how they move as a coherent structure. It is therefore important to understand the processes governing eddy formation and decay. We have examined only a small portion of the dynamics and processes experienced by these eddies, and envision that greater understanding of the governing physical processes and the ultimate effects eddies have on ocean basins will come as we discover the important role they play in the ocean.

Appendix A

Determining Argo float eddies using local threshold

We want to determine if an Argo float profile is within an anticyclone by applying a salinity threshold, and then obtain a basin-wide eddy census. First, profiles taken in independent eddies must be found to eliminate bias from floats trapped in float eddies. The average (quasi-Lagrangian) decorrelation scale for temperature and salinity at 260 m (a typical eddy core depth) estimated from over 50 floats that entered the Irminger Sea is 50 days. This means that on average, float profiles (from the same float) greater than 50 days apart will be uncorrelated and not be part of the same feature.

We want to define a salinity threshold beyond which a float profile is in an anticyclone. A salinity gradient is observed across the Irminger Sea from previous observations (see Våge et al., 2011a), so applying one threshold to all floats would be inappropriate. Instead, we need thresholds dependent on a given region. We obtain the background salinity field from the World Ocean Atlas 2009 (WOA09) product. WOA09 is a set of objectively analyzed (1° grid) climatological fields of in situ measurements at standard depth levels for annual, seasonal, and monthly compositing periods for the world ocean. Here, we have used the mean salinity product, whose details are found in Antonov et al. (2010). The WOA09 mean salinity field at 260m, as expected, shows higher salinities in the north-east region of the Irminger Sea and lower salinities in the southwest. We compare the WOA09 salinity in the Irminger Sea with mean uncorrelated Argo float salinities averaged over 100 km by 100 km bins over the basin.

First, we compare statistics for an area 100 km around the CIS mooring, assuming that the mooring statistics are representative of this region. At the WOA09 nearest grid point, the mean salinity at 260m is 0.02 lower than the mean non-eddy salinity at the mooring. This is expected since we know the mooring sampled during a time of increased salinities (Sarafanov et al., 2007) compared to climatology. The Argo float mean at 260m in this region is 0.02 higher than the mooring non-eddy mean; this is due to the floats' sampling both eddies and non-eddy water. The salinity threshold is defined as the mean plus one standard deviation (STD). The STD used for the WOA threshold is the mooring STD, which represents the variability in salinities in the region. The STDs used for the WOA and Argo floats are 0.02 and 0.04. These values resulted in a WOA threshold of 34.94, and an Argo float threshold of 34.96. Because the WOA threshold is likely biased low, and the Argo float threshold is biased high, we take the mean of the two to be our threshold to find eddies.

Using this threshold, 22% of uncorrelated float profiles within 100 km of the mooring are eddies. We assume that the percent of time the mooring timeseries is occupied by an eddy is equivalent to the percent of float profiles that happen to sample in an eddy. This essentially means that the probabilities of picking a point within an eddy are the same if one randomly picks a point in time or a point in space. The mooring shows about 18% of the timeseries is occupied by high salinity associated with anticyclones. This is similar to the percent of float profiles picked by the theshold method in this region, suggesting that the threshold method is valid. We extend this method to the entire basin by making 100 km by 100 km bins and picking float eddies from local salinity thresholds at 260m in each bin.

NCEP re-calculation of sensible and latent heat

Previous studies (see Josey, 2001; Smith et al., 2001; Renfrew et al., 2002) have shown significant biases in the NCEP heat fluxes compared to heat flux observations. The primary sources of the biases come from the calculation of the sensible and latent

heat fluxes. In the Labrador Sea, Josey (2001) observed that the NCEP product overestimates the net heat flux by a mean bias of $35 \pm 12\ W/m^2$.

In order to correct for the bias, we employ the bulk formula methods outlined by Smith (1988) and DeCosmo et al. (1996). These formulas have been shown to be an effective alternative to the bulk formulations used by NCEP to eliminate the bias (see Bumke et al., 2002). In order to use these bulk formulas, we use the following output variables provided by the NCEP dataset: 10m wind, air temperature, air density, specific humidity, and ocean skin temperature. The mean values of these variables over the Labrador Sea area are used in the calculations. With these, we calculate the sensible and latent heat flux coefficients using the bulk formulas in Smith (1988) and DeCosmo et al. (1996), respectively. We then obtain a second order regression between the NCEP net heat flux and the recalculated net heat flux of the form:

$$Q_{re} = -0.0003Q_{ncep}^2 + 0.8785Q_{ncep} - 10.7170 \tag{A.1}$$

where Q_{ncep} and Q_{re} represent the NCEP and recalculated net heat fluxes, respectively.

The resulting Q_{re} value has a mean offset of -39 W/m^2 over the Labrador Sea compared to the original NCEP net heat flux. This value is very close to the observed bias reported in Josey (2001), suggesting that the new bulk formulations for the sensible and latent heat fluxes are more representative for the Labrador Sea region. Assuming that the same applies for the CIS basin, we apply the regression to the NCEP net heat flux at the CIS mooring location. The resulting new heat flux has a mean offset of -23 W/m^2 from the original NCEP value. This recalculated heat flux is used in our analysis. Computed in units corresponding to what is shown in table 3.1, an offset of -23 W/m^2 is equivalent to $56\text{x}10^{-7}\ ^oCm/s$, a very large offset compared to the terms in the heat budget.

Derivation of heat conservation equation

We follow the formulation presented by Stevenson and Niiler (1983) and Moisan and Niiler (1998). The 3D heat equation vertically integrated down to an isotherm (or constant depth, in our case) of depth h is described as

$$h\frac{\partial T_a}{\partial t} + h\mathbf{v}_a \cdot \nabla T + \nabla \cdot \left(\int_{-h}^{0} \hat{\mathbf{v}} \hat{T}_a dz \right) + (T_a - T_{-h}) \times \left(\frac{\partial h}{\partial t} + v_{-h} \cdot h + w_{-h} \right) = \frac{q_o - q_{-h}}{\rho_o c_p}, \tag{A.2}$$

where ρ_o, c_p, and T_a are the mean density, specific heat, and temperature of seawater, respectively, and q_o and q_{-h} are the vertical heat flux through the top and bottom of a layer bound by the surface and depth of isotherm (or isopycnal) h. The vertically averaged horizontal velocity is separated into $\mathbf{v} = \mathbf{v}_a + \hat{\mathbf{v}}$, and the vertically averaged temperature is separated similarly ($T = T_a + \hat{T}$).

Following the logic of Stevenson and Niiler (1983), since h is almost always below the main thermocline, the flux of heat through the bottom, q_{-h}, is negligible. Because h essentially acts as a material surface, the entrainment rate of heat across the interface is small and the term $(\frac{\partial h}{\partial t} + v_{-h} \cdot h + w_{-h})$ is small. The horizontal eddy heat transport term is also neglected because it represents eddies with vertical temperature anomalies not represented by the mean. Because we have observed eddies primarily with a barotropic signal (at least in the upper ISW layer) from Fan et al. 2013, this term is likely small. The final equation, as in Moisan and Niiler (1998), contains the heat storage rate term, a horizontal heat advection term, and a net surface heat flux term:

$$\rho_o c_p \left(h\frac{\partial T_a}{\partial t} + h\mathbf{v}_a \cdot \nabla T_a \right) = Q_{net}, \tag{A.3}$$

where $Q_{net} = q_o$ is the net heat flux across the ocean surface, and we have $h = H$ held at a constant depth.

Next, because we want to examine the heat budget (and salt budget) in terms of means over a certain time period, we decompose the temperature following the triple decomposition presented in Reynolds and Hussain (1972):

$$T_a = \overline{T}_a + \widetilde{T}_a + T_a' \tag{A.4}$$

$\overline{T}_a$ is the mean (time-averaged) contribution, $\widetilde{T}_a$ is the large-scale organized fluctuation, and T_a' is the part of the signal not covered by $\overline{T}_a$ and $\widetilde{T}_a$. In our case, the $\widetilde{T}_a$ represents the

specific contribution by the anticyclonic eddies, and T_a' comprises all other contributions from different phenomena or time scales (e.g. cyclones, advection on scales other than eddy scales, random turbulence). Likewise, the velocity is decomposed as

$$\mathbf{v}_a = \overline{\mathbf{v}}_a + \widetilde{\mathbf{v}}_a + \mathbf{v}_a'. \tag{A.5}$$

The *phase average* (designated by $\langle\rangle$) is defined in Reynolds and Hussain (1972) to be the average over a large ensemble of points having the same phase for a given phenomenon. Because we are identifying our anticyclone features discretely, we are essentially performing a phase average over the observations to isolate them, effectively rejecting other phenomena or scales of variability. We substitute the decomposed variables and take the phase average of equation (A.3) to arrive at

$$\begin{aligned}\left\langle H\frac{\partial \overline{T}_a}{\partial t}\right\rangle + \left\langle H\frac{\partial \widetilde{T}_a}{\partial t}\right\rangle + \left\langle H\frac{\partial T_a'}{\partial t}\right\rangle + \left\langle H\overline{\mathbf{v}}_a\cdot\nabla\overline{T}_a\right\rangle + \left\langle H\overline{\mathbf{v}}_a\cdot\nabla\widetilde{T}_a\right\rangle + \left\langle H\overline{\mathbf{v}}_a\cdot\nabla T_a'\right\rangle \\ + \left\langle H\widetilde{\mathbf{v}}_a\cdot\nabla\overline{T}_a\right\rangle + \left\langle H\widetilde{\mathbf{v}}_a\cdot\nabla\widetilde{T}_a\right\rangle + \left\langle H\widetilde{\mathbf{v}}_a\cdot\nabla T_a'\right\rangle \\ + \left\langle H\mathbf{v}'_a\cdot\nabla\overline{T}_a\right\rangle + \left\langle H\mathbf{v}'_a\cdot\nabla\widetilde{T}_a\right\rangle + \left\langle H\mathbf{v}'_a\cdot\nabla T_a'\right\rangle \\ = \left\langle\frac{Q_{net}}{\rho_o c_p}\right\rangle\end{aligned}$$

Using rules of Reynolds averaging, we can rewrite this as

$$\begin{aligned}H\frac{\partial\left\langle\overline{T}_a\right\rangle}{\partial t} + H\frac{\partial\left\langle\widetilde{T}_a\right\rangle}{\partial t} + H\frac{\partial\left\langle T_a'\right\rangle}{\partial t} + H\overline{\mathbf{v}}_a\cdot\nabla\left\langle\overline{T}_a\right\rangle + H\overline{\mathbf{v}}_a\cdot\nabla\left\langle\widetilde{T}_a\right\rangle + H\overline{\mathbf{v}}_a\cdot\nabla\left\langle T_a'\right\rangle \\ + H\widetilde{\mathbf{v}}_a\cdot\nabla\left\langle\overline{T}_a\right\rangle + H\widetilde{\mathbf{v}}_a\cdot\nabla\left\langle\widetilde{T}_a\right\rangle + H\widetilde{\mathbf{v}}_a\cdot\nabla\left\langle T_a'\right\rangle \\ + H\left\langle\mathbf{v}'_a\right\rangle\cdot\nabla\overline{T}_a + H\left\langle\mathbf{v}'_a\right\rangle\cdot\nabla\widetilde{T}_a + H\left\langle\mathbf{v}'_a\cdot\nabla T_a'\right\rangle \\ = \left\langle\frac{Q_{net}}{\rho_o c_p}\right\rangle\end{aligned}$$

$$\begin{aligned}H\frac{\partial\overline{T}_a}{\partial t} + H\frac{\partial\widetilde{T}_a}{\partial t} + H\frac{\partial\left\langle T_a'\right\rangle}{\partial t} + H\overline{\mathbf{v}}_a\cdot\nabla\overline{T}_a + H\overline{\mathbf{v}}_a\cdot\nabla\widetilde{T}_a + H\overline{\mathbf{v}}_a\cdot\nabla\left\langle T_a'\right\rangle \\ + H\widetilde{\mathbf{v}}_a\cdot\nabla\overline{T}_a + H\widetilde{\mathbf{v}}_a\cdot\nabla\widetilde{T}_a + H\widetilde{\mathbf{v}}_a\cdot\nabla\left\langle T_a'\right\rangle \\ + H\left\langle\mathbf{v}'_a\right\rangle\cdot\nabla\overline{T}_a + H\left\langle\mathbf{v}'_a\right\rangle\cdot\nabla\widetilde{T}_a + H\left\langle\mathbf{v}'_a\cdot\nabla T_a'\right\rangle \\ = \left\langle\frac{Q_{net}}{\rho_o c_p}\right\rangle\end{aligned}$$

By definition, $\langle \mathbf{v}'_a \rangle = \langle T'_a \rangle = 0$, so we have

$$H\frac{\partial \overline{T}_a}{\partial t} + H\frac{\partial \widetilde{T}_a}{\partial t} + H\overline{\mathbf{v}}_a \cdot \nabla \overline{T}_a + H\overline{\mathbf{v}}_a \cdot \nabla \widetilde{T}_a + H\widetilde{\mathbf{v}}_a \cdot \nabla \overline{T}_a + H\widetilde{\mathbf{v}}_a \cdot \nabla \widetilde{T}_a + H\left\langle \mathbf{v}'_a \cdot \nabla T'_a \right\rangle = \left\langle \frac{Q_{net}}{\rho_o c_p} \right\rangle$$

Taking the time-average (overbar operator) over the entire equation, we arrive at

$$\overline{H\frac{\partial \overline{T}_a}{\partial t}} + \overline{H\frac{\partial \widetilde{T}_a}{\partial t}} + \overline{H\overline{\mathbf{v}}_a \cdot \nabla \overline{T}_a} + \overline{H\overline{\mathbf{v}}_a \cdot \nabla \widetilde{T}_a} + \overline{H\widetilde{\mathbf{v}}_a \cdot \nabla \overline{T}_a} + \overline{H\widetilde{\mathbf{v}}_a \cdot \nabla \widetilde{T}_a} + \overline{H\left\langle \mathbf{v}'_a \cdot \nabla T'_a \right\rangle} = \overline{\left\langle \frac{Q_{net}}{\rho_o c_p} \right\rangle}$$

$$H\frac{\partial \overline{T}_a}{\partial t} + H\frac{\partial \overline{\widetilde{T}}_a}{\partial t} + \overline{H\overline{\mathbf{v}}_a \cdot \nabla \overline{T}_a} + H\overline{\mathbf{v}}_a \cdot \nabla \overline{\widetilde{T}}_a + H\overline{\widetilde{\mathbf{v}}}_a \cdot \nabla \overline{T}_a + \overline{H\widetilde{\mathbf{v}}_a \cdot \nabla \widetilde{T}_a} + \overline{H\mathbf{v}'_a \cdot \nabla T'_a} = \overline{\frac{Q_{net}}{\rho_o c_p}}$$

By definition, $\overline{\widetilde{T}}_a = \overline{\widetilde{\mathbf{v}}}_a = 0$, and we are left with

$$H\frac{\partial \overline{T}_a}{\partial t} + H\overline{\mathbf{v}}_a \cdot \nabla \overline{T}_a + \overline{H\widetilde{\mathbf{v}}_a \cdot \nabla \widetilde{T}_a} + \overline{H\mathbf{v}'_a \cdot \nabla T'_a} = \overline{\frac{Q_{net}}{\rho_o c_p}}. \tag{A.6}$$

Following the same arguments, using $S_a = \overline{S}_a + \widetilde{S}_a + S'_a$, we arrive at a salt balance equation of the same form:

$$H\frac{\partial \overline{S}_a}{\partial t} + H\overline{\mathbf{v}}_a \cdot \nabla \overline{S}_a + \overline{H\widetilde{\mathbf{v}}_a \cdot \nabla \widetilde{S}_a} + \overline{H\mathbf{v}'_a \cdot \nabla S'_a} = \overline{P - E} \tag{A.7}$$

Bibliography

M.R. Abbott and P.M. Zion. Satellite observations of phytoplankton variability during an upwelling event. *Continental Shelf Research*, 4:661–680, 1985.

J. I. Antonov, D. Seidov, T. P. Boyer, R. A. Locarnini, A. V. Mishonov, and H. E. Garcia. World Ocean Atlas 2009 Volume 2: Salinity. *NOAA Atlas NESDIS 69*, page 184, 2010.

J.I. Antonov, R.A. Locarnini, T.P. Boyer, A.V. Mishonov, and H.E. Garcia. World ocean atlas 2005 volume 2: Salinity. *US Department of Commerce, NOAA, NESDIS, USA*, 62, 2006.

A. Arakawa and V.R. Lamb. Computational design of the basic dynamical processes of the ucla general circulation model. *Methods in computational physics*, 17:173–265, 1977.

B.K. Arbic and G.R. Flierl. Baroclinically unstable geostrophic turbulence in the limits of strong and weak bottom ekman friction: Application to midocean eddies. *Journal of Physical Oceanography*, 34:2257–2273, 2004.

L. Armi, D. Hebert, N. Oakey, J.F. Price, P.L. Richardson, H.T. Rossby, and B. Ruddick. Two years in the life of a Mediterranean salt lens. *Journal of Physical Oceanography*, 19:354–370, 1989.

S. Bacon, W.J. Gould, and Y. Jia. Open-ocean convection in the Irminger Sea. *Geophysical Research Letters*, 30:1246, 2003.

E. Behrens. *The oceanic response to Greenland melting: the effect of increasing model resolution*. PhD thesis, Helmholtz Centre for Ocean Research (GEOMAR), Kiel, September 2013.

E. Behrens, A. Biastoch, and C.W. Böning. Spurious amoc trends in global ocean sea-ice models related to subarctic freshwater forcing. *Ocean Modelling*, 69:39–49, 2013.

M. Bersch, I. Yashayaev, and K.P. Koltermann. Recent changes of the thermohaline circulation in the subpolar north atlantic. *Ocean Dynamics*, 57:223–235, 2007.

A. Biastoch, C.W. Böning, J. Getzlaff, J. Molines, and G. Madec. Causes of interannual-decadal variability in the meridional overturning circulation of the midlatitude north atlantic ocean. *Journal of Climate*, 21:6599–6615, 2008.

J.F. Bjerknes. Atlantic air-sea interaction. *Advances in Geophysics*, 10:82, 1964.

C.W. Böning, M. Scheinert, J. Dengg, A. Biastoch, and A. Funk. Decadal variability of subpolar gyre transport and its reverberation in the north atlantic overturning. *Geophysical Research Letters*, 33, 2006.

A. Bracco, J. Pedlosky, and R.S. Pickart. Eddy formation near the west coast of Greenland. *Journal of Physical Oceanography*, 38:1992–2002, 2008.

F.P. Bretherton and D.B. Haidvogel. Two-dimensional turbulence above topography. *Journal of Fluid Mechanics*, 78:129–154, 1976.

O.B. Brown, P.C. Cornillon, S.R. Emmerson, and H.M. Carle. Gulf stream warm rings: a statistical study of their behavior. *Deep Sea Research*, 33:1459–1473, 1986.

J.G. Bruce. Eddies southwest of the Denmark Strait. *Deep Sea Research Part I: Oceanographic Research Papers*, 42:13–17, 1995.

K. Bumke, U. Karger, and K. Uhlig. Measurements of turbulent fluxes of momentum and sensible heat over the labrador sea. *Journal of Physical Oceanography*, 32:401–410, 2002.

G.F. Carnevale, R.C. Kloosterziel, and G.J.F. Van Heijst. Propagation of barotropic vortices over topography in a rotating tank. *Journal of Fluid Mechanics*, 233:119–139, 1991.

C. Cenedese and PF Linden. Cyclone and anticyclone formation in a rotating stratified fluid over a sloping bottom. *Journal of Fluid Mechanics*, 381:199–223, 1999.

D.B. Chelton, R.A. DeSzoeke, M.G. Schlax, K. El Naggar, and N. Siwertz. Geographical variability of the first baroclinic Rossby radius of deformation. *Journal of Physical Oceanography*, 28:433–460, 1998.

D.B. Chelton, S.K. Esbensen, M.G. Schlax, N. Thum, M.H. Freilich, F.J. Wentz, C.L. Gentemann, M.J. McPhaden, and P.S. Schopf. Observations of coupling between surface wind stress and sea surface temperature in the eastern tropical pacific. *Journal of Climate*, 14:1479–1498, 2001.

D.B. Chelton, M.G. Schlax, M.H. Freilich, and R.F. Milliff. Satellite measurements reveal persistent small-scale features in ocean winds. *Science*, 303:978–983, 2004.

D.B. Chelton, M.G. Schlax, R.M. Samelson, and R.A. de Szoeke. Global observations of large oceanic eddies. *Geophysical Research Letters*, 34:L15606, 2007.

D.B. Chelton, M.G. Schlax, and R.M. Samelson. Global observations of nonlinear mesoscale eddies. *Progress in Oceanography*, 91:167–216, 2011.

N. Daniault, P. Lherminier, and H. Mercier. Circulation and transport at the south east tip of Greenland. *Journal of Physical Oceanography*, 41:437–457, 2011.

F. De Jong. *Hydrographic Variability of the Irminger Sea*. PhD thesis, University of Utrecht, the Netherlands, 2010.

M.F. De Jong, H.M. van Aken, K. Våge, and R.S. Pickart. Convective mixing in the central Irminger Sea: 2002–2010. *Deep Sea Research Part I: Oceanographic Research Papers*, 63:36–51, 2012.

J. DeCosmo, K.B. Katsaros, S.D. Smith, R.J. Anderson, W.A. Oost, K. Bumke, and H. Chadwick. Air-sea exchange of water vapor and sensible heat: The humidity exchange over the sea (hexos) results. *Journal of Geophysical Research*, 101:12001–12, 1996.

D.P. Dee, S.M. Uppala, A.J. Simmons, P. Berrisford, P. Poli, S. Kobayashi, U. Andrae, M.A. Balmaseda, G. Balsamo, P. Bauer, P. Bechtold, A.C.M. Beljaars, L. Van de Berg, J. Bidlot, N. Bormann, C. Delsol, R. Dragani, M. Fuentes, A.J. Geer, L. Haimberger, S.B. Healy, H. Hersbach, E.V. Holm, L. Isaksen, P. Kallberg, M. Kohler, M. Matricardi, A.P. McNally, B.M. Monge-Sanz, J.-J. Morcrette, B.-K. Park, C. Peubey, P. De Rosnay, C. Tavolato, J.-N. Thepaut, and F. Vitart. The era-interim reanalysis: Configuration and performance of the data assimilation system. *Quarterly Journal of the Royal Meteorological Society*, 137:553–597, 2011.

W.K. Dewar and P.D. Killworth. On the stability of oceanic rings. *Journal of Physical Oceanography*, 25:1467–1487, 1995.

W.K. Dewar, P.D. Killworth, and J.R. Blundell. Primitive-equation instability of wide oceanic rings. part ii: Numerical studies of ring stability. *Journal of Physical Oceanography*, 29:1744–1758, 1999.

B. Dickson, I. Yashayaev, J. Meincke, B. Turrell, S. Dye, and J. Holfort. Rapid freshening of the deep north atlantic ocean over the past four decades. *Nature*, 416:832–837, 2002.

R. Dickson, B. Rudels, S. Dye, M. Karcher, J. Meincke, and I. Yashayaev. Current estimates of freshwater flux through arctic and subarctic seas. *Progress in Oceanography*, 73:210–230, 2007.

R.R. Dickson and J. Brown. The production of north atlantic deep water: sources, rates, and pathways. *Journal of Geophysical Research*, 99:12319–12, 1994.

N. Ducet, PY Le Traon, and G. Reverdin. Global high-resolution mapping of ocean circulation from TOPEX/Poseidon and ERS-1 and-2. *Journal of Geophysical Research (Oceans)*, 105:19–477, 2000.

C. Eden and C. Böning. Sources of eddy kinetic energy in the Labrador Sea. *Journal of Physical Oceanography*, 32:3346–3363, 2002.

W.J. Emery, W.G. Lee, and L. Magaard. Geographic and seasonal distributions of Brunt-Väisälä frequency and Rossby radii in the North Pacific and North Atlantic. *Journal of Physical Oceanography*, 14:294–317, 1984.

A. Falina, A. Sarafanov, and A. Sokov. Variability and renewal of Labrador Sea Water in the Irminger Basin in 1991–2004. *Journal of Geophysical Research*, 112, 2007.

X. Fan, U. Send, P. Testor, J. Karstensen, and P. Lherminier. Observations of irminger sea anticyclonic eddies. *Journal of Physical Oceanography*, 43:805–823, 2013.

J.C. Gascard and K.A. Mork. Climatic importance of large-scale and mesoscale circulation in the Lofoten Basin deduced from lagrangian observations. *Arctic-Subarctic Ocean Fluxes*, pages 131–143, 2008.

R. Gelderloos, C.A. Katsman, and S.S. Drijfhout. Assessing the roles of three eddy types in restratifying the labrador sea after deep convection. *Journal of Physical Oceanography*, 41:2102–2119, 2011.

P.R. Gent, J. Willebrand, T.J. McDougall, and J.C. McWilliams. Parameterizing eddy-induced tracer transports in ocean circulation models. *Journal of Physical Oceanography*, 25:463–474, 1995.

A.E. Gill. *Atmosphere-ocean dynamics*, volume 30. Academic press, 1982.

A.E. Gill, J.S.A. Green, and A.J. Simmons. Energy partition in the large-scale ocean circulation and the production of mid-ocean eddies. In *Deep Sea Research and Oceanographic Abstracts*, volume 21, pages 499–528, 1974.

A.L. Gordon and W.F. Haxby. Agulhas eddies invade the south atlantic: Evidence from geosat altimeter and shipboard conductivity-temperature-depth survey. *Journal of Geophysical Research*, 95:3117–3125, 1990.

C. Gourcuff, P. Lherminier, H. Mercier, and P.Y. Le Traon. Altimetry combined with hydrography for ocean transport estimation. *Journal of Atmospheric and Oceanic Technology*, 28:1324–1337, 2011.

S.M. Griffies, A. Biastoch, C. Böning, F. Bryan, G. Danabasoglu, E.P. Chassignet, M.H. England, R. Gerdes, H. Haak, R.W. Hallberg, W. Hazeleger, J. Jungclaus, W.G. Large, G. Madec, A. Pirani, B. Samuels, M. Scheinert, A.S. Gupta, C.A. Severijns, H.L. Simmons, A.M. Treguier, M. Winton, S. Yeager, and J. Yin. Coordinated ocean-ice reference experiments (cores). *Ocean Modelling*, 26:1–46, 2009.

MEDOC Group. Observation of formation of deep water in the Mediterranean Sea, 1969. *Nature*, 227:1037–1040, 1970.

D.V. Hansen and A. Herman. Temporal sampling requirements for surface drifting buoys in the tropical Pacific. *Journal of Atmospheric and Oceanic Technology*, 6: 599–607, 1989.

D.V. Hansen and P.M. Poulain. Quality control and interpolations of WOCE-TOGA drifter data. *Journal of Atmospheric and Oceanic Technology*, 13:900–910, 1996.

H. Hashizume, S. Xie, W.T. Liu, and K. Takeuchi. Local and remote atmospheric response to tropical instability waves: A global view from space. *Journal of Geophysical Research*, 106:10173–10185, 2001.

H. Hátún, C.C. Eriksen, P.B. Rhines, and J. Lilly. Buoyant eddies entering the Labrador Sea observed with gliders and altimetry. *Journal of Physical Oceanography*, 37: 2838–2854, 2007.

D. Hebert, N. Oakey, and B. Ruddick. Evolution of a Mediterranean salt lens: Scalar properties. *Journal of Physical Oceanography*, 20:1468–1483, 1990.

N.P. Holliday, A. Meyer, S. Bacon, S. Alderson, and B. de Cuevas. The retroflection of part of the East Greenland Current at Cape Farewell. *Geophysical Research Letters*, 34:L07609, 2007.

N.P. Holliday, S.L. Hughes, S. Bacon, A. Beszczynska-Möller, B. Hansen, A. Lavin, H. Loeng, K.A. Mork, S. Østerhus, T. Sherwin, and W. Walczowski. Reversal of the 1960s to 1990s freshening trend in the northeast North Atlantic and Nordic Seas. *Geophysical Research Letters*, 35:L03614, 2008.

S. Hosoda, T. Ohira, and T. Nakamura. A monthly mean dataset of global oceanic temperature and salinity derived from argo float observations. *JAMSTEC Report of Research and Development*, 8:47–59, 2008.

R.X. Huang. *Ocean circulation: wind-driven and thermohaline processes*. Cambridge University Press, 2010.

H.E. Huppert and K. Bryan. Topographically generated eddies. *Deep-Sea Research*, 23: 655–679, 1976a.

H.E. Huppert and K. Bryan. Topographically generated eddies. In *Deep Sea Research and Oceanographic Abstracts*, volume 23, pages 655–679. Elsevier, 1976b.

S.A. Josey. A comparison of ecmwf, ncep-ncar, and soc surface heat fluxes with moored buoy measurements in the subduction region of the northeast atlantic. *Journal of Climate*, 14:1780–1789, 2001.

E. Kalnay, M. Kanamitsu, R. Kistler, W. Collins, D. Deaven, L. Gandin, M. Iredell, S. Saha, G. White, J. Woollen, Y. Zhu, M. Chelliah, W. Ebisuzaki, W. Huggins, J Janowiak, K.C. Mo, C. Ropelewski, J. Wang, A. Leetmaa, R. Reynolds, R. Jenne, and D. Joseph. The NCEP/NCAR 40-year reanalysis project. *Bulletin of the American Meteorological Society*, 77:437–471, 1996.

V.M. Kamenkovich, Y.P. Leonov, D.A. Nechaev, D.A. Byrne, and A.L. Gordon. On the influence of bottom topography on the agulhas eddy. *Journal of Physical Oceanography*, 26:892–912, 1996.

J. Karstensen. Calibration of Physical Data. *Internal Report: Animate Report*, page 43, 2005.

C.A. Katsman, P.C.F. Van der Vaart, H.A. Dijkstra, and W.P.M. De Ruijter. Stability of multilayer ocean vortices: a parameter study including realistic gulf stream and agulhas rings. *Journal of Physical Oceanography*, 33:1197–1218, 2003.

C.A. Katsman, M.A. Spall, and R.S. Pickart. Boundary Current eddies and their role in the restratification of the Labrador sea. *Journal of Physical Oceanography*, 34: 1967–1983, 2004.

A. Köhl. Generation and stability of a quasi-permanent vortex in the Lofoten Basin. *Journal of Physical Oceanography*, 37:2637–2651, 2007.

W. Krauss. Currents and mixing in the Irminger Sea and in the Iceland Basin. *Journal of Geophysical Research*, 100:10851–10, 1995.

E. Kunze. Near-inertial wave propagation in geostrophic shear. *Journal of Physical Oceanography*, 15:544–565, 1985.

E. Kunze, R.W. Schmitt, and J.M. Toole. The energy balance in a warm-core ring's near-inertial critical layer. *Journal of Physical Oceanography*, 25:942–957, 1995.

J.H. LaCasce and J. Pedlosky. The instability of rossby basin modes and the oceanic eddy field*. *Journal of Physical Oceanography*, 34:2027–2041, 2004.

K.L. Lavender, R.E. Davis, and W.B. Owens. Mid-depth recirculation observed in the interior Labrador and Irminger Seas by direct velocity measurements. *Nature*, 407: 66–69, 2000.

K.L. Lavender, W. Brechner Owens, and R.E. Davis. The mid-depth circulation of the subpolar North Atlantic Ocean as measured by subsurface floats. *Deep Sea Research Part I: Oceanographic Research Papers*, 52:767–785, 2005.

S. Levitus and T.P. Boyer. World ocean atlas 1994. volume 4. temperature. Technical report, National Environmental Satellite, Data, and Information Service, Washington, DC (United States), 1994.

P. Lherminier, H. Mercier, C. Gourcuff, M. Alvarez, S. Bacon, and C. Kermabon. Transports across the 2002 Greenland-Portugal Ovide section and comparison with 1997- art. no. C07003. *Journal of Geophysical Research (JGR)-Oceans*, 112, 2007.

P. Lherminier, H. Mercier, T. Huck, C. Gourcuff, F.F. Perez, P. Morin, A. Sarafanov, and A. Falina. The Atlantic Meridional Overturning Circulation and the subpolar gyre observed at the A25-OVIDE section in June 2002 and 2004. *Deep Sea Research Part I: Oceanographic Research Papers*, 57:1374–1391, 2010.

J.M. Lilly and P.B. Rhines. Coherent eddies in the Labrador Sea observed from a moorring. *Journal of Physical Oceanography*, 32:585–598, 2002.

J.M. Lilly, P.B. Rhines, F. Schott, K. Lavender, J. Lazier, U. Send, and E. D'Asaro. Observations of the Labrador Sea eddy field. *Progress in Oceanography*, 59:75–176, 2003.

E. Louarn, H. Mercier, P. Morin, E. De Boisseson, and S. Bacon. Upper Labrador Sea Water in the Irminger Sea during a weak convection period (2002-2006). *Ocean Science Discussions*, 6:2085–2113, 2009.

G. Madec. Nemo ocean engine. *Institut Pierre-Simon Laplace (IPSL)*, 2008.

J. Marshall and F. Schott. Open-ocean convection: Observations, theory, and models. *Reviews of Geophysics*, 37:1–64, 1999.

J.P. Martin, C.M. Lee, C.C. Eriksen, C. Ladd, and N.B. Kachel. Glider observations of kinematics in a Gulf of Alaska eddy. *Journal of Geophysical Research*, 114:C12021, 2009.

N. Maximenko, P. Niiler, L. Centurioni, M.H. Rio, O. Melnichenko, D. Chambers, V. Zlotnicki, and B. Galperin. Mean Dynamic Topography of the Ocean Derived from Satellite and Drifting Buoy Data Using Three Different Techniques. *Journal of Atmospheric and Oceanic Technology*, 26:1910–1919, 2009.

D.J. McGillicuddy, L.A. Anderson, N.R. Bates, T. Bibby, K.O. Buesseler, C.A. Carlson, C.S. Davis, C. Ewart, P.G. Falkowski, S.A. Goldthwait, et al. Eddy/wind interactions stimulate extraordinary mid-ocean plankton blooms. *Science*, 316:1021, 2007.

J.C. McWilliams. Submesoscale, coherent vortices in the ocean. *Reviews of Geophysics*, 23:165–182, 1985.

J.R. Moisan and P.P. Niiler. The seasonal heat budget of the north pacific: Net heat flux and heat storage rates (1950-1990). *Journal of Physical Oceanography*, 28:401–421, 1998.

J.A. Nelder and R. Mead. A simplex method for function minimization. *The Computer Journal*, 7:308, 1965.

F. Nencioli, C. Dong, T. Dickey, L. Washburn, and J.C. McWilliams. A vector geometry-based eddy detection algorithm and its application to a high-resolution numerical model product and high-frequency radar surface velocities in the southern california bight. *Journal of Atmospheric and Oceanic Technology*, 27:564–579, 2010.

J.L. Newton, K. Aagaard, and L.K. Coachman. Baroclinic eddies in the Arctic Ocean. In *Deep Sea Research and Oceanographic Abstracts*, volume 21, pages 707–719, 1974.

J. Nilsen and E. Falck. Variations of mixed layer properties in the Norwegian sea for the period 1948-1999. *Progress in Oceanography*, 70:58–90, 2006.

L.W. ONeill, D.B. Chelton, and S.K. Esbensen. Observations of sst-induced perturbations of the wind stress field over the southern ocean on seasonal timescales. *Journal of Climate*, 16:2340–2354, 2003.

L. Padman, M. Levine, T. Dillon, J. Morison, and R. Pinkel. Hydrography and microstructure of an arctic cyclonic eddy. *Journal of Geophysical Research*, 95:9411–9420, 1990.

A. Persson and F. Grazzini. User guide to ecmwf forecast products. *Meteorological Bulletin*, 3:2, 2005.

R.S. Pickart, M.A. Spall, M.H. Ribergaard, G.W.K. Moore, and R.F. Milliff. Deep convection in the Irminger Sea forced by the Greenland tip jet. *Nature*, 424:152–156, 2003.

N. Picot, K. Case, S. Desai, and P. Vincent. AVISO and PODAAC User Handbook. *IGDR and GDR Jason Products*, 2003.

R.D. Pingree and B. Le Cann. Anticyclonic eddy X91 in the southern Bay of Biscay, May 1991 to February 1992. *Journal of Geophysical Research*, 97:14353–14, 1992.

J. Piquet. *Turbulent flows: models and physics*. Springer, 1999.

P.S. Polito, J.P. Ryan, W.T. Liu, and F.P. Chavez. Oceanic and atmospheric anomalies of tropical instability waves. *Geophysical Research Letters*, 28:2233–2236, 2001.

P.M. Poulain, A. Warn-Varnas, and PP Niiler. Near-surface circulation of the Nordic seas as measured by Lagrangian drifters. *Journal of Geophysical Research*, 101: 18237–18, 1996.

M.D. Prater. Eddies in the Labrador Sea as observed by profiling RAFOS floats and remote sensing. *Journal of Physical Oceanography*, 32:411–427, 2002.

I.A. Renfrew, G.W.K. Moore, P.S. Guest, and K. Bumke. A comparison of surface layer and surface turbulent flux observations over the labrador sea with ecmwf analyses and ncep reanalyses. *Journal of Physical Oceanography*, 32:383–400, 2002.

W.C. Reynolds and A.K.M.F. Hussain. The mechanics of an organized wave in turbulent shear flow. part 3. theoretical models and comparisons with experiments. *Journal of Fluid Mechanics*, 54:263–288, 1972.

P.L. Richardson, D. Walsh, L. Armi, M. Schröder, and J.F. Price. Tracking three meddies with SOFAR floats. *Journal of Physical Oceanography*, 19:371–383, 1989.

M.J. Rodwell, D.P. Rowell, and C.K. Folland. Oceanic forcing of the wintertime north atlantic oscillation and european climate. *Nature*, 398:320–323, 1999.

D. Roemmich and J. Gilson. The 2004–2008 mean and annual cycle of temperature, salinity, and steric height in the global ocean from the argo program. *Progress in Oceanography*, 82:81–100, 2009.

T. Rossby, V. Ozhigin, V. Ivshin, and S. Bacon. An isopycnal view of the Nordic Seas hydrography with focus on properties of the Lofoten Basin. *Deep Sea Research Part I: Oceanographic Research Papers*, 56:1955–1971, 2009a.

T. Rossby, MD Prater, and H. Søiland. Pathways of inflow and dispersion of warm waters in the Nordic seas. *Journal of Geophysical Research*, 114:C04011, 2009b.

D.L. Rudnick, R.E. Davis, C.C. Eriksen, D.M. Fratantoni, and M.J. Perry. Underwater gliders for ocean research. *Marine Technology Society Journal*, 38:73–84, 2004.

T. Rykova, F. Straneo, J.M. Lilly, and I. Yashayaev. Irminger Current Anticyclones in the Labrador Sea observed in the hydrographic record, 1990-2004. *Journal of Marine Research*, 67:361–384, 2009.

O.A. Saenko, F. Dupont, D. Yang, P.G. Myers, I. Yashayaev, and G.C. Smith. Role of resolved and parameterized eddies in the labrador sea balance of heat and buoyancy. *Journal of Physical Oceanography*, 44:3008–3032, 2014.

A. Sarafanov, A. Sokov, A. Demidov, and A. Falina. Warming and salinification of intermediate and deep waters in the Irminger Sea and Iceland Basin in 1997–2006. *Geophysical Research Letters*, 34:L23609, 2007.

S. Schmidt and U. Send. Origin and composition of seasonal Labrador Sea freshwater. *Journal of Physical Oceanography*, 37:1445–1454, 2007.

M.W. Schonten, W.P.M. Ruijter, P.J. Leeuwen, and J.R. Lutjeharms. Translation, decay and splitting of agulhas rings in the southeastern atlantic ocean. *Journal of Geophysical Research*, 105:21913–21925, 2000.

F.A. Schott, R. Zantopp, L. Stramma, M. Dengler, J. Fischer, and M. Wibaux. Circulation and deep-water export at the western exit of the subpolar North Atlantic. *Journal of Physical Oceanography*, 34:817–843, 2004.

U. Send and J. Marshall. Integral effects of deep convection. *Journal of Physical Oceanography*, 25:855–872, 1995.

J. Sherman, R.E. Davis, W.B. Owens, and J. Valdes. The autonomous underwater glider Spray. *IEEE Journal of Oceanic Engineering*, 26:437–446, 2001.

S.D. Smith. Coefficients for sea surface wind stress, heat flux, and wind profiles as a function of wind speed and temperature. *Journal of Geophysical Research: Oceans (1978–2012)*, 93:15467–15472, 1988.

S.R. Smith, D.M. Legler, and K.V. Verzone. Quantifying uncertainties in ncep reanalyses using high-quality research vessel observations. *Journal of Climate*, 14:4062–4072, 2001.

D. Stammer and C.W. Böning. Mesoscale variability in the Atlantic Ocean from Geosat altimetry and WOCE high-resolution numerical modeling. *Journal of Physical Oceanography*, 22:732–752, 1992.

J.W. Stevenson and P.P. Niiler. Upper ocean heat budget during the hawaii-to-tahiti shuttle experiment. *Journal of Physical Oceanography*, 13:1894–1907, 1983.

D.A. Sutherland and R.S. Pickart. The east greenland coastal current: Structure, variability, and forcing. *Progress in Oceanography*, 78:58–77, 2008.

L.D. Talley. Potential vorticity distribution in the North Pacific. *Journal of Physical Oceanography*, 18:89–106, 1988.

E.D. Traganza, V.M. Silva, D.M. Austin, W.L. Hanson, and S.H. Bronsink. Nutrient mapping and recurrence of coastal upwelling centers by satellite remote sensing: Its implication to primary production and the sediment record. In *Coastal Upwelling Its Sediment Record*, pages 61–83. Springer, 1983.

K. Våge, R.S. Pickart, A. Sarafanov, Ø. Knutsen, H. Mercier, P. Lherminier, M. Bersch, H. van Aken, J. Meincke, and D. Quadfasel. Surprising return of deep convection to the subpolar North Atlantic Ocean in winter 2007–2008. *Nature Geoscience*, 2: 67–72, 2008a.

K. Våge, R.S. Pickart, V. Thierry, G. Reverdin, C.M. Lee, B. Petrie, T.A. Agnew, A. Wong, and M.H. Ribergaard. Surprising return of deep convection to the subpolar north atlantic ocean in winter 2007–2008. *Nature Geoscience*, 2:67–72, 2008b.

K. Våge, R.S. Pickart, A. Sarafanov, Ø. Knutsen, H. Mercier, P. Lherminier, M. Bersch, H. van Aken, J. Meincke, and D. Quadfasel. The Irminger Gyre: Circulation, convection, and interannual variability. *Deep Sea Research Part I: Oceanographic Research Papers*, 58:590 – 614, 2011a.

K. Våge, R.S. Pickart, A. Sarafanov, Ø. Knutsen, H. Mercier, P. Lherminier, M. Bersch, H. van Aken, J. Meincke, and D. Quadfasel. The irminger gyre: Circulation, convection, and interannual variability. *Deep-Sea Research*, 1:590–614, 2011b.

G.K. Vallis. *Atmospheric and oceanic fluid dynamics: fundamentals and large-scale circulation*. Cambridge University Press, 2006.

C.L. Wolfe and C. Cenedese. Laboratory experiments on eddy generation by a buoyant coastal current flowing over variable bathymetry. *Journal of Physical Oceanography*, 36:395–411, 2006.

D.G. Wright, R. Pawlowicz, T.J. McDougall, R. Feistel, and G.M. Marion. Absolute salinity," density salinity" and the reference-composition salinity scale: present and future use in the seawater standard teos-10. *Ocean Science*, 7, 2011.

I. Yashayaev, H.M. van Aken, N.P. Holliday, and M. Bersch. Transformation of the labrador sea water in the subpolar north atlantic. *Geophysical Research Letters*, 34: L22605, 2007.